

POLITECNICO DI TORINO

Master's Degree in Aerospace Engineering



**Politecnico
di Torino**



Master's Degree Thesis

**Numerical investigations on
boundary conditions with
turbulence injection and their
impact on a high-speed low
pressure turbine cascade**

Supervisor:

Prof. Andrea FERRERO

Co-Supervisor:

Prof. Koen HILLEWAERT

Candidate

Carlo DI CINTIO

April 2025

Abstract

This master's thesis investigates the impact of the inlet boundary conditions on the spatial evolution of the turbulence injected using a library-based method. The free-stream turbulence inflow data has been generated with a precursor approach through the Direct Numerical Simulation (DNS) of a Decaying Homogeneous Isotropic Turbulence (DHIT). Numerical studies have been carried out using the solver ArgoDG, developed at Cenaero, which is based on a high-order discontinuous Galerkin method.

Firstly, a parametric study was conducted in a free domain to assess the influence of various simulation parameters (i.e. Reynolds number, Mach number, injection angle, type of boundary conditions and mesh) on the properties of a freely decaying turbulence. The results show that imposing total conditions at the inlet leads the injected turbulence to become anisotropic. Moreover, a non-zero injection angle amplifies the discrepancy between the turbulent kinetic energy associated with the three spatial directions. On the other hand, static inlet conditions result in isotropic injected turbulence, even though the mesh is anisotropic and the injection angle is not zero.

Subsequently, static boundary conditions at the inlet were applied to simulate a high-speed low-pressure turbine cascade with high free-stream turbulence. The results were compared with a simulation of the same case but using total inlet conditions. A detailed evaluation of the impact on the flow physics will be presented, including blade loading, boundary layer stability and wake behavior. Overall, the turbulence upstream of the blade exhibits characteristics consistent with those observed in the free domain. Furthermore, the simulation with static inlet conditions shows better agreement with experimental data.

Acknowledgements

First and foremost, I would like to express my deepest gratitude to Professor Koen Hillewaert, my academic supervisor during my research project at the University of Liège. His guidance and support have been fundamental to this work. Furthermore, I would like to thank him for sharing his experience and passion for the subject, which have helped me grow personally.

I am deeply grateful to my supervisor at Politecnico di Torino, Professor Andrea Ferrero, for his assistance throughout my academic journey. I am particularly grateful for his CFD lectures, which sparked my interest in this field.

Special thanks are due to Dr. Margaux Boxho, Research Engineer at Cenaero, for her unwavering and kind willingness to help me. Her advice and suggestions played a crucial role in the research process and in the writing of this master's thesis. I would also like to thank Cenaero for providing the computational resources without which this study would not have been possible. Computational resources have been provided by the Consortium des Équipements de Calcul Intensif (CÉCI), funded by the Fonds de la Recherche Scientifique de Belgique (F.R.S.-FNRS) under Grant No. 2.5020.11 and by the Walloon Region. The present research benefited from computational resources made available on Lucia, the Tier-1 supercomputer of the Walloon Region, infrastructure funded by the Walloon Region under the grant agreement n°1910247.

To Maxime Borbouse and Nathan Deneffe, PhD candidates at the University of Liège, for welcoming me and making me feel at home during my stay at the institute, as well as for their invaluable help and guidance. I also extend my gratitude to the von Karman Institute for Fluid Dynamics for providing the experimental results, a precious contribution to this work.

Finally, I warmly thank my friends and family for being present throughout my journey. In particular, to my parents, for their unwavering support in every moment over these years, especially the difficult ones. A special thank you to my girlfriend, for believing in me and encouraging me every day.

Contents

1	Introduction	1
2	Flow physics	4
2.1	Physical model	4
2.2	Turbulence	5
2.2.1	Statistical description	6
2.2.2	Scales of turbulence	10
2.2.3	Other parameters of turbulence and Taylor’s hypothesis	11
2.3	Boundary layer	13
2.3.1	Laminar-turbulent transition	14
2.3.2	Separation	17
2.3.3	Universal law of the wall	18
2.4	Wake	19
3	Low pressure turbine features	22
3.1	Geometrical parameters	22
3.2	Operating conditions parameters	24
3.3	Performance parameters	24
3.4	Sources of losses	25
3.5	Separation and transition	27
4	SPLEEN cascade experimental background	31
4.1	Experimental environment	31
4.2	Free-stream turbulence generation	33
5	Numerical methods and tools	35
5.1	HPC	36
5.1.1	NIC5	36
5.1.2	Lucia	37
5.2	DGM	37
5.3	ArgoDG	39
6	Turbulence injection	40
6.1	Review of existing turbulence injection methods	40
6.1.1	Transition-inducting methods	40
6.1.2	Turbulence library-based methods	41
6.1.3	Recycling-rescaling methods	41
6.1.4	Synthetic inflow generators	42
6.1.5	Machine learning and deep learning techniques	42

6.2	Turbulence injection procedure	42
6.2.1	Setup and execution of the precursor simulation	43
6.2.2	Duplication, transformation, concatenation and blending of the precursor solution field	44
7	Free domain simulations	45
7.1	Computational setup	45
7.1.1	Computational domain and meshing	46
7.1.2	Solver settings	48
7.1.3	Boundary and initial conditions	48
7.1.4	Convergence	50
7.1.5	Data extraction	52
7.2	Results and discussion	53
7.2.1	Baseline case	53
7.2.2	Reynolds and mach numbers effect	55
7.2.3	Boundary condition type effect	60
7.2.4	Injection angle effect	64
7.2.5	Mesh isotropy effect	70
7.2.6	Mesh isotropy effect with non-zero injection angle	75
8	Turbine simulations	77
8.1	Computational setup	77
8.1.1	Computational domain and meshing	77
8.1.2	Boundary conditions, initial conditions and convergence	80
8.1.3	Data extraction	82
8.2	Results and discussion	83
8.2.1	Inlet	83
8.2.2	Fields	85
8.2.3	Blade loading	88
8.2.4	Skin friction	89
8.2.5	Boundary layer	92
8.2.6	Wake	95
9	Conclusion	102

List of Figures

2.1	Typical energy spectrum for homogeneous isotropic turbulence	12
2.2	Boundary layer developing on a flat plate at zero incidence	13
2.3	Sketch of transition in the boundary layer on a flat plate at zero incidence (reproduced from [17])	15
2.4	Time averaged velocity profiles for laminar and turbulent remise	16
2.5	Boundary layer separation on a curved surface	17
2.6	Velocity distribution in the wall layer	19
2.7	Sketch of a typical von Karman vortex street for a circular cylinder in a flow with $80 < Re < 200$ (reproduced from [18])	20
3.1	Schematic of the geometrical parameters for LPT cascade with SPLEEN blades	23
3.2	Different modes of boundary layer transition related to Tu , K and Re_θ (reproduced from [21])	27
3.3	Time-averaged representation of different flow-separated transitional modes (reproduced from [23]): <i>transitional separation mode</i> (top), <i>laminar separation/short bubble mode</i> (center) and <i>laminar separation/long bubble mode</i> (bottom)	29
3.4	Qualitative effect of Re on the performance of a LPT cascade (reproduced from [24])	30
4.1	VKI S1/C wind tunnel (taken from [27])	31
4.2	VKI S1/C wind tunnel (taken from [27])	32
5.1	A visual comparison of the fundamental properties of different CFD methods	36
5.2	Example of the discontinuous trial space of the DGM (taken from [36])	38
6.1	Precursor domain mesh, 3-dimensional view	43
7.1	Free domain, 3-dimensional view	47
7.2	Free domain isotropic mesh, 3-dimensional view	47
7.3	Isotropic mesh (left) and anisotropic mesh (right), 2-dimensional inlet view	48
7.4	Free domain with inlet shown in green (left) and outlet shown in red (right), 2-dimensional view	49
7.5	Convective density flux (Φ_ρ [$\text{kg m}^{-2} \text{s}^{-1}$]) during the numerical transient of the simulation	51
7.6	Convective density flux (Φ_ρ [$\text{kg m}^{-2} \text{s}^{-1}$]) of the converged simulation	51
7.7	Free domain probe set shown in red , 2-dimensional side-view	52

7.8	High density probe set shown in red (on the left) and low density probe set shown in green (on the right), 2-dimensional inlet view . . .	52
7.9	Streamwise evolution of diagonal terms of the Reynolds stress tensor for the base case	53
7.10	Streamwise evolution of the Turbulent Kinetic Energy (left) and Turbulent Intensity (right) for the base case	54
7.11	Streamwise evolution of velocity integral length scale for the base case	54
7.12	Streamwise evolution of diagonal terms of Reynolds stress tensor for different Re and M cases	55
7.13	Streamwise evolution of $\overline{u'u'}$ (top-left), $\overline{v'v'}$ (top-right), and $\overline{w'w'}$ (bottom) for different Re and M cases	56
7.14	Streamwise evolution of the Turbulent Kinetic Energy for different Re and M cases	57
7.15	Streamwise evolution of velocity integral length scale for different Re and M cases	58
7.16	Streamwise evolution of L_{XX} (top-left), L_{YY} (top-right), and L_{ZZ} (bottom) for different Re and M cases	59
7.17	Streamwise evolution of diagonal terms of Reynolds stress tensor for different inlet boundary conditions type	60
7.18	Streamwise evolution of $\overline{u'u'}$ (top-left), $\overline{v'v'}$ (top-right), and $\overline{w'w'}$ (bottom) for different inlet boundary conditions type	61
7.19	Streamwise evolution of the Turbulent Kinetic Energy for different inlet boundary conditions type	62
7.20	Streamwise evolution of velocity integral length scale for different inlet boundary conditions type	62
7.21	Streamwise evolution of L_{XX} (top-left), L_{YY} (top-right), and L_{ZZ} (bottom) for different inlet boundary conditions type	63
7.22	Streamwise evolution of diagonal terms of Reynolds stress tensor for different α_{in} , using Mach total boundary conditions	64
7.23	Streamwise evolution of $\overline{u'u'}$ (top-left), $\overline{v'v'}$ (top-right), and $\overline{w'w'}$ (bottom) for different α_{in} , using Mach total boundary conditions . .	65
7.24	Streamwise evolution of the Turbulent Kinetic Energy for different α_{in} , using Mach total boundary conditions	66
7.25	Streamwise evolution of velocity integral length scale for different α_{in} , using Mach total boundary conditions	66
7.26	Streamwise evolution of L_{XX} (top-left), L_{YY} (top-right), and L_{ZZ} (bottom) for different α_{in} , using Mach total boundary conditions . .	67
7.27	Streamwise evolution of diagonal terms of Reynolds stress tensor for different α_{in} , using Free stream boundary conditions	68
7.28	Streamwise evolution of velocity integral length scale for different α_{in} , using Free stream boundary conditions	68
7.29	Streamwise evolution of L_{XX} for different α_{in} , using Free stream boundary conditions	69
7.30	Streamwise evolution of $\overline{u'u'}$ for different meshes, using Mach total boundary conditions	70
7.31	Streamwise evolution of L_{XX} for different meshes, using Mach total boundary conditions	71

7.32	Streamwise evolution of $\overline{u'u'}$ (top-left), $\overline{v'v'}$ (top-right), and $\overline{w'w'}$ (bottom) for different meshes, using Free stream boundary conditions	72
7.33	Streamwise evolution of diagonal terms of Reynolds stress tensor for different meshes, using Free stream boundary conditions	72
7.34	Streamwise evolution of the Turbulent Kinetic Energy for different meshes, using Free stream boundary conditions	73
7.35	Streamwise evolution of L_{XX} (top-left), L_{YY} (top-right), and L_{ZZ} (bottom) for different different meshes, using Free stream boundary conditions	73
7.36	Streamwise evolution of velocity integral length scale for different meshes, using Free stream boundary conditions	74
7.37	Streamwise evolution of $\overline{u'u'}$ for different meshes, using Mach total boundary conditions and with $\alpha_{in} \neq 0^\circ$	75
7.38	Streamwise evolution of the Turbulent Kinetic Energy for different meshes, using Mach total boundary conditions and with $\alpha_{in} \neq 0^\circ$. . .	76
7.39	Streamwise evolution of L_{XX} for different different meshes, using Mach total boundary conditions and with $\alpha_{in} \neq 0^\circ$	76
8.1	Turbine domain with inlet shown in green (left) and outlet shown in red (right), 2-dimensional view	78
8.2	Mesh of the turbine domain, 2-dimensional view (taken from [7]) . . .	79
8.3	Time-averaged and extremes instantaneous values of the wall coordinates associated to the near-wall elements	80
8.4	Time evolution of the pitchwise component of the momentum fluxes; data are monitored during the numerical transient and extracted on the inlet, the outlet and the blade, for both total (top) and static (bottom) inlet boundary conditions [total case taken from 7]	81
8.5	Probes layout in the turbine domain	82
8.6	Streamwise evolution of the Reynolds stresses in the inlet region, averaged over time and along pitchwise and spanwise directions, with total (left) and static (right) inlet boundary conditions (total case reproduced from [7])	84
8.7	Streamwise evolution of the TKE in the inlet region, averaged over time and along pitchwise and spanwise directions, with total and static inlet boundary conditions; the curves are compared to the TKE evolution predicted using the DHIT (total case reproduced from [7]) .	84
8.8	Streamwise evolution of the integral length scales in the inlet region related to the three components of velocity fluctuation, averaged over time and integrated along the spanwise direction, with total (left) and static (right) inlet boundary conditions (total case reproduced from [7])	85
8.9	Energy density spectrum averaged over time and along pitchwise and spanwise directions, extracted at $0.5 \times c_{ax}$ upstream to the LE of the blade, for total and static inlet boundary conditions (total case reproduced from [7])	85
8.10	Instantaneous field of the Mach number extracted from the spanwise plane at $z = 0$, with total (left) and static (right) inlet boundary conditions (total case taken from [7])	86

8.11	Instantaneous field of the vorticity magnitude extracted from the spanwise plane at $z = 0$, with total (left) and static (right) inlet boundary conditions (total case taken from [7])	87
8.12	Instantaneous field of the normalized density gradient (numerical Schlieren) extracted from the spanwise plane at $z = 0$, with total (left) and static (right) inlet boundary conditions (total case taken from [7])	88
8.13	Instantaneous field of the entropy generation extracted from the spanwise plane at $z = 0$, with total (left) and static (right) inlet boundary conditions (total case taken from [7])	88
8.14	Time and spanwise average of the isentropic Mach number on the blade, with total and static inlet boundary conditions cases (total case taken from [7]) compared to experimental data [1]	89
8.15	Time and spanwise average of the skin friction coefficient on the blade, with total and static inlet boundary conditions cases [total case taken from 7] compared to experimental data [1]	90
8.16	Time evolution of the spanwise averaged skin friction coefficient on the blade, with total (top) and static (bottom) inlet boundary conditions (total case taken from [7])	91
8.17	Time and spanwise average of tangential velocity profiles in the boundary layer, with total and static inlet boundary conditions (total case taken from [7])	92
8.18	Time and spanwise average of the tangential velocity in the boundary layer, with total (top) and static (bottom) inlet boundary conditions (total case taken from [7])	93
8.19	Time and spanwise average of the TKE distribution in the boundary layer, with total (top) and static (bottom) inlet boundary conditions (total case taken from [7])	94
8.20	Time and spanwise average of the boundary layer integral parameters, with total (left) and static (right) inlet boundary conditions (total case taken from [7])	95
8.21	Time and spanwise average of displacement thickness (top-left), momentum thickness (top-right) and shape factor (bottom), with total and static inlet boundary conditions (total case taken from [7])	96
8.22	Time and spanwise average of the total pressure defect in the wake on planes 05 and 06, with total and static inlet boundary conditions cases (total case taken from [7]) compared to experimental data [1] (plane 06 only)	97
8.23	Time and spanwise average of the total temperature in the wake on planes 05 and 06, with total and static inlet boundary conditions (total case taken from [7])	97
8.24	Time and spanwise average of the flow angle in the wake on planes 05 and 06, with total and static inlet boundary conditions (total case taken from [7])	98
8.25	Time and spanwise average of the diagonal stresses in the wake on planes 05 and 06, with total and static inlet boundary conditions (total case taken from [7])	99

8.26	Time and spanwise average of the energy density spectrum in the wake on planes 05 and 06, with total and static inlet boundary conditions (total case taken from [7])	100
8.27	Time and spanwise average of the integral length scales in the wake on planes 05 and 06, with total and static inlet boundary conditions (total case taken from [7])	101

List of Tables

3.1	Geometrical parameter of the SPLEEN blade	23
3.2	Operating conditions for the SPLEEN simulation	24
4.1	Turbulence parameters predicted with semi-empirical law and measured experimentally with hot-wire probes	34
7.1	Characteristics of the baseline case	45
7.2	Re and M values for the parametric study	46
7.3	Summary of the parametric study	46
7.4	Boundary conditions for simulations with different Re and M	49
7.5	Boundary conditions for simulations with different α	49
7.6	Example case with Free stream boundary conditions	50
7.7	Types of initial solution	50
7.8	Injection angles and related injection vectors	64
8.1	Inlet boundary conditions parameters for the turbine simulation	80

Chapter 1

Introduction

Over the past few decades, the utilization of Computational Fluid Dynamics (CFD) has become an increasingly prevalent tool across various engineering disciplines. In industrial settings, Reynolds Averaged Navier Stokes (RANS) simulations are extensively employed. However, in scenarios involving complex geometries and flows characterized by laminar to turbulent transition and separation, such as those encountered in turbomachinery, RANS methods tend to exhibit low reliability. To achieve higher accuracy, Large Eddy Simulation (LES) and Direct Numerical Simulation (DNS) are adopted. Despite their increased computational cost, these methodologies enable the capture and analysis of complex flow features.

Arguably, turbulence represents the most intricate flow characteristic to accurately model. This phenomenon is virtually ubiquitous in fluid dynamics and can exert a substantial influence on flow properties. Consequently, the faithful representation of turbulence is of paramount importance in the majority of fluid dynamic applications relevant to engineering, including turbomachinery. Unlike other methods where the effect of turbulence is partially or entirely modeled, DNS resolves all turbulent scales, thereby yielding a higher fidelity of the results.

The challenge of accurately representing turbulence is particularly pronounced when dealing with spatially evolving turbulent inflow boundary conditions. In such cases, it becomes imperative to generate turbulent inflow data, thereby simulating the introduction of turbulent eddies into the computational domain as a function of time. This procedure is commonly referred to as turbulence injection, and a multitude of methodologies exist in the literature for generating such inflow conditions.

The primary objective of this master's thesis is to investigate how various numerical simulation characteristics can impact the injection and evolution of turbulence within the main computational domain, while maintaining a constant turbulent inflow dataset. To this end, DNS were performed on meshes generated using the GMSH software. The numerical solver employed is ArgoDG, which implements a high-order Discontinuous Galerkin Method (DGM). The turbulent inflow data were generated through a Decaying Homogeneous Isotropic Turbulence (DHIT) simulation in an auxiliary domain, following the precursor method.

This study can be ideally divided into two primary parts. The first part evaluates the effect of various simulation parameters on the injected turbulence. The parameters selected for the parametric study are: Reynolds number, Mach number, boundary condition type, injection angle, and mesh. The study is conducted through

a series of DNS in a simplified free domain. This domain, characterized by its simple geometry and absence of solid walls, was chosen to minimize the computational cost of each simulation and to assess the impact on freely decaying turbulence.

In the second part of this study, the effect of different inlet boundary conditions is analyzed in a numerical simulation with turbulence injection relevant to practical applications. The case under consideration is a high-speed low-pressure turbine (LPT) pertaining to the new generation of geared turbofan (GTF) engines. The fundamental concept behind these engines is to decouple the rotational speed of the low-pressure turbine from the fan through a gearbox, thereby enabling optimal rotational speeds and consequently enhancing the efficiency of the turbomachine. Indeed, in conventional turbofans, the low-pressure spool speed is limited by compressibility effects on the fan, leading to suboptimal operation of the low-pressure turbine. The combination of high speed in LPT of GTF and low density in cruise conditions induces different physical effect compared to conventional turbofans. A large range of experimental results in on-design and off-design conditions has been obtained in the SPLEEN project, which is led by the von Karman Institute for Fluid Dynamics (VKI) [1]. Indeed, the LPT analyzed in this master's thesis is a linear cascaded composed by SPLEEN blades, that are specially designed for low Reynolds and high Mach conditions. Moreover, numerical studies of the SPLEEN cascade have been conducted in previous works, by Bolyne [2], Khateeb [3], Borbouse et al. [4, 5, 6], and Deneffe [7]. Specifically, the study of [7] employed turbulence injection to analyze the turbine under three operating conditions, characterized by Reynolds numbers of $70 \cdot 10^3$ and Mach numbers of 0.7, 0.90, and 0.95, respectively. The turbine simulation performed in this study corresponds to the operating condition with a Reynolds number of $70 \cdot 10^3$ and a Mach number of 0.70, utilizing the same simulation parameters and turbulent inflow data as in [7], with the exception of the inlet boundary condition type. While [7] used total inlet conditions, this study employs static inlet conditions. This master's thesis presents a comparison between the two numerical simulations, as well as with experimental results, to assess the effect of free stream turbulence on the turbine simulation under different inlet boundary conditions.

The structure of this master's thesis is organized into the following chapters:

- Chapter 2 covers the main physical concepts related to the flow equations and turbulence, including phenomena that occur with relative motion between a fluid and a body, such as boundary layers and wakes;
- Chapter 3 summarizes some useful concepts for dealing with low pressure turbine, which include geometry, operating conditions, performances, sources of losses and blade channel phenomena;
- Chapter 4 briefly shows the VKI experimental setup used to obtain the SPLEEN results;
- Chapter 5 introduces the computational resources used to run the simulations, as well as the solver and numerical method employed;
- Chapter 6 presents the main turbulence injection method and details the precursor approach used to generate the turbulent inflow data employed in this study;

- Chapter 7 discusses the computational settings and the results related to the parametric study and free domain;
- Chapter 8 focuses on the turbine computations, highlighting the effect of the two different inlet boundary conditions types (static and total) while injecting turbulence.

Chapter 2

Flow physics

This chapter provides the theoretical and conceptual foundation necessary to understand the results presented in the following chapters. Firstly, the physical model implemented for the numerical simulations is introduced, including the governing fluid flow equations and associated assumptions. Secondly, the concept of turbulence is discussed, including common statistical tools used for its description and key theoretical advancements in understanding the phenomenon. Given that all simulations in this study involve turbulence injection (as detailed in Chapter 6), the underlying physics of this process is also explored. The boundary layer concept is then introduced, highlighting its ubiquitous nature in flows over solid surfaces. The key parameters used to characterize boundary layers are discussed, along with phenomena such as transition and separation. Lastly, the concept of wakes is presented, with a particular focus on the von Karman vortex street and the influence of boundary layer state on wake characteristics.

2.1 Physical model

This section will briefly discuss the physical model implemented in the numerical solver (ArgoDG). The equations that describe the motion of viscous fluids are known as Navier-Stokes equations (NSE). The NSE are a set of partial differential equations, which include continuity equation, momentum equations and energy equation. NSE can be written in many different forms. The following NSE are given as examples in Cartesian coordinates, using Einstein notation:

$$\begin{cases} \frac{\partial \rho}{\partial t} + \frac{\partial(\rho u_i)}{\partial x_i} = 0 \\ \frac{\partial(\rho u_i)}{\partial t} + \frac{\partial(\rho u_i u_j)}{\partial x_j} = -\frac{\partial p}{\partial x_i} + \frac{\partial \tau_{ij}}{\partial x_j} + \rho f_i \\ \frac{\partial(\rho E)}{\partial t} + \frac{\partial[(\rho E + p)u_i]}{\partial x_j} = \frac{\partial(k\partial T/\partial x_i)}{\partial x_j} + \tau_{ij} \frac{\partial u_i}{\partial x_j} + \rho f_i u_i. \end{cases} \quad (2.1)$$

The terms that appear in Equation 2.1 are:

- t : time, [s];
- x_i : i -th spatial coordinate, [m];
- ρ : density, [kg/m³];

- u_i : i -th velocity component, [m/s];
- p : pressure, [Pa];
- τ_{ij} : viscous stress tensor, [Pa];
- f_i : i -th direction of the body force per unit mass, [N/kg];
- E : total energy per unit mass, [J/kg];
- k : thermal conductivity, [W/(m·K)];
- T : Temperature, [K].

Since all the simulations in this study are DNS, the NSE are solved without any model for the turbulence (see Chapter 5). However, some assumptions are made, for example the body force are neglected ($f_i = 0$), as well as the heat exchanges with solid bodies (adiabatic walls). Furthermore, ideal and calorically perfect gas assumptions are made. The fluid considered has a ratio of the specific heat capacities $\gamma = 1.4$, a gas constant $R = 287.1 \text{ J}\cdot\text{kg}^{-1}\cdot\text{K}^{-1}$ and a thermal conductivity $k = 0.02414 \text{ W}\cdot\text{m}^{-1}\cdot\text{K}^{-1}$. Moreover, the viscous stress tensor is calculated using the assumption of Newtonian fluid:

$$\tau_{ij} = \mu \left(\frac{\partial u_i}{\partial u_j} + \frac{\partial u_j}{\partial u_i} - \frac{2}{3} \delta_{ij} \frac{\partial u_k}{\partial u_k} \right), \quad (2.2)$$

where μ is the dynamic viscosity [$\text{N}\cdot\text{s}/\text{m}^2$] and δ_{ij} is the Kronecker delta. The latter is defined by

$$\delta_{ij} = \begin{cases} 1, & \text{if } i = j \\ 0, & \text{if } i \neq j. \end{cases} \quad (2.3)$$

Lastly the empirical Shuterland's law [8] has been used to model the temperature dependence of the dynamic viscosity:

$$\frac{\mu}{\mu_0} = \left(\frac{T}{T_0} \right)^{\frac{3}{2}} \frac{T_0 + S}{T + S}, \quad (2.4)$$

where μ_0 is the dynamic viscosity at a reference temperature T_0 and S is the Sutherland's constant. The values for the fluid considered in this study are $\mu_0 = 1.5 \cdot 10^{-5} \text{ N}\cdot\text{s}/\text{m}^2$, $T_0 = 293.15 \text{ K}$ and $S = 110.4 \text{ K}$.

2.2 Turbulence

This section aims to provide a brief overview of the fundamental concepts of turbulence. For a more in-depth treatment of the subject, the reader is referred to Pope [9] and Davidson [10].

Turbulent flow is characterized by an irregular and chaotic motion, exhibiting a wide range of length scales and contrasting with laminar flow, where the fluid motion is smooth and regular. However, laminar flow is often restricted to highly viscous or low-speed flows and is rarely observed in nature. In fact, turbulence

is ubiquitous in fluid dynamics and influences a vast array of phenomena, from large-scale atmospheric flows to airflow through the human larynx. Consequently, understanding turbulence is essential when dealing with fluid dynamics.

The chaotic behavior of turbulent flows is a direct result of non-linear terms in the NSE. These terms became dominant in the NSE when the Reynolds number increases; indeed, Re is a useful parameter to describe the turbulent behavior of the flow. However, the transition mechanism from laminar to turbulent is extremely complex and is not yet fully understood. In the following sections, only the transition in the boundary layer will be briefly discussed since a thorough discussion of this subject is not the purpose of this study.

In the following subsections, useful statistical quantities and turbulence theories will be discussed.

2.2.1 Statistical description

A common characteristic of turbulence is that the instantaneous velocity field is unpredictable. Any experimental representation of a turbulent flow each time reproduces a different solution, even if the initial and boundary conditions remain unchanged. The reason is that turbulence tends to amplify all those inevitable and very small differences that exist between one realization and another, thus leading to a different result. Although the instantaneous turbulent field is random and unpredictable, the statistical properties seem to be smooth and reproducible. This is why statistical descriptions are used to deal with turbulent flows.

Averages

If a turbulent flow is *statistically stationary*, an useful statistical operation is *time averaging*:

$$\bar{u}(\mathbf{x}) = \lim_{t \rightarrow \infty} \frac{1}{t} \int_0^t u(\mathbf{x}, t') dt'. \quad (2.5)$$

Statistically stationary (or *statistically steady*) means that the statistics are independent of time. This operation has been widely used in this study, since all the flows simulated are statistically steady. In these cases, time averages depend on position in the space but not on time. Two other types of averages exists: the *ensemble average* and the *volume average*. The former is the mean value of a quantity at a given position and given time over a collection of identical systems

$$\langle u(\mathbf{x}, t) \rangle = \lim_{N \rightarrow \infty} \frac{1}{N} \sum_{i=1}^N u_i(\mathbf{x}, t), \quad (2.6)$$

while the latter is the mean value of a quantity over a specific volume

$$\langle u(t) \rangle_V = \lim_{V \rightarrow \infty} \frac{1}{V} \int_V u(\mathbf{x}, t) dV. \quad (2.7)$$

In a statistically steady flow, time average and ensemble average are equivalent. On the other hand, volume average is useful in statistically homogeneous turbulence, i.e. statistical properties do not depend on position. In that case volume average and ensemble average are equivalent.

Statistical tools

Following the discussion and the notation of Pope [9], is possible to introduce a set of quantities useful to characterize a random variable U . In order to do that, an independent variable V is introduced, that is a *sample-space* variable associated to U . Since U is a random variable, the objective of a statistical theory is not to determine the exact value of U , but the probability that a particular event will occur. For example, given the event A like

$$A \equiv \{U < V_a\}, \quad (2.8)$$

the probability of the event A is

$$p = P(A) = \{U < V_a\}. \quad (2.9)$$

p is a real number between 0 and 1, and it represents how much an event is likely to occur. If $p = 0$, the event is impossible, while if $p = 1$ the event is sure. To determine the probability of any event, is possible to use the *cumulative distribution function* (CDF), which is defined by

$$F(V) \equiv P\{U < V\} \quad (2.10)$$

and represent the probability of U being smaller than a specific value of V . This function can be used also to determine the probability that U is between two specific values, for example

$$P\{V_a \leq U < V_b\} = P\{U < V_b\} - P\{U < V_a\} = F(V_b) - F(V_a). \quad (2.11)$$

Starting from the CDF, the *probability density function* (PDF) can be determined:

$$f(V) = \frac{dF(V)}{dV}. \quad (2.12)$$

Using the PDF, the probability of the random variable being in a particular interval is

$$P\{V_a \leq U < V_b\} = F(V_b) - F(V_a) = \int_{V_a}^{V_b} f(V) dV. \quad (2.13)$$

Indeed, the PDF is the probability per unit of distance in the simple space:

$$P\{V \leq U < V + dV\} = F(V + dV) - F(V) = f(V) dV. \quad (2.14)$$

A random variable like U can be completely characterized by its PDF. The *mean* of U , can be computed using PDF:

$$\langle U \rangle \equiv \int_{-\infty}^{\infty} V f(V) dV. \quad (2.15)$$

It is also possible to define the *fluctuation*

$$u \equiv U - \langle U \rangle, \quad (2.16)$$

the *variance*

$$\langle u^2 \rangle = \int_{-\infty}^{\infty} (V - \langle U \rangle)^2 f(V) dV, \quad (2.17)$$

and the *standard deviation*

$$\sigma_u = \sqrt{\text{var}(U)} = \langle u^2 \rangle^{1/2}. \quad (2.18)$$

In general, the n^{th} -order *central moment* is defined by

$$\langle u^n \rangle = \int_{-\infty}^{\infty} (V - \langle U \rangle)^n f(V) dV. \quad (2.19)$$

The central moments with $n = 3$ and $n = 4$ are respectively known as the *skewness factor* and the *flatness factor*.

The concept just expressed for a single random variable U can be extended to two or even more random variable. For example, is possible to consider the random variables $\mathbf{U} = \{U_1, U_2\}$, with the sample-space associated $\mathbf{V} = \{V_1, V_2\}$. In this case the joint CFD is

$$F_{12}(V_1, V_2) \equiv P\{U_1 < V_1, U_2 < V_2\} \quad (2.20)$$

and the joint PDF is

$$f_{12}(V_1, V_2) \equiv \frac{\partial^2}{\partial V_1 \partial V_2} F_{12}(V_1, V_2). \quad (2.21)$$

With two random variables, the mixed 2^{nd} -order moment is called *covariance*, and is defined by

$$\langle u_1 u_2 \rangle = \int_{-\infty}^{\infty} \int_{-\infty}^{\infty} (V_1 - \langle U_1 \rangle)(V_2 - \langle U_2 \rangle) f_{12}(V_1, V_2) dV_1 dV_2. \quad (2.22)$$

The ratio of the covariance divided by the product of the variance of both variables is called the *correlation coefficient*:

$$\rho_{12} \equiv \langle u_1 u_2 \rangle / [\langle u_1^2 \rangle \langle u_2^2 \rangle]^{1/2}. \quad (2.23)$$

It describes the mutual influence between U_1 and U_2 . For the *Cauchy-Schwartz inequality*

$$-1 \geq \rho_{12} \geq 1. \quad (2.24)$$

If $\rho_{12} = 1$ then the two variables are *perfectly correlated*, if $\rho_{12} = -1$ then they are *perfectly negatively correlated*. If U_1 and U_2 are independent, then $\rho_{12} = 0$.

To apply this concept to the turbulence, is possible to define the velocity $\mathbf{U}(\mathbf{x}, t)$ as a random vector field time-dependent, with components (U_X, U_Y, U_Z) . In order to study the spatial structure of this random field, the two-point, one-time autocovariance (also known as *two-point correlation*) can be used:

$$R_{ij}(\mathbf{r}, \mathbf{x}, t) \equiv \langle u_i(\mathbf{x}, t) u_j(\mathbf{x} + \mathbf{r}, t) \rangle. \quad (2.25)$$

It is a simple statistic, closely related to the covariance, which allows to determine how much speed is correlated in two points of the space. Therefore, in some way, it allows to obtain information on the size and energy of the turbulent structures contained in the flow. From R_{ij} , it is possible to deduce a set of integral length scales,

which also gives information about the influence of the velocity field in different point in the space. An example of integral length scale is

$$L_{ZZ}(\mathbf{x}, t) \equiv \frac{1}{R_{ZZ}(0, \mathbf{x}, t)} \int_0^\infty R_{ZZ}(\mathbf{e}_Z r, \mathbf{x}, t) dr \quad (2.26)$$

where \mathbf{e}_Z constitutes the unit vector in the z -direction. Another useful parameter is the velocity spectrum tensor, which is the Fourier transform of the two-point correlation

$$\Phi_{ij}(\mathbf{k}, t) = \frac{1}{(2\pi)^3} \iiint_{-\infty}^{\infty} e^{-i\mathbf{k}\cdot\mathbf{r}} R_{ij}(\mathbf{r}, t) d\mathbf{r}, \quad (2.27)$$

and represent the contribution to the covariance $\langle u_i u_j \rangle$ of velocity modes with wavenumber \mathbf{k} . Another parameter expressed in terms of wavelength spectrum is the *energy spectrum function*:

$$E(k, t) \equiv \iiint_{-\infty}^{\infty} \frac{1}{2} \Phi_{ii}(\mathbf{k}, t) \delta(|\mathbf{k}| - k) d\mathbf{k}. \quad (2.28)$$

$E(k, t)$ represent the energy, at a given time, related to a specific wavelength, but without the directional information of $\Phi_{ij}(\mathbf{k}, t)$.

RANS and closure modeling

Since the statistical properties of a turbulent velocity field are smooth and reproducible, it would be useful to derive dynamical equations for these statistical quantities. A simple idea to obtain an average velocity field, could be to mediate the NSE. Unfortunately, since such equations are non-linear, there will be more statistical unknowns than equations. A way to average the NSE is to decompose the parameters into a sum of their mean and fluctuation

$$u(\mathbf{x}, t) = \bar{u}(\mathbf{x}, t) + u'(\mathbf{x}, t) \quad (2.29)$$

and then average the equations. For example, the unsteady momentum conservation equation would be

$$\frac{\partial(\rho \bar{u}_i)}{\partial t} + \frac{\partial(\rho \bar{u}_i \bar{u}_j)}{\partial x_j} = -\frac{\partial \bar{p}}{\partial x_i} + \frac{\partial}{\partial x_j} (\bar{\tau}_{ij} - \overline{\rho u'_i u'_j}), \quad (2.30)$$

where

$$\bar{\tau}_{ij} = \mu \left(\frac{\partial \bar{u}_i}{\partial x_j} + \frac{\partial \bar{u}_j}{\partial x_i} - \frac{2}{3} \delta_{ij} \frac{\partial \bar{u}_k}{\partial x_k} \right). \quad (2.31)$$

By applying this approach to the NSE, the Reynolds averages Navier-Stokes (RANS) can be obtained. However, in the Equation 2.30 there is the averaged product of the velocity fluctuations $(-\overline{\rho u'_i u'_j})$, also know as *Reynolds stress*, which is an additional unknown variable. This means that averaging the NSE leads to a not closed system of equations. In general, this is known as the *closure problem of turbulence*. However, closure relations are not exact and an empirical modeling is necessary. Many models exist, anyway they invokes non-rigorous hypotheses and have limited range of use.

A possible alternative to modeling is to solve the three-dimensional, time-dependent NSE, by direct numerical simulation (DNS). For this study, DNS has been employed; however, it is worth to keep in mind that DNS are extremely computational expensive and not practicable in most flows of engineering interest.

2.2.2 Scales of turbulence

Turbulent flows are characterized by coherent flow structures, known as eddies, which correspond to organized regions of vorticity. The latter is defined as

$$\boldsymbol{\omega} = \nabla \times \mathbf{u}. \quad (2.32)$$

Richardson's theory

Base on Richardson [11], turbulence is a superposition of a broad spectrum of eddy sizes. The largest eddies are created by inertial instabilities of the mean flow and they contain most of the kinetic energy. These large eddies are in some way instable and break up due to the effect of inertial forces. In this process the energy is transferred to smaller eddies, which are instable as well, and consequently their energy is passed to even smaller eddies. This concept has been called *energy cascade* by Richardson. In this process, the large eddy Re is sufficiently high and the viscosity is negligible. Indeed, the cascade is driven only by inertial forces and the energy is not dissipated, but passed from large to small scales. The cascade stops when the eddies become so small that their Re is of the order of unity. As a result, viscosity is not negligible anymore and energy starts to be dissipated. In summary, turbulent energy is distributed across a wide range of length scales. The largest scales contain most of this energy, while dissipation is dominated by small scales (see Figure 2.1).

Following the discussion of Davidson [10], we define the Re of largest eddies as

$$Re = \frac{u \cdot l_0}{\nu} \quad (2.33)$$

while the Re of smallest eddies is

$$\frac{v \cdot \eta}{\nu} \sim 1 \quad (2.34)$$

l_0 and η are, respectively, the length scales of the largest and the smallest structures, while u and v are, respectively, the velocities of the two scales. ν is the kinematic viscosity, [m²/s]. The rate at which the energy is passed from the largest scales to the smaller is

$$\Pi = \frac{[energy]}{[turnover\ time]} \sim \frac{u^2}{l_0/u} = \frac{u^3}{l_0} \quad (2.35)$$

In statistically steady condition, Π has to be equal to the rate of dissipation of energy, that is $\epsilon \sim \nu(v^2/\eta^2)$. Using this similarity

$$\frac{u^3}{l_0} \sim \nu \frac{v^2}{\eta^2} \quad (2.36)$$

and the fact that the Re for the smallest scales is of the order of unity, is possible to find that

$$\eta \sim l_0 \cdot Re^{-\frac{3}{4}}, \quad (2.37)$$

$$v \sim u \cdot Re^{-\frac{1}{4}}. \quad (2.38)$$

η and v are called *Kolmogorov microscales* of turbulence, while l_0 is called the *integral scale*. From these equations is possible to understand that the length scales of the smallest eddies decrease if Re increases. This is why capturing all the eddies in a flow with high Re with a numerical simulation is so difficult.

Kolmogorov's theory

Another great improvement in the understanding of turbulence has been done thanks to Kolmogorov in 1941 [12]. Following the discussion of [13], Kolmogorov developed three main hypotheses for turbulent flows with $Re \gg 1$:

1. **Hypothesis of local isotropy:** the directional information is lost at the smallest scales. It means that for scales $l \ll l_0$ (where l_0 is the integral scale), the turbulence statistics are isotropic. In this condition, the velocity spectrum tensor $\Phi_{ij}(\mathbf{k})$ is completely determined by the energy spectrum function $E(k)$.
2. **First similar hypothesis:** the turbulence statistics for the smallest scales ($l \ll l_{EI}$) are universal and depend only on ν and ϵ . It is possible to define the scale $l_{EI} \sim l_0/6$, such that $l < l_{EI}$ is the *universal equilibrium region*. In this region, the energy spectral function can be written as

$$E(k) = \epsilon^{2/3} k^{-5/3} \Psi(k\eta), \quad (2.39)$$

where $\Psi(k\eta)$ is the *universal Kolmogorov compensated spectrum function*.

3. **Second similarity hypothesis:** for $l_{EI} \gg l \gg \eta$, the turbulence statistics depend only on ϵ . It is possible to define l_{DI} , such that $l_{EI} > l > l_{DI}$ is the *inertial subrange* and $l < l_{DI}$ is the *dissipation subrange*. In the inertial subrange, the energy spectrum function can be written as

$$E(k) = C \epsilon^{2/3} k^{-5/3}, \quad (2.40)$$

where

$$C = \lim_{k\eta \rightarrow 0} \Psi(k\eta). \quad (2.41)$$

Figure 2.1 shows a simple schematic of the wavenumbers related to the different scales and the regions just discussed, with also the $E(k)$ distribution.

2.2.3 Other parameters of turbulence and Taylor's hypothesis

Turbulence parameters

In Equation 2.30, is possible to see that when decomposing the parameters of the NSE into their mean and fluctuating components, and then averaging the equations, some new and unknown statistical parameters appear: the Reynolds stresses. These additional stresses lead to an increased momentum transport in turbulent flows. They are a direct consequence of turbulent fluctuation and can be represented through a symmetric tensor: the *Reynolds stress tensor*

$$\bar{\tau}_R = -\rho \begin{bmatrix} \overline{u'u'} & \overline{u'v'} & \overline{u'w'} \\ \overline{v'u'} & \overline{v'v'} & \overline{v'w'} \\ \overline{w'u'} & \overline{w'v'} & \overline{w'w'} \end{bmatrix}. \quad (2.42)$$

The variables u' , v' and w' denote the fluctuating velocity components in the x , y , and z directions, respectively. In general, $\bar{\tau}_R$ will be used in this study for analyze some features of the turbulent flows, for example the isotropy.

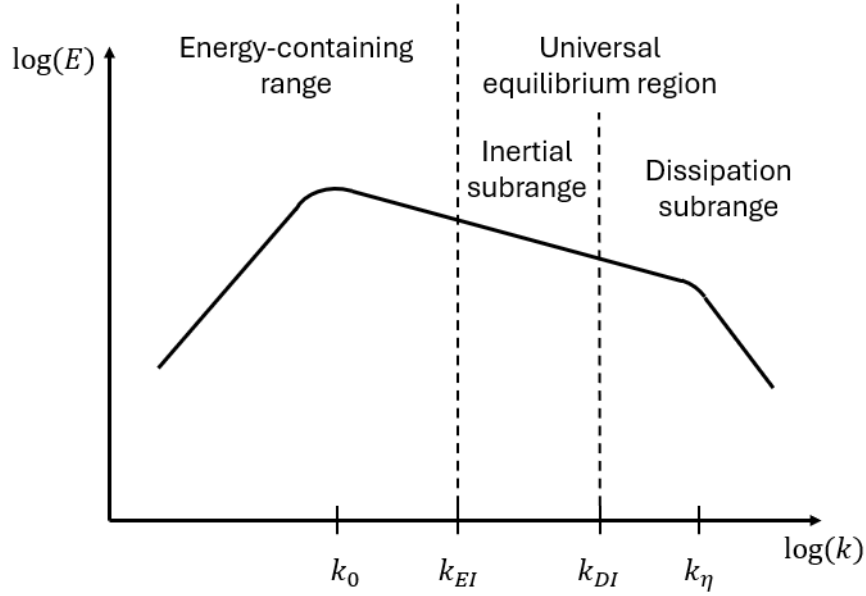


Figure 2.1: Typical energy spectrum for homogeneous isotropic turbulence

Another parameter largely used in this study is the turbulent kinetic energy (TKE). It has no directional information and characterizes the magnitude of kinetic energy in the flow related to the turbulence. TKE can be calculated as the integral on all modes of the energy spectral function or equivalently as half of the Reynolds stress tensor trace:

$$TKE = \int_0^{\infty} E(k) dk = \frac{1}{2} \overline{u'_i u'_i}. \quad (2.43)$$

TKE can be normalized with the free-stream velocity of the flow U_{∞} , in order to obtain the turbulence intensity (TI):

$$TI = \sqrt{\frac{2 TKE}{3 U_{\infty}^2}} = \sqrt{\frac{1}{3} \frac{\overline{u'_i u'_i}}{U_{\infty}^2}}. \quad (2.44)$$

As for TKE, TI is used to characterize the magnitude of the turbulent content of the flow and is usually reported as a percentage.

Taylor's hypothesis

Another crucial hypothesis extensively utilized in this study is the *frozen-turbulence* approximation, also known as *Taylor's hypothesis* [14]. Under this hypothesis, is possible to convert a time signal in a specific point into a spatially coherent signal, using the convection velocity U_c . This approximation, which assumes a homogeneous flow, becomes more accurate as the time it takes for a fluid particle to convect past a given point becomes much smaller than the characteristic time scale of the turbulent eddies. Following the discussion of Durbin and Rief [15], for the large scales, the condition translates to

$$\frac{\sqrt{k}}{U_c} \ll 1, \quad (2.45)$$

implying that the turbulence intensity has to be small (k is the turbulent energy). For small scales, the condition is given by

$$R_T^{-\frac{1}{4}} \frac{\sqrt{k}}{U_c} \ll 1, \quad (2.46)$$

where R_T is the turbulent Reynolds number, defined as

$$R_T \equiv \frac{k^2}{\epsilon \nu}. \quad (2.47)$$

For the smallest scales, the main challenge often lies in the accuracy of the probes rather than in the validity of the hypothesis.

The turbulence injection process used for the numerical simulations in this study is based on Taylor's hypothesis (see Chapter 6).

2.3 Boundary layer

The first who introduced the concept of boundary layer (BL) was L. Prandtl in 1904 [16]. According to him, the flow past a body can be divided in two regions: a thin layer close to the body, i.e. the boundary layer (also known as the *friction layer*), and the remaining region outside. Due to the no-slip condition, the velocity has to be zero on the surface of the body, thus the velocity gradient near the body can be high. Therefore, even if a fluid has very small viscosity, the viscous forces cannot be neglected in the boundary layer, while they can be neglected outside. This Prandtl's theory allowed to overcome the strong discrepancy between classical hydrodynamics and experimental evidence; in fact, it is considered a keystone of modern fluid mechanics.

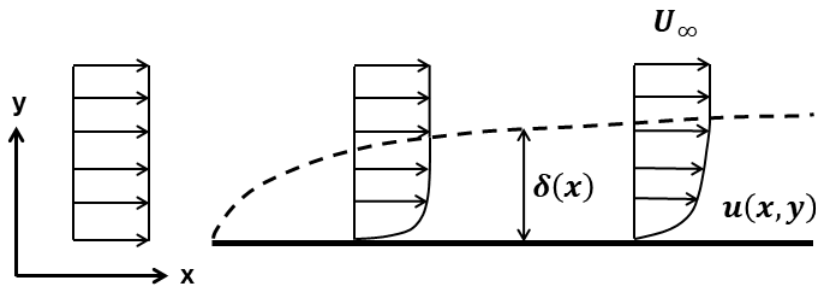


Figure 2.2: Boundary layer developing on a flat plate at zero incidence

Figure 2.2 shows the simple case of a boundary layer developing on a flat plate at zero incidence. U_∞ is the velocity outside the BL, while $u(x, y)$ is the velocity inside. In a more general case, the outer velocity is a function of the x ($U_e(x)$). It can be seen that $u = 0$ on the wall (i.e. $y = 0$) and it increases along the y -direction. δ represents the BL thickness, which increases along the x -direction. However, δ is an artificial concept and usually, for each x -position, δ is arbitrarily set at the point where the u reaches the 99% of U_∞ .

The velocity gradient on the wall is particularly important because is directly proportional to the wall shear stress:

$$\tau_w = \mu \left(\frac{\partial u}{\partial y} \right)_{y=0}. \quad (2.48)$$

The shear stress represent the tangential force generated by the flow on the surface and can be integrated on the whole wall to determine the friction drag. By using a reference dynamic pressure, a dimensionless wall shear stress, namely the *friction coefficient*, can be obtained:

$$c_f = \frac{\tau_w}{\frac{1}{2}\rho_0 U_0^2}. \quad (2.49)$$

Following the discussion of Schlichting and Gersten [17], in addition to δ and τ_w , other physical quantities useful to describe a BL can be introduced:

- the displacement thickness δ^* , which quantifies the streamline displacement due to the presence of the BL:

$$\delta^*(x) = \int_0^\infty \left(1 - \frac{\rho}{\rho_e} \frac{u}{U_e} \right) dy, \quad (2.50)$$

where the subscript "e" refers to quantities outside the BL;

- the momentum thickness θ , which quantifies the drag:

$$\theta(x) = \int_0^\infty \frac{\rho}{\rho_e} \frac{u}{U_e} \left(1 - \frac{\rho}{\rho_e} \frac{u}{U_e} \right) dy; \quad (2.51)$$

- the shape factor H , which describe the state of the BL:

$$H = \frac{\delta^*}{\theta}, \quad (2.52)$$

where for $H > 2$ the BL is laminar while for $H < 2$ (typically around 1.4) it is turbulent.

The remaining subsections of this chapter will delve deeper into specific aspects of boundary layer theory. Firstly, the phenomenon of boundary layer transition will be explored, including the factors that trigger it and the mechanisms involved. Secondly, boundary layer separation will be discussed, focusing on its identification and prediction. Lastly, the universal characteristics of the near-wall region of the boundary layer will be highlighted, leading to the formulation of the universal law of the wall.

2.3.1 Laminar-turbulent transition

The interaction between flow and body is strongly affected by the boundary layer regime. Therefore, predicting and controlling the transition from laminar to turbulent is of particular interest. In addition to the Reynolds number, the transition of the BL depends on many parameters, some of the most important are the outer pressure distribution, the wall roughness and the free-stream TI.

Following the discussion of [17], Figure 2.3 shows the different transition stages from laminar to turbulent in a simple case with a flat plate at zero incidence:

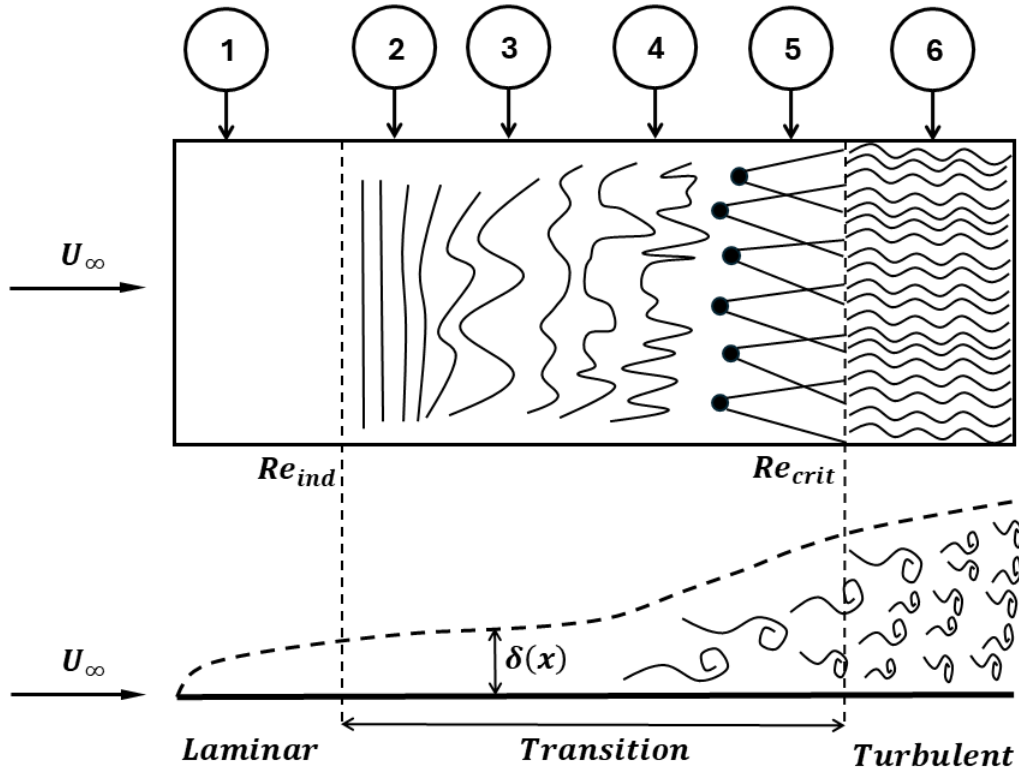


Figure 2.3: Sketch of transition in the boundary layer on a flat plate at zero incidence (reproduced from [17])

1. initially the BL is laminar and stable;
2. the transition is initiated by axisymmetric waves called *Tollmien-Schlichting waves* (TS) where the Reynolds number reach a value called *indifference Reynolds number* (Re_{ind});
3. the two-dimensional TS waves are unstable and lead to the formation of three-dimensional waves and vortex;
4. the three-dimensional structures start to decay;
5. this decay leads to the generation of turbulent spots at arbitrary positions;
6. the BL reaches a fully turbulent regime when the Reynold number reaches the critical value (Re_{crit}).

Looking at the bottom part of the sketch, it is also possible to see that the BL thickness strongly increases during the transition. Further, the time averaged velocity profile changes as well (see Figure 2.4).

The velocity gradient on the wall is higher for the turbulent regime; therefore, the wall shear stress is higher in a turbulent BL compared to a laminar BL, leading to higher friction drag.

In order to predict the transition of the boundary layer, several theoretical models have been developed. Usually, in these methods the flow is decomposed into a

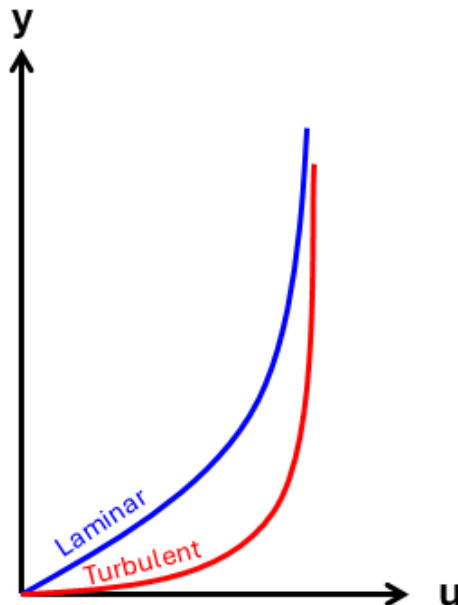


Figure 2.4: Time averaged velocity profiles for laminar and turbulent regime

laminar basic flow and superimposed perturbations, which are much smaller than the basic flow. The general idea behind the stability theory of laminar flows is that if the perturbations increase in time, the basic flow is unstable; if the perturbations decrease in time, the basic flow is stable.

According to [17], two different methods can be used: the *energy method* and the *method of small disturbance*. The first method focuses on the rate of change of the energy of the perturbation, but it has been proved to be unsuccessful. On the other hand, the second method focuses only on the perturbations consistent with the hydrodynamic equations of motion, which progression in time is traced. These perturbations are modeled by modes which represent waves propagating in the x -direction. The resulting ordinary differential equation is known as *Orr-Sommerfeld equation*.

However, this linear stability theory is not able to predict all the non-linear effect that contribute to the transition. In the reality, the transition can be triggered in many different ways and the most common are:

- natural transition, which is the mechanism represented in Figure 2.3 and represent typically the slowest one;
- bypass transition, where, due to free-stream TI or other disturbances, the first 3 steps of the natural transition are skipped and thus the process is faster;
- separated flow transition, where the large shear stresses generated by velocity differences in the free shear layer trigger the transition (a free shear layer is a shear layer that is not adjacent to a boundary);
- forced transition, where the mechanism is artificially accelerated by surface imperfections or specific devices.

It can also happen that the reverse process occurs, i.e. the flow passes from turbulent to laminar regime. The process in question is called *relaminarization*

and is usually observed in cases of favorable pressure gradients, that is a negative pressure gradient along the flow direction.

2.3.2 Separation

The boundary layer separation occurs when the flow within it reverses direction. This phenomenon is common in diverging geometries, when there is an adverse pressure gradient (that is a positive pressure gradient along the flow direction). The location where the downwards and upwards moving flows meet is called separation point. In this point the velocity gradient on the wall is zero, therefore the wall shear stress is zero as well:

$$\tau_w = \mu \left(\frac{\partial u}{\partial y} \right)_{y=0} = 0 \quad (\text{at the separation point}). \quad (2.53)$$

The separation leads to a strong thickening of the boundary layer and a flow mass transported from the wall to the outer flow.

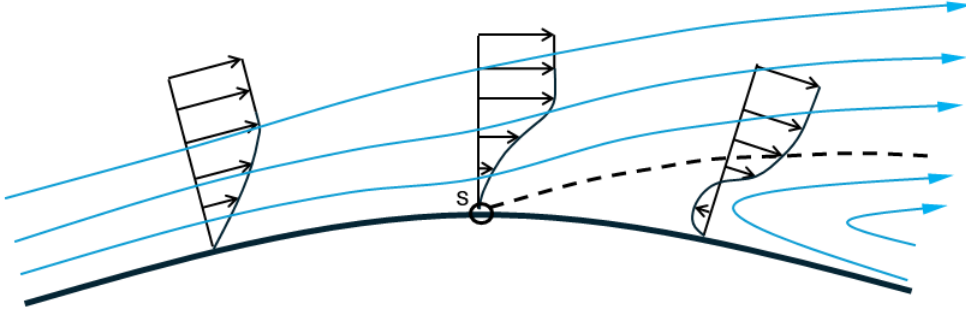


Figure 2.5: Boundary layer separation on a curved surface

Figure 2.5 shows a typical BL separation on a curved surface, where the separation point is indicated with **S**. The dotted line starting from **S** is the free shear layer.

In many applications, the separation of the boundary layer is undesirable, since it is detrimental for the aerodynamic efficiency due to high energy losses. This is why usually streamwise bodies are preferred over bluff bodies, because they allow the flow to smoothly pass around.

Another aspect to consider is the regime of the flow: a laminar boundary layer tends to separate easier than a turbulent one. In the second case, the energizing action of the outer flow on the boundary layer is higher. Indeed, although the friction drag is higher for a turbulent regime, in some cases it is preferred over a laminar one, because the separation point is moved further downstream and sometimes completely avoided. Furthermore, laminar separation can trigger the separated flow transition (see Subsection 2.3.1), leading the BL to become turbulent and to reattach to the surface. The resulting recirculation area is also known as *separation bubble*.

Since the pressure gradient greatly affects the separation, an useful quantity to predict the phenomenon is the *acceleration parameter*:

$$K = \frac{\nu}{U^2} \frac{dU}{ds}, \quad (2.54)$$

where s is the curvilinear coordinate tangential to the surface. Positive values of K mean that the local velocity is increasing and the pressure gradient is favorable, while for negative values the local velocity is decreasing and the pressure gradient is adverse. Therefore, with $K < 0$ the BL risk of separate, while for $K > 0$ the risk is lower. If there is a positive value of K large enough, a separated boundary layer can reattach, and even experience relaminarization if it was turbulent.

A last consideration about the separation region is its variation in time: a laminar separation region is usually steady and well-defined in time, while a turbulent one can behave highly unsteady.

2.3.3 Universal law of the wall

Following the discussion of [17], for large Reynolds number flows, the boundary layer can be split in two regions: a large *core layer* where the molecular momentum transfer can be neglected compared to the turbulent momentum transfer, and a thin *wall layer* where both momentum transfer are considered. Several experiments show that the velocity distribution inside this wall layer appear to be universal. This *universal law of the wall* is usually described using dimensionless quantities called dimensionless wall units. The reference velocity for wall units is the *friction velocity* (or more correctly *wall friction velocity*)

$$u_\tau = \sqrt{\frac{\bar{\tau}_w}{\rho}}, \quad (2.55)$$

while the reference length is the *wall layer thickness*

$$\delta_v = \frac{\nu}{u_\tau}. \quad (2.56)$$

Consequently there are the dimensionless velocity

$$u^+ = \frac{\bar{u}}{u_\tau}, \quad (2.57)$$

and the dimensionless characteristic wall coordinate

$$y^+ = \frac{y}{\delta_v}. \quad (2.58)$$

Therefore, the velocity distribution in the wall layer has the form $u^+ = f(y^+)$, however, the equation is not the same in the entire wall layer. In order to find a formulation for $u^+(y^+)$, the wall layer can be further subdivided in three more regions (see Figure 2.6). These regions are:

- the pure viscous sublayer: $0 \leq y^+ < 5$;
- the buffer layer: $5 < y^+ < 70$;
- the overlap layer: $y^+ > 70$.

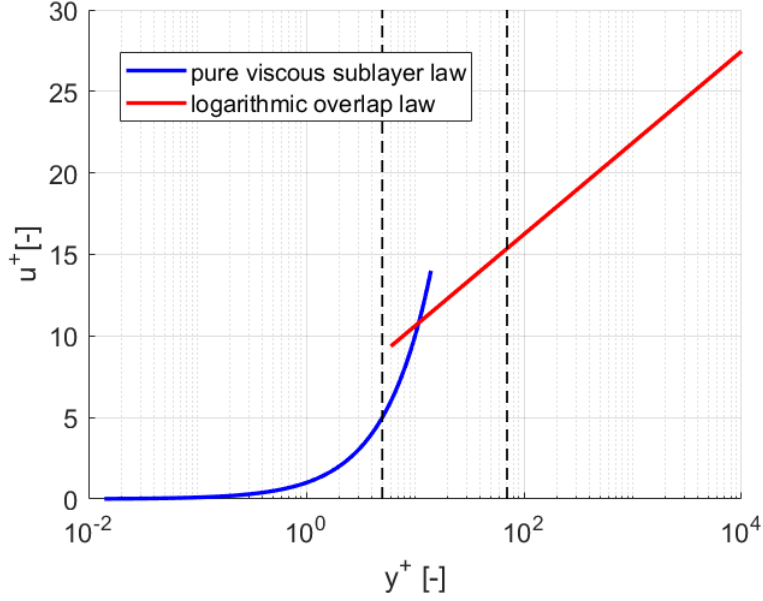


Figure 2.6: Velocity distribution in the wall layer

In the pure viscous sublayer is dominated by viscosity and the flow is laminar. The velocity distribution in this region is

$$u^+ = y^+. \quad (2.59)$$

In the overlap layer, the velocity distribution is given by the *logarithmic overlap law*:

$$u^+ = \frac{1}{k} \ln y^+ + C^+, \quad (2.60)$$

where the constant k is called the *Karman constant* and is equal to 0.41, while C^+ is the constant of integration and depends by the wall roughness (e.g. $C^+ = 5.0$ in a smooth wall).

In the buffer layer, the velocity distribution is given by a combination of the two adjacent layers.

Lastly, the dimensionless wall coordinates for a general surface can be introduced:

$$n^+ = \frac{n}{\delta_v}, \quad s^+ = \frac{s}{\delta_v}, \quad (2.61)$$

where n and s are respectively the normal distance from the wall and the tangential distance along the surface.

2.4 Wake

The relative motion between a body and a fluid flow can generate a wake. The latter is a complex phenomenon affected by various factors, for example, the geometry of the body and the Reynolds number. Usually, the wake is a region with high vorticity and turbulence, which can have a major impact on the flow field downstream of the body and also on the forces exchanged between the latter and the flow.

Indeed, understanding the wake is of fundamental importance in many engineering applications.

Following the discussion of Kundu and Cohen [18], this section will briefly describe the flow past a circular cylinder for a wide range of Reynolds numbers (which is defined $Re = U_\infty d/\nu$ using the free stream velocity and the cylinder diameter). Since the trailing edge of the turbine blade employed in this study has a circular shape, similar phenomena are observed between the two geometries.

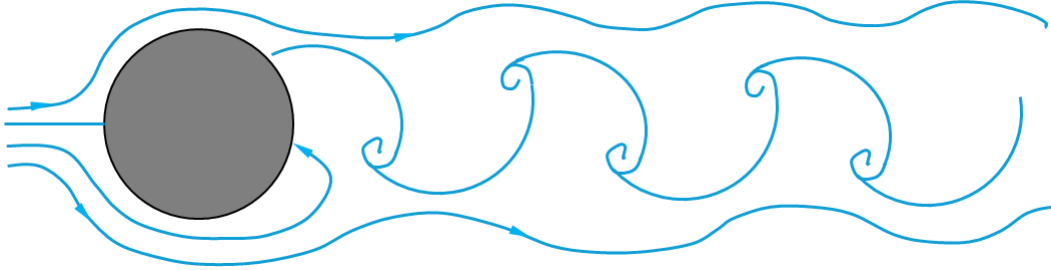


Figure 2.7: Sketch of a typical von Karman vortex street for a circular cylinder in a flow with $80 < Re < 200$ (reproduced from [18])

For $Re < 1$, the vorticity generated on the BL by the no-slip condition is simply diffused and not advected. Then, for $Re > 1$, the vorticity starts to be confined behind the cylinder due to the increasing advection effect. For $Re > 4$, two standing small eddies appear attached behind the cylinder. For $Re > 40$, the wake becomes unstable, with slow velocity oscillations that are periodic in time and with the amplitude increasing downstream. The resulting unstable wake has two staggered rows of vortices with opposite sense of rotation. This phenomenon has been investigated by von Karman, who concluded that wakes with nonstaggered rows of vortices are unstable, while staggered rows are stable if the ratio of the lateral distance to the longitudinal distance between the vortices is 0.28. This staggered row of vortices is known as *von Karman vortex street* and is a dominantly two-dimensional phenomenon. For $Re > 80$, the vortex street start to interact with the small eddies attached behind the cylinder, which start to periodically break off alternately (see Figure 2.7). This flow regime is characterized by an oscillating lateral force, which may damage the structure if the natural frequency of the body is close to the *vortex shedding* frequency. The latter can be described using the adimensional *Strouhal number*:

$$St \equiv \frac{f \cdot d}{U_\infty}, \quad (2.62)$$

where f is the frequency. For circular cylinders, St is close to 0.21 for a wide range of Reynolds numbers [18]. For a general geometry, St can be defined using a characteristic length L instead of d . Furthermore, St is also equal to the ratio of the *Roshko number* (Ro) to Re :

$$St = \frac{Ro}{Re}. \quad (2.63)$$

Following the empirical correlation of Ro for a cylinder [19], St expression becomes:

$$St = 0.212 \left(1 - \frac{12.7}{Re} \right). \quad (2.64)$$

Increasing the Re further leads to a fully turbulent wake; however, the BL remains laminar for $Re < 3 \cdot 10^5$. In this regime flow tends to separate from the surface and the drag is high due to the asymmetry in the pressure distribution. In fact, the pressure in the wake is almost constant and lower compared to the free-stream conditions. For a circular cylinder, the critical value of Re is around $3 \cdot 10^5$, thus the BL over this number tends to become turbulent. As discussed in Section 2.3, a turbulent BL is less prone to separation. As a consequence, the separation point moves downstream and the drag is decreased. However, the Re_{cr} is strongly dependent by the free-stream TI and the roughness of the body surface. Indeed, the value $3 \cdot 10^5$ is related to a low free stream TI and a smooth surface. In general, the wake depends by the BL regime and the transition may have a beneficial effect on the flow, especially in situations where the BL is likely to separate.

Chapter 3

Low pressure turbine features

This chapter provides a range of key concepts for understanding the results of the high-speed low-pressure turbine presented in this study. The turbine under investigation is modeled as a linear cascade, composed of SPLEEN airfoils. Firstly, the geometrical parameters encompassing both the individual SPLEEN airfoil and the complete cascade are presented. Secondly, the most common parameters related to the operating conditions and performance of turbine blades and cascades in general are introduced. Subsequently, a method for evaluating losses in turbomachinery is briefly discussed, with a particular focus on the possible sources of losses. Lastly, the importance of boundary layer separation and transition in turbines is highlighted, as well as the combined effect of the two phenomena and how they can strongly affect the performance of the turbomachine.

3.1 Geometrical parameters

In the field of cascade design, there are some common parameters used to describe the geometry. Figure 3.1 shows a schematic of a low pressure turbine cascade composed of SPLEEN blades with some of these key parameters.

The parameters are:

- c : *true chord*, which describe the distance between the leading edge (LE) and the trailing edge (TE) of the blade;
- λ : *stagger angle*, defined as the angle between the true cord direction and the axial direction;
- c_{ax} : *axial chord*, which is the projection of the true chord in the streamwise direction ($c_{ax} = c \cdot \cos \lambda$) and gives a length of reference for the size of the blade;
- g : *pitch*, defined as the distance between corresponding points on two adjacent blades in a cascade;
- α'_1 and α'_2 : *metal angles* respectively for the LE and the TE, defined as the angle between the streamwise direction and the blade tangent in the point considered.

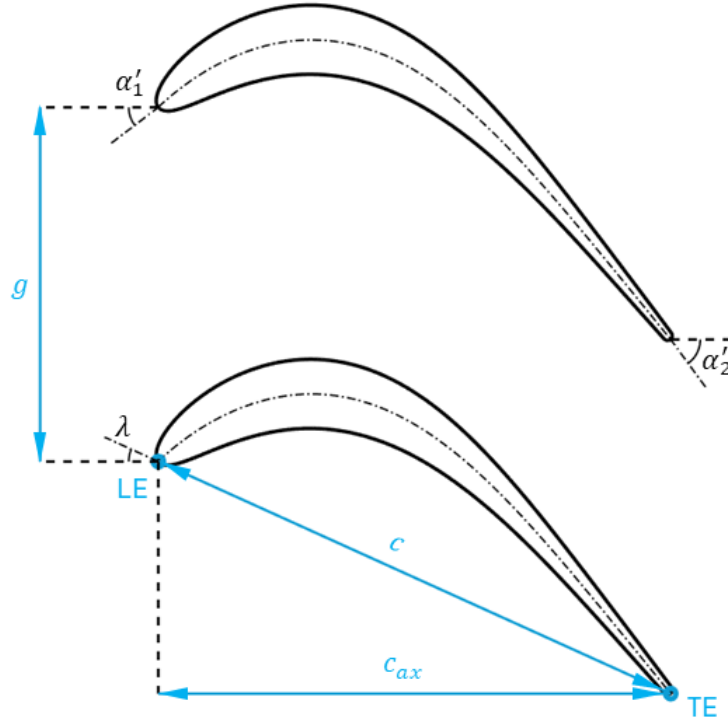


Figure 3.1: Schematic of the geometrical parameters for LPT cascade with SPLEEN blades

Parameter	Unit	Value
c	[mm]	52.28
λ	[°]	24.40
c_{ax}	[mm]	47.61
g	[mm]	32.95
α'_1	[°]	37.30
α'_2	[°]	53.80

Table 3.1: Geometrical parameter of the SPLEEN blade

The geometrical parameter of the SPLEEN blade, which has been used in this study, are presented in Table 3.1.

Another important geometrical parameter is the *throat opening width* w , which is the minimum distance between two adjacent blades and determines the maximum flow rate through the cascade for a given physical state of flow. For the SPLEEN blade $w = 19.40$ mm. Additional geometrical parameters can be derived from the previous ones, which are the *solidity* $\sigma = c/g$ and the *camber angle* $\theta = \alpha'_1 + \alpha'_2$. The metal angles are positive if they are like in Figure 3.1.

In general, the direction of the flow can be different from the blade tangents at the LE and the TE. Therefore, the *flow angles* can be defined: α_1 and α_2 , which are the angles between the axial direction and flow velocity at the inlet and the outlet of the cascade, respectively. The difference between the metal and the flow angles is called *incidence angle* at the LE ($i = \alpha_1 - \alpha'_1$) and *deviation angle* at the TE ($\delta = \alpha'_2 - \alpha_2$). Moreover, the difference between the two flow angles is called *turning angle* $\epsilon = \alpha_1 - \alpha_2$ and represent the change of the flow direction induced by the

blade.

Since the TE of the SPLEEN blade is designed in a circular shape, a last geometrical parameter is its characteristic diameter t , which is 0.87 mm. This parameter is useful to predict the characteristics of the wake generated by the blade and related losses.

3.2 Operating conditions parameters

Usually, in order to define the operating conditions of a turbine cascade, four dimensionless numbers are used: the inlet and outlet flow angles (α_1 and α_2), the isentropic Reynolds number at the outlet and the isentropic Mach number at the outlet. The last two are defined as:

$$M_{is,out} = \sqrt{\frac{2}{\gamma - 1} \left[\left(\frac{p_{in}^0}{p_{out}} \right)^{\frac{\gamma-1}{\gamma}} - 1 \right]}, \quad (3.1)$$

$$Re_{is,out} = \frac{\rho_{is,out} U_{is,out} c}{\mu(T_{out})}. \quad (3.2)$$

p_{in}^0 and p_{out} are the total pressure at the inlet and the static pressure at the outlet, while $Re_{is,out}$ is defined using the outlet isentropic quantities. Conventionally, to define the operating conditions of a compressor cascade are used inlet quantities instead of outlet ones.

The SPLEEN simulation discussed in this study focus only on one of the three cases analyzed by Deneffe [7], which is the one with $Re_{is,out} = 70 \cdot 10^3$ and $M_{is,out} = 0.70$. However, the most common way to define the operating conditions in numerical simulation of turbine cascades is by total temperature and pressure at the inlet (T_{in}^0 and p_{in}^0), flow angle at the inlet (α_{in}) and static pressure at the outlet (p_{out}). Table 3.2 shows the value related to the SPLEEN operating condition analyzed in this study.

Quantity	Unit	Value
T_{in}^0	[K]	300
p_{in}^0	[Pa]	10779.39
α_{in}	[°]	36.3
p_{out}	[Pa]	7771.1645

Table 3.2: Operating conditions for the SPLEEN simulation

3.3 Performance parameters

There are several parameters used to describe the performance of a turbine blade. Probably, the most important are related to the blade loading, which refers to the work extracted by the blade and how this work is distributed. One of these parameter is the *pressure coefficient*:

$$c_p = \frac{p - p_{out}}{\frac{1}{2} \rho_{out} U_{out}^2}. \quad (3.3)$$

which gives the pressure distribution on the blade p , using p_{out} as a reference pressure and the dynamic pressure at the outlet $\frac{1}{2}\rho_{out}U_{out}^2$ to make the parameter dimensionless. Another way to represent the pressure distribution around the blade is by the isentropic Mach number:

$$M_{is} = \sqrt{\frac{2}{\gamma - 1} \left[\left(\frac{p_{in}^0}{p} \right)^{\frac{\gamma-1}{\gamma}} - 1 \right]}. \quad (3.4)$$

In addition to the pressure acting in the normal direction of the surface, the flow exerts aerodynamic forces on the blade also in the tangential direction. These forces are described by the wall shear stress τ_w (see Equation 2.48) or, more commonly, by the skin-friction coefficient:

$$c_f = \frac{\tau_w}{\frac{1}{2}\rho_{out}U_{out}^2} \quad (3.5)$$

where τ_w is made dimensionless using the dynamic pressure at the outlet. This parameter is useful to calculate the aerodynamic friction, but also to find any separation point (see Subsection 2.3.2).

Since the blades have an optimal inlet flow angle, another performance parameter is the average outflow angle. Indeed the inlet flow angle of a cascade is determined by the outflow angle of the previous one. A deviation from the design value of the angle can be highly detrimental for the turbine.

Probably, the most important performance parameter for gas turbine engines is the *efficiency*. The latter is used to quantify the portion of energy extracted respect to the maximum available:

$$\eta_t = \frac{h_{in} - h_{out}}{h_{in} - h_{is,out}}, \quad (3.6)$$

where h is the enthalpy.

Lastly a *loss coefficient* can be defined. Several of them exist, but probably the most common is the *total pressure loss coefficient*, defined by

$$\zeta = \frac{p_{in}^0 - p_{out}^0}{p_{out}^0 - p_{out}}. \quad (3.7)$$

3.4 Sources of losses

Following the discussion of Denton [20], one effective method of measuring losses in an adiabatic machine is through entropy creation. This method is particularly convenient because entropy generation does not depend on the reference of frame. Using the perfect gas hypothesis, the entropy variation can be written as

$$\Delta s = s - s_{ref} = c_p \ln \frac{T}{T_{ref}} - R \ln \frac{p}{p_{ref}}, \quad (3.8)$$

where c_p is the specific heat capacities with constant pressure. Since the change from static to total condition is isentropic, Equation 3.8 can be written using also

total temperature and pressure. In addition, in an adiabatic machine, the total temperature is constant and the equation becomes

$$\Delta s = s_2 - s_1 = -R \ln \frac{p_2^0}{p_1^0}. \quad (3.9)$$

For small total pressure changes, the equation is

$$\Delta s \approx -R \frac{\Delta p^0}{p^0}, \quad (3.10)$$

therefore the entropy generation is directly linked to the total pressure loss. Furthermore, the efficiency can be also closely obtained from entropy creation by

$$\eta_t \approx \frac{h_1 - h_2}{h_1 - h_2 + T_2 \Delta s}. \quad (3.11)$$

According to [20], the main sources of entropy in turbomachines are: *viscous effects in boundary layers, viscous effects in mixing processes, shock waves and heat transfer across temperature differences.*

Regarding the boundary layer, most of the entropy is concentrated near the surface in the inner part of the layer, where the velocity changes are larger. More details about the formulation is given by [20] in function of Re_θ . In general, in range of Re_θ where the BL can be both laminar or turbulent, the entropy is larger in the turbulent case. On the other hand, the effect of the Mach number on this type of loss is generally considered to be small.

However, entropy generation due to viscous effects is not confined to boundary layers, but is associated with any shear rate within the flow field. Other regions with significant shear rates include turbulent regions, such as the edges of separation zones and wakes. Regarding the latter, [20] proposes a correlation for the total pressure loss coefficient:

$$\zeta = \frac{\Delta p^0}{\frac{1}{2} \rho_{TE} U_{TE}^2} = -\frac{c_{pb} t}{w} + \frac{2\theta}{w} + \left(\frac{\delta^* + t}{w} \right)^2 \quad (3.12)$$

Still, this model does not account for the detailed mixing process, including the unsteady nature of the Karman vortex street and the entropy generation due to viscous dissipation of vortices. w and t are respectively the throat opening and the TE thickness (see Section 3.1) while δ^* and θ are respectively the displacement thickness and the momentum thickness (see Section 2.3) at the TE. C_{pb} is called the *base pressure coefficient* and is a dimensionless parameter linked to the pressure in the base region p_b :

$$c_{pb} = \frac{p_b - p_{ref}}{\frac{1}{2} \rho_{ref} U_{ref}^2}. \quad (3.13)$$

The base region is the low pressure region just downstream the TE. Indeed, the first term of the Equation 3.12 refers to the wake losses linked to the low base pressure. On the other hand, the second term refers to the losses created by the mixing out of the BL; in fact, it is related to the momentum thickness of the BL at the trailing edge. Lastly, the third term refers to the mixing in the wake and usually it is smaller than the others.

If the BL separated before the TE, it could fail to reattach and an open separation occurs. In this case there is an extra loss to take into account:

$$\zeta_{sep} = \frac{\delta^{*2} + 2t\delta^*}{w^2}. \quad (3.14)$$

Therefore, a large open separation leads to high losses in the cascade.

Shock waves are also a source of entropy due to their inherent irreversibility. However, this phenomenon will not be discussed further as it is not observed in any of the simulations presented in this study.

Lastly, the entropy can be also generated by heat transfer. Usually, this phenomenon is negligible in turbomachines, except for cooled turbines. Since this study is not the case, this last source of entropy will not be discussed further as well.

3.5 Separation and transition

As discussed in the previous section, flow separation is one of the main threats to LPT performance. In low Reynolds number regimes, the flow has a tendency to remain laminar and thus to separate before it becomes turbulent. In this condition, the flow may not reattach, leading to large losses. As a consequence, it is important to understand the role of BL transition when dealing with LPT.

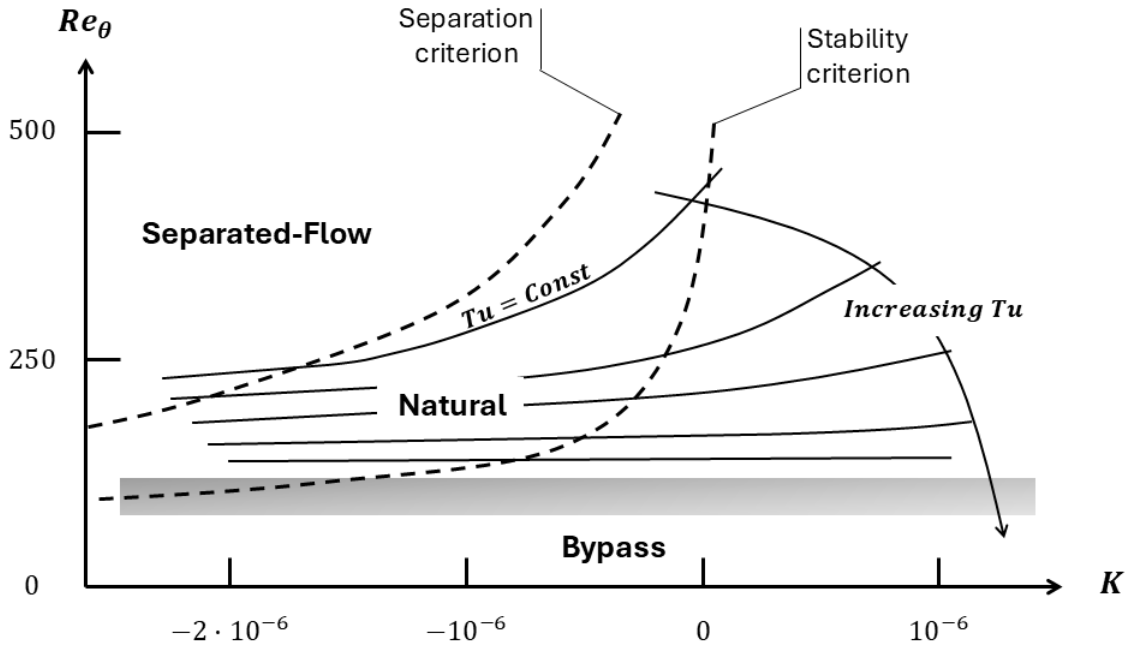


Figure 3.2: Different modes of boundary layer transition related to Tu , K and Re_θ (reproduced from [21])

Following the discussion of Mayle [21], the BL transition mode can be predicted using the turbulent intensity Tu , the acceleration parameter K (see Equation 2.54) and the momentum thickness Reynolds number $Re_\theta = (U\theta/\nu)$. Figure 3.2 shows

how these parameters are related to the different transition modes (these last are described in Subsection 2.3.1). The iso-Tu curves represent the Re_θ at which the transition begins, for a given Tu and K . The *stability criterion* curve represents the limit above which a Tollmien-Schlichting type of instability is possible, while the *separation criterion* curve represents the limit above which a laminar BL separates and a separated-flow transition is possible. According to Thwaites [22], the separation criterion is given by

$$Re_\theta^2 K = -0.082; \quad (3.15)$$

however, it does not consider the effect of Tu .

In the figure is not shown the *periodic-unsteady transition*, where the transition is triggered by the periodic passing of wakes or shock waves generated from the TEs of the upstream cascade. This type of transition is less known, also it can occur in multiple modes and on multiple locations of the same surface at the same time. Indeed, it is also known as *multimoded transition*.

Another transition type that is not shown in Figure 3.2 is the *reverse transition*, i.e. from turbulent to laminar. This phenomena can occur when Tu is low and $K > 3 \cdot 10^{-6}$ [21]. Flow regimes with high K can be encountered on LPT blades on the suction side (SS) near the LE and on the pressure side (PS) near the LE. Moreover, normal transition from laminar to turbulent cannot occur if $K > 3 \cdot 10^{-6}$.

The natural and bypass transitions modes have been already presented in Subsection 2.3.1, following the discussion of Schlichting and Gersten [17]. Regarding the separated-flow transition, further studies have been done by Hatman and Wang [23], which identifies three main separated-flow transition modes: *transitional separation mode*, *laminar separation/short bubble mode* and *laminar separation/long bubble mode* (see Figure 3.3).

There is a succession of intermediate stages between these modes that allows for a continuous process when passing from one mode to the other. In general, these types of transition take place with both Tollmien-Schlichting instability and Kelvin-Helmholtz (KH) instability. The former type has been described in Subsection 2.3.1, while the latter verifies with a separated BL and the low-speed flow near the wall.

Following the discussion of [23], the transitional separation mode is related to high Re flows and low adverse pressure gradients. In this case, the onset of transition x_t is upstream the separation point x_s . Between this two points, TS waves develop and evolves, while downstream x_s KH instability also sets in. For this mode, the maximum displacement location of the separation bubble x_{MD} coincides with the midtransition point $x_{u'max}$. Then, the increase in turbulent mixing leads to the reattachment of the BL in x_R . The end of transition and a fully turbulent BL take place in x_T , usually just downstream of x_R .

Regarding the laminar separation, for both short and long bubble modes, the onset on transition is induced downstream x_S by KS instability close to the maximum displacement point. The short bubble verifies in moderate Re flows with mild adverse pressure gradients, while the long bubble is typical encountered with low Re flows and strong adverse pressure gradients. In the first case, the pressure gradient is not strong enough and the high turbulent mixing in the region of $x_{u'max}$ leads to reattachment before the BL becomes fully turbulent. In the second case, the mixing

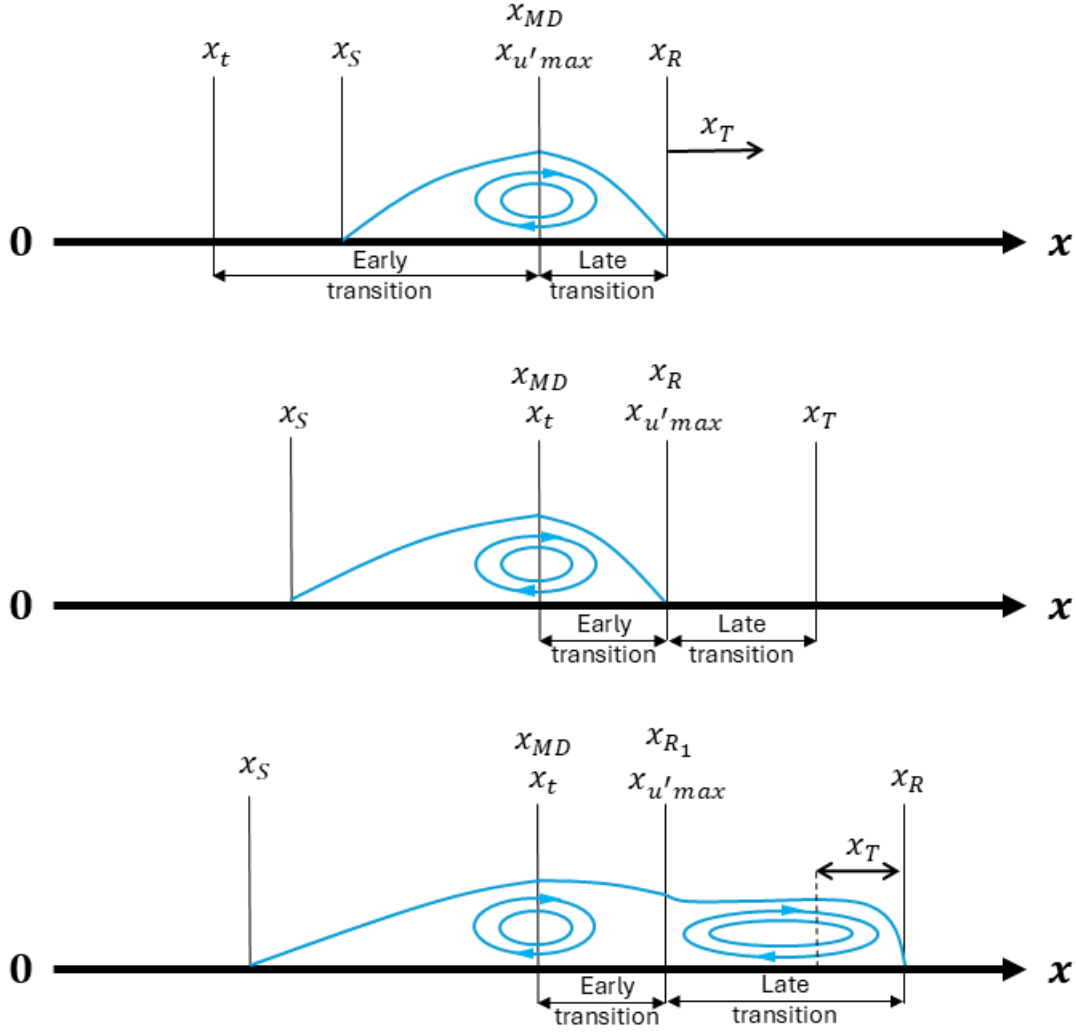


Figure 3.3: Time-averaged representation of different flow-separated transitional modes (reproduced from [23]): *transitional separation mode* (**top**), *laminar separation/short bubble mode* (**center**) and *laminar separation/long bubble mode* (**bottom**)

in $x_{u'max}$ leads to the first reattachment point X_{R1} . However the shear layer fails to remain attached and the short bubble *bursts* into a long bubble. Then the BL becomes fully turbulent and reattaches. Differently from short bubbles, which only have a local displacement effect, long bubble can heavily affect the pressure distribution along the blade (see [21]). Furthermore, if the adverse pressure gradient is strong enough or the Re is very low, the bubble may never close, causing large losses. Usually, in LPT cascades, the flow tends to separate on the PS near the LE, but it rapidly reattach due to favorable pressure gradient present downstream. Contrary to this behavior, in the SS the flow tends to separate near the TE, potentially causing a drastic drop in the performance of the cascade. Further investigation of the separation, transition and reattachment on the SS of blade in turbomachines has been done by Lou and Hourmouziadis [24].

Figure 3.4 shows the evolution of the loss coefficient ζ with Re for a LPT cascade.

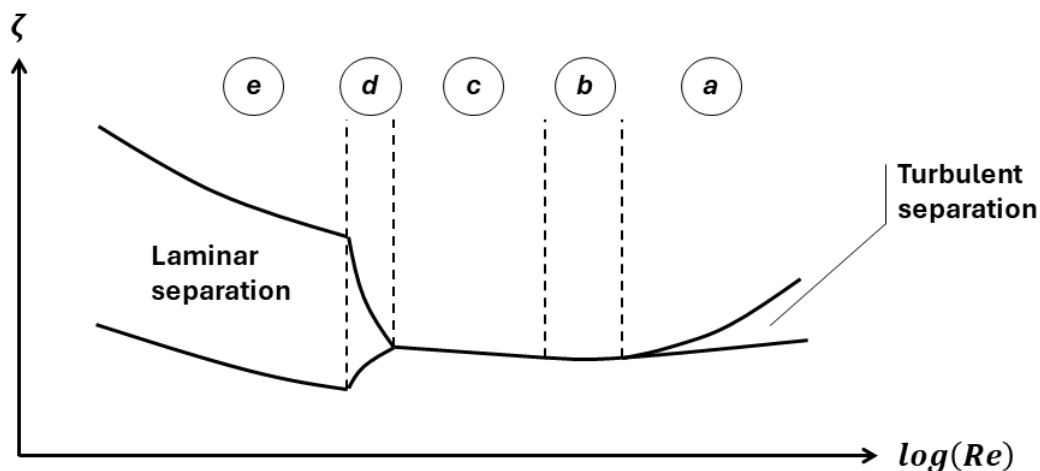


Figure 3.4: Qualitative effect of Re on the performance of a LPT cascade (reproduced from [24])

According to [24], when Re is high (a), a turbulent separation occurs near the TE, leading to mixing losses, in addition to wall shear stress losses. Decreasing Re , the turbulent separation disappears (b) and losses decrease as well. For even lower Re , the transition moves downstream and a laminar separation occurs on the SS (c). However, the turbulent shear layer reattaches before the TE. If the Re decreases further, the transition shifts further downstream and the turbulent shear layer cannot reattach (d), leading to a step increase of losses due to the mixing out of the separation in the wake. In this region, the transition point moves downstream as the Re decreases, until it reaches the TE plane (e). With lower Re , the loss grows due to increased thickness of the free shear layer.

Chapter 4

SPLEEN cascade experimental background

Within the SPLEEN project [25], the von Karman Institute for Fluid Dynamics (VKI) [26] has made a fundamental contribution in creating a unique experimental database in the context of high-speed low-pressure turbine cascades. This data provides a very important step for the development of new generation compact high-efficiency LPT. An open-access experimental database, containing data collected from 2018 to 2022 by the VKI and related to this context, can be consulted at [1]. The experimental campaign was conducted on the linear cascade codnamed SPLEEN C1, in the VKI high-speed wind tunnel S1/C. Measurements were taken under both on-design and off-design conditions, in order to observe and investigate in more depth the phenomena resulting from a wide range of operating conditions.

The following parts of this chapter contain a brief description of the VKI S1/C facility and a discussion of the physics behind the turbulence generation in the wind tunnel.

4.1 Experimental environment

The concepts presented in this section are entirely based on the work of Simonassi et al. [27, 28]. Readers are encouraged to consult these references for a more in-depth discussion.

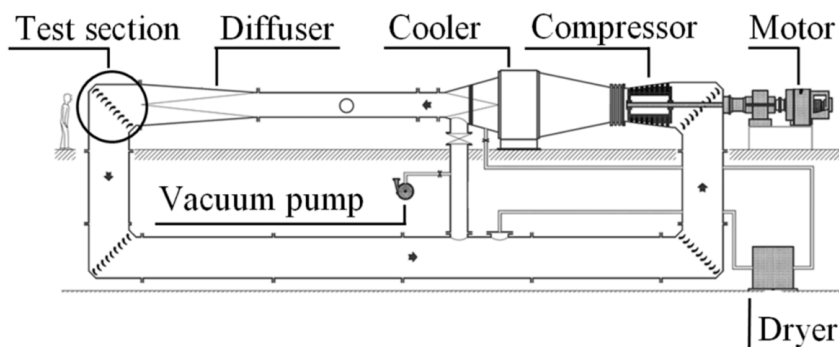


Figure 4.1: VKI S1/C wind tunnel (taken from [27])

Figure 4.1 shows a schematic of the VKI facility. The S1/C is a closed-loop

wind tunnel, where the flow is moved by a 615 kW, 13-stages axial flow compressor. The layout is specifically designed for linear turbine cascades testing. Indeed, the test section is located in the elbow of the tunnel, in order to easily handle the large deviation of the flow induced by the cascade. Moreover, the vacuum pump and the compressor rotation speed can be regulated independently, to change the Reynolds number and the Mach number respectively. Typically, the Reynolds number can be controlled in a range from 2×10^4 to 3×10^5 , while the range for the Mach number is from 0.6 to 1.2. This allows the simulation of a broad spectrum of operating conditions.

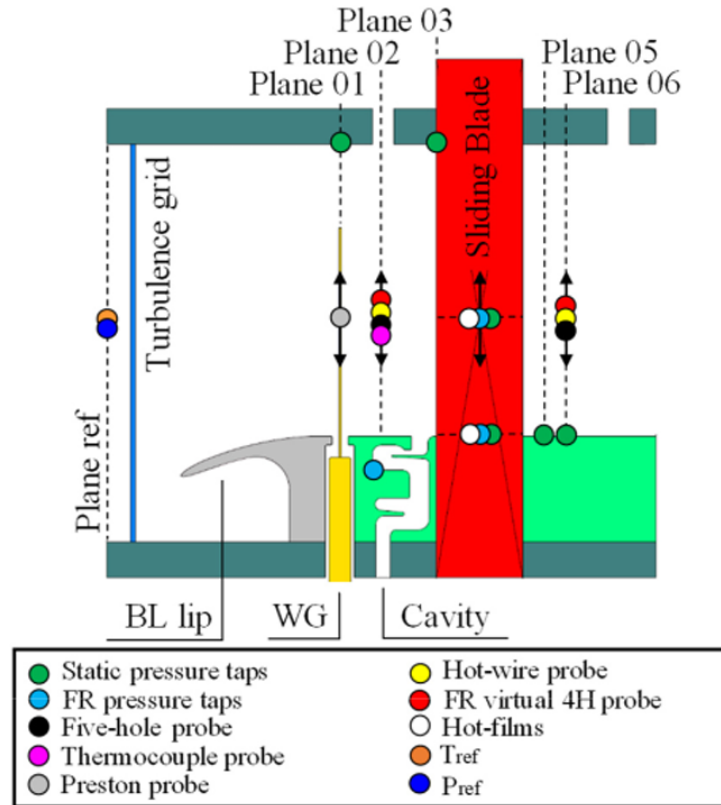


Figure 4.2: VKI S1/C wind tunnel (taken from [27])

Figure 4.2 shows the schematic planar view of the test section, including the measurement devices used. The linear cascade is composed by a total of 23 airfoils, which only the central blade is equipped with sensor. This central blade can slide along the spanwise direction, in order to measure a more complete distributions of quantities of interest. Other several devices can be notices from the schematic:

- a turbulence grid placed upstream of the cascade, designed to obtain a TI of around 2.5% at the blade (the back ground TI generated in the wind tunnel is of approximately 0.9%);
- a boundary layer lip, which prevents the boundary layer developed upstream to reach the cascade;
- a wake generator (WG) composed of 96 cylindrical rotating bars, which diameters and rotating speed are adjustable to simulate a desired situation of upstream turbine stage;

- a cavity just upstream the cascade, which can simulate a purge/leakge flow.

The last two elements are optional, allowing different flow setups. The configurations envisaged for the experimental campaign are:

- without both WG and cavity flow;
- with WG and without cavity flow;
- with both WG and cavity flow.

The results of the SPLEEN blade in this study refer to the first configuration.

4.2 Free-stream turbulence generation

When dealing with experimental simulations of a typical turbomachinery flow field, the generation of turbulence can be fundamental. One of the simplest ways of doing that in wind tunnels is using a grid placed normal to a uniform upstream flow. Following the discussion of Roach [29], this method leads to the generation of turbulence characterized by a fairly good homogeneity and isotropy. The device also causes a pressure drop, which is found to be directly proportional to the turbulence energy generated. Further considerations can be made about the flow just downstream the grid, which is strongly inhomogeneous, due to initially isolated bar wakes. These wakes grow in size and eventually coalesce, leading to a homogeneous flow ten mesh lengths downstream of the grid. Indeed, usually the experimental setups take this length into account. Moreover, examinations have shown that for grid solidity σ greater than 0.5, significant flow instability could occur. As a consequence, grids with $\sigma > 0.5$ are not recommended.

Several methods available from the literature try to determinate the characteristics of the turbulence downstream the grid. According to [29], the semi-empirical power law introduced by Frenkiel [30] gives a prediction of turbulence energy decay in good accordance with experimental evidence, without the necessity to estimate the grid pressure loss. The law is

$$Tu = C \left(\frac{x}{d} \right)^{-5/7}, \quad (4.1)$$

where Tu is the streamwise component of the TI, C is a function of grid geometry, x is the distance upstream of the grid and d is the representative grid dimension. [29] also introduced a semi-empirical power law to predict the evolution of the integral length scales. The expression for the evolution of the streamwise component of the integral scale is given by

$$\frac{\Lambda_x}{d} = I \left(\frac{x}{d} \right)^{1/2}, \quad (4.2)$$

where I is an empirical constant.

Regarding the VKI S1/C wind tunnel, the turbulence is generated through a $\sigma = 0.25$ grid, made up of thin cylindrical rods with $d = 3$ mm. In order to have a TI of approximately 2.5% on the cascade, the grid is placed 400 mm upstream to the LE of the blade. Using Equation 4.1 and Equation 4.2, and considering that for

Parameter	Unit	Predicted (blade LE)	Measured (plane 02)
Tu	[%]	2.43	2.34
Λ_x	[mm]	6.93	12.05

Table 4.1: Turbulence parameters predicted with semi-empirical law and measured experimentally with hot-wire probes

grid with parallel and round bars ($C = 0.8$ and $I = 0.2$), is possible to predict both Tu and Λ_x .

Table 4.1 shows the value predicted for Tu and Λ_x with the semi-empirical laws and also the same parameters measured with hot-wire probes at plane 02 of the S1/C. Plane 02 is just upstream the LE of the blade, so is reasonable to think that the Tu on the LE of the blade is slightly lower than the measured value, while the Λ_x is slightly higher. Although the difference between experiment and prediction, the TI magnitude is still satisfying. For Λ_x , the discrepancy between the two cases is more pronounced. However, it is important to note that both the semi-empirical law and the experimental measurements rely on a number of assumptions. Therefore, the observed difference may not be entirely unexpected.

The turbulence injection for all the numerical simulations presented in this study employs the fluctuations generated and utilized by Deneffe [7], which aimed to replicate the experimental turbulence intensity level at the LE of the blade, using the value reported in Table 4.1 (see Chapter 6).

Chapter 5

Numerical methods and tools

This chapter will briefly discuss the numerical and computational tools used to obtain the results presented in this master's thesis.

It is possible to predict fluid flows using computing resources, through Computational Fluid Dynamics. CFD simulations are a powerful tool for fluid dynamics analysis. Compared to experiments, CFD simulations offer the advantage of being able to simulate and analyze flow properties in situations that would be impossible or very difficult to replicate experimentally. Additionally, CFD simulations avoid the disturbances that physical probes can introduce into the flow.

To solve a fluid flow through the CFD it is necessary to discretize the Navier Stokes Equations (NSE), which can be done in many ways, with the most common being Reynolds-Averaged Navier-Stokes (RANS), Large Eddy Simulation (LES), and Direct Numerical Simulation (DNS). RANS models the effects of turbulence by solving averaged equations, while LES resolves the large turbulent structures and models the smaller scales. DNS, on the other hand, resolves all turbulent scales (see Figure 5.1). Moving from RANS to DNS, there is a decrease in the amount of modeling required, but an increase in computational cost, which scales with the Reynolds number. Since the size of the smallest turbulent eddies (Kolmogorov scale) is inversely proportional to $Re^{3/4}$ (see Subsection 2.2.2), the computational cost of a DNS simulation increases with the Reynolds. More precisely, the computational cost is estimated to be proportional to Re^3 for homogeneous turbulence and even more for inhomogeneous cases [31].

In this master's thesis, a DNS approach is employed, which allows the resolution of all turbulent scales and leads to greater accuracy. While the simulations pertaining to the free domain may be considered DNS, those concerning the turbine cascade do not strictly adhere to the DNS criteria. This deviation stems from the prohibitive computational cost associated with achieving the requisite wall resolution for a true DNS in such complex geometries. Nonetheless, the term is retained herein due to the high resolution employed, which captures a significant portion of the turbulent scales. To address the high computational cost associated with DNS, high-performance computing resources are used. Thanks to technological advancements, supercomputers are becoming increasingly powerful, capable of solving complex problems. To further manage computational costs, the computational domain is divided into multiple partitions that are solved in parallel, with each partition assigned to one or more computational cores (CPUs).

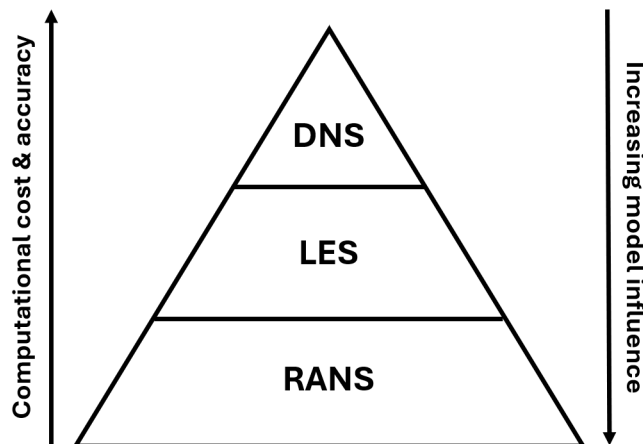


Figure 5.1: A visual comparison of the fundamental properties of different CFD methods

The simulations presented in this master's thesis were performed on NIC5 and Lucia supercomputers, which will be discussed in detail later in this chapter. NIC5 was employed to solve the free domain simulations, while Lucia was employed for the turbine ones. In both cases, the solver used is ArgoDG. The latter implements the Discontinuous Galerkin Method, which among its various features has the advantage of facilitating parallelization due to its discontinuous nature. The main features of the numerical method and the numerical solver will also be presented in the following sections.

5.1 HPC

NIC5 and Lucia supercomputers are high-performance computing (HPC) clusters, the first one is hosted at the University of Liège in Belgium while the second one is managed by a private non-profit applied research center called *Cenaero* [32]. They are part of the CÉCI (*Consortium des Équipements de Calcul Intensif*) infrastructure [33], that was born in November 9th 2010, by the signature of the Rectors of five French-speaking universities in Belgium, and now provides computational resources to researchers across the country, thanks to the support of the *Fond national de la recherche scientifique* (FNRS) and the Walloon Region. The computational resources involved are 6 clusters and, except for Lucia [34], five of them are hosted by different Belgian universities (like NIC5).

5.1.1 NIC5

NIC5 consists of 4672 cores spread across 73 compute nodes with two 32 cores AMD Epyc Rome 7542 CPUs at 2.9 GHz. The default partition holds 70 of 73 nodes, with 256 GB of RAM each and thus 3.9 GB per core. However, there are also 3 nodes with 1 TB of RAM for memory-intensive tasks. All the nodes are interconnected using a high-speed network (100 Gbps Infiniband HDR), crucial for parallel computations. NIC5 is also backed by a high-performance parallel file system, providing fast access to large datasets of 520 TB.

Furthermore, the scheduling of jobs on NIC5 is managed by a Slurm Workload Manager. In order to queue and run the jobs, it is necessary to write a submission script describing the needed resources and the desired operations. For instance, it contains the computational time, the number of tasks, the number of CPUs per task and the memory per CPU. During this study, regarding the simulations run on NIC5, were used 64 tasks per simulation (one per partition), with one CPU per task and a memory per CPU that was chosen according to the specific case.

5.1.2 Lucia

Lucia comprises three distinct partitions: a 300-node CPU partition, a 50-node GPU partition, and a 14-node heterogeneous partition for specialized workloads. Regarding the CPU partition, each node is equipped with two 64-core AMD EPYC 7763 processors operating at 2.45 GHz, while for the GPU partition, each node features two 32-core AMD EPYC 7513 processors running at 2.6 GHz and four NVIDIA A100 40GB GPUs. Both CPU and GPU nodes boast 256GB of RAM. Of the other 14 nodes, 7 are large memory nodes, 1 is extra-large memory, 2 are for AI workflows and 4 are for visualization. All partitions are integrated through an HDR InfiniBand network and a 10Gb/s Ethernet network, ensuring high-speed communication between nodes and resources. With a combined peak performance of approximately 4 PetaFLOPS, Lucia was ranked 245th on the November 2022 Top500 List. Lucia leverages the IBM Spectrum Scale file system (formerly GPFS) for storage, providing a robust and scalable solution. The system includes 2.87 PB of standard disk space, further divided into 200TB for user home directories, 1.5PB for project data, and 1PB for temporary scratch space. A robust backup system based on IBM Spectrum Protect safeguards user data in the home and project directories.

Similar to NIC5, the scheduling of jobs on Lucia is managed by a Slurm Workload, with the difference that the nodes on Lucia cannot be shared with different jobs and the number of nodes desired for each job has to be specified in the slurm file. During this study, simulations run on Lucia have requested 16 nodes, and were used 512 tasks (one per partition) with 4 CPUs per task.

5.2 DGM

Among the various methods developed to approximate the solutions of systems of partial differential equations, two are the most well-known: the finite element method (FEM) and the finite volume method (FVM). In both methods, the computational domain is split in small parts, called control volumes in FVM and elements in FEM. In each part a discrete set of variables is computed through a corresponding number of equation properly defined, and then used for the interpolation of the approximated solution. The precision of this solution depends on the elements size (i.e., the resolution of the mesh), and on the order of convergence (i.e., the evolution of the error with the typical mesh size). The FEM is based on piecewise polynomial approximations and is primarily applied to elliptic and parabolic (i.e., diffusive) problems. This method is particularly well-suited for cases where the solution is sufficiently regular. On the other hand, in the case of solutions with strong gradients or discontinuities, such as compressible flows, the approximation made by

FEM methods typically suffers from the Gibbs phenomenon, that consists of non-physical oscillations called spurious oscillations. Although stabilization techniques exist, the difficulties in applying them to the solution of compressible flows commonly lead to the resolution of these flows using FVM. This second type of method typically involves a piecewise constant approximation, with communication between elements through fluxes. Since the reconstruction of the solution is discontinuous at the interface between elements, FVM allows for easier management of solution discontinuities, such as shock waves. In fact, these methods are the most used in the case of convective or hyperbolic problems. The main drawback of these schemes is that they usually have a low-order of accuracy, and the construction of a high-order FVM is conditioned by the presence of various obstacles.

With the aim of combining the advantages of the previous two methods, the Discontinuous Galerkin Method is introduced [35]. This method allows high-order accurate scheme through the approximation of the solution obtained using piecewise polynomial functions over a finite element mesh without any requirement on interelement continuity (see Figure 5.2). The use of high-order polynomials to approximate the solution, together with the discontinuous nature of this approximation, allows for an excellent combination of accuracy and flexibility of the method. Since DGM allows for communication between elements through fluxes as in FVM, the management of the convective contributions of the solution over time can be easily handled through upwind flux techniques. The same cannot be said for diffusive contributions, for which stabilization techniques are necessary. The solver ArgoDG uses the symmetric interior penalty discontinuous Galerkin (SIPDG) method by default, which consists in evaluating the jumps between elements (called penalties) aiming to the best-fitted solution with the smallest penalties possible, in order to avoid too large discontinuities at the interfaces between elements.

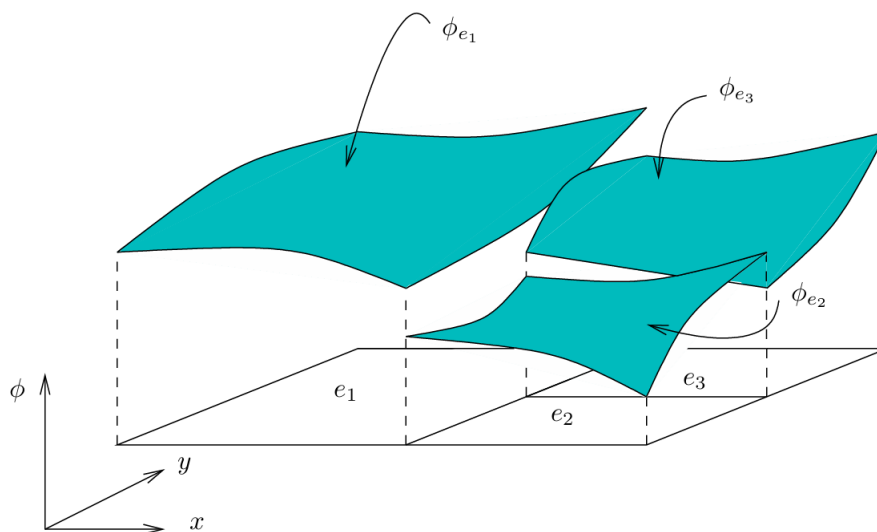


Figure 5.2: Example of the discontinuous trial space of the DGM (taken from [36])

5.3 ArgoDG

ArgoDG is a three-dimensional solver developed at *Cenaero* (see [36] and [37]). In the past years, it has been employed in several European programs, such as ADIGMA, IDIHOM, Tilda and HiFiTurb. The simulation is controlled through an input file where all simulation parameters are specified, such as the computational mesh, boundary conditions, fluid properties, initial conditions, reference frame, non-linear solver, order of accuracy, stabilization method, Jacobian matrix computation method, and many others. In this work, the meshes were generated using the software GMSH, which produces files that Argo can read and, if applicable, can assign periodic boundary conditions defined during mesh generation.

Furthermore, the desired output must also be defined in the input file. For example, it is possible to save specific solution parameters extracted from regions of interest within the domain, such as the entire domain, interfaces, or specific points and sections. Values can be extracted for a specific point and instant or averaged over time and/or space. The generated output files can be in the form of numerical data sets for easy post-processing, or they can be used to visualize the fluid flow field through ParaView for example.

Chapter 6

Turbulence injection

This chapter introduces the concept of turbulence injection, which involves the creation and utilization of flow data necessary for the numerical simulation of turbulent inflow conditions. The various methods employed for turbulence injection will be reviewed, highlighting their strengths and weaknesses. Subsequently, the specific method adopted in this study will be detailed, including a description of the simulation used to generate turbulent fluctuations and the criteria used to process these data for application to the main flow simulation.

6.1 Review of existing turbulence injection methods

Generating turbulent inflow demands a time series that encompasses all the length and time scales resolved by the simulation at the inlet boundary. This section reviews existing methods for generating such turbulent inflow conditions in numerical simulations. Following the discussion of Hao et al. [38], these methods can be categorized into four groups:

1. transition-inducting methods;
2. turbulence library-based methods;
3. recycling-rescaling methods;
4. synthetic inflow generators.

It is also possible to identify a recent type of method based on machine learning and deep learning techniques.

6.1.1 Transition-inducting methods

Differently from other types of method, this one does not aim to generate fully developed turbulence, but aims to trigger the transition from laminar to turbulent flow in the numerical simulation. These methods are based on the introduction of controlled disturbance in the flow, e.g. acoustic waves or localized perturbations, in order to mimic the natural mechanism of transition.

Although the implementation of this family of methods is relatively straightforward, the range of applicability is limited. They also typically require a large space

to achieve fully developed turbulence. In addition, the injection of disturbance can lead to spurious effects if not well controlled, and acoustic effects that are not always of interest.

6.1.2 Turbulence library-based methods

In this type of methods, a realistic turbulent flow is extracted from a database of snapshots or an auxiliary simulation, and then injected in the main simulation. In these cases, the injected flow is already describing a physical solution, therefore a "high-quality" turbulent flow field can be obtained with minor approximations (e.g., Taylor's hypothesis). Furthermore, the auxiliary simulation parameters can be set in order to have a specific length scale and TI.

Nevertheless, if the injection data are not already available, the generation of the database or the use of an auxiliary simulation is associated with a high computational cost, especially if the Reynolds number is large. Also, the need to storage the data must be taken into account, as well as the need to read and process them in a way that does not affect the global performance of the simulation. Lastly, a temporal correlation can be observed because of the finite length of the database.

The turbulence injection method used in this study belongs to the family of methods just discussed. Specifically, the injection data was generated using an auxiliary simulation (precursor method). More details about the latter are discussed in Section 6.2.

6.1.3 Recycling-rescaling methods

In these methods, the flow information related to a downstream position in the main domain is recycled as inflow condition for the same domain. In other words, the flow imposed at the inlet is extracted from a downstream location. This continuous process leads to an asymptotic configuration in which the turbulence is fully developed. The main advantage over library-based methods is the feedback of the inflow from the main domain itself. Following the discussion of Wu [39], the recycling methods can be classified into two further types:

- strong recycling methods;
- weak recycling methods,

In the first sub-category, the strict periodic condition is applied between the downstream and the upstream positions. In the second type, the extracted data are rescaled, in order to satisfy the desired statistics of the flow at the inlet. Rescaling is necessary, for example, when dealing with a spatially developing boundary layer [40, 41, 42].

In general, an important drawback of these methods is their limited range of applicability to simple configurations. Furthermore, due to the finite distance between the extraction position and the inlet, this type of methods imposes a strong spatial correlation.

6.1.4 Synthetic inflow generators

Following the discussion of Dhamankar et al. [43], this type of methods aims to reconstruct a turbulent velocity field, using analytical expression or statistical techniques. These methods can be potentially used in a wide range of turbulent flow conditions and the turbulence can be generated in order to have specific properties (i.e., length scale, TI, Reynolds stress tensor...). Furthermore, differently from library-based methods, the computational cost and the need of storage capability associated to an auxiliary simulation is avoided. An ideal synthetic method should be able to generate a realistic turbulent flow for every situation. However, the resulting turbulence does not solve the NSE at the inlet and thus is not perfectly realistic, even though it fulfills a series of statistics. This type of methods requires a certain development distance, called *development fetch* [44, 45]. Usually, the first-order statistics are met immediately, while the higher-order statistics are met further downstream. The need for this development fetch is handled by an extension of the domain, which leads to an increase in the computational cost of the simulation. Consequently, the distance of adaptation is a good indicator of the performance of a synthetic method. An example of a synthetic method with favorable results is the turbulent inflow data generator based on a digital filter developed by Klein et al. [46].

Several methods belonging to this category exist, and a brief review can be found in [38, 43].

6.1.5 Machine learning and deep learning techniques

The methods using these techniques have been developed recently, with the aim to take advantage of the increasing power of artificial intelligence to generate high-fidelity turbulence. These methods are trained with large experimental or numerical databases of turbulent flows, in order to predict new artificial flow fields and potentially generate realistic turbulent inflow conditions.

An example of method belonging to this family has been developed by Fukami et al. [47], which used a neural network to generate time-dependent turbulent inflow data, in the case of a channel flow. Another method has been developed by Kim and Lee [48] on a similar test case, which has been able to reproduce flow fields at various Reynolds numbers.

6.2 Turbulence injection procedure

The turbulent inflow data that have been used for this study have been generated by Deneffe [7], who followed the procedure presented by Rasquin et al. [49]. The procedure consist in using a precursor simulation to realize a turbulent free-stream flow with zero mean velocity and then combine the resulting velocity fluctuations u' with the inlet mean flow \bar{U}_{in} of the main simulation. In the specific case of this study, also the static pressure fluctuations p' and the temperature fluctuations T' have been used. This turbulence injection method falls into the turbulence library-based methods (see Subsection 6.1.2). The method can be performed under two main hypotheses:

- Taylor's hypothesis (see Subsection 2.2.3), and

- spatially homogeneity of the flow field (even in the flow direction).

With the first hypothesis, the non-linear interaction between the mean inlet flow and the velocity fluctuation can be neglected, so that the resulting turbulent injected velocity field is $\bar{U}_{in} + u'$.

The following subsections will briefly discuss about the features of the precursor simulation and the final realization of the turbulent inflow data. More details can be found in [7].

6.2.1 Setup and execution of the precursor simulation

The precursor simulation employed in this study is the canonical case of homogeneous isotropic turbulence decay, simulated in a triply periodic cubic domain [9], with a characteristic length of $L = 4.11875$ mm (Figure 6.1). The precursor domain mesh, generated using GMSH, consists of 16 elements in each direction. This element number was chosen as a trade off between computational cost of the precursor simulation and the resolution required to simulate the DHIT.

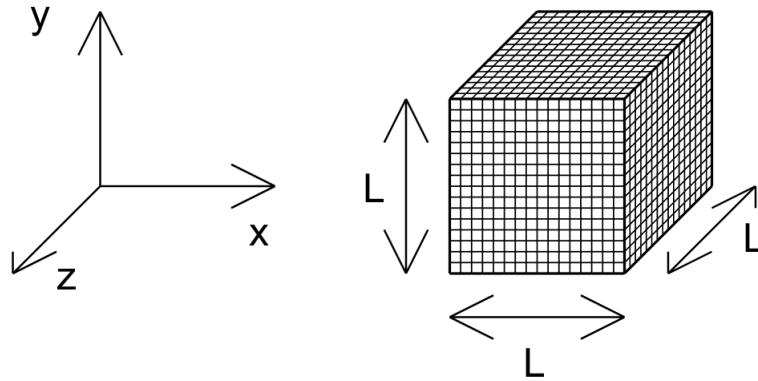


Figure 6.1: Precursor domain mesh, 3-dimensional view

The precursor simulation was performed using the DGM solver implemented on ArgoDG, with a polynomial spatial discretization of order $p = 3$. Assuming incompressible turbulent fluctuations at the inlet of the main simulation, the initial conditions involved imposing an incompressible velocity field with zero mean in the cube, following the methodology outlined by Rogallo [50]. The energy spectrum of the field was given by Passot and Pouquet [51]. By considering the dimensions of the precursor domain and adjusting the amplitude and spectral width of this spectrum, specific initial turbulent kinetic energy and integral length scales could be obtained. Additional initial conditions included uniform total temperature and total pressure, consistent with the inlet conditions of the main simulation. Further details regarding the precursor simulation setup can be found in [7].

The evolution of TKE within the precursor simulation is monitored to determine the optimal time at which to extract the turbulent fluctuations. The goal is to replicate the experimental conditions reported in Chapter 4, specifically the $Tu = 2.34\%$ at a distance $0.5 \times c_{ax}$ upstream of the LE of the blade (Table 4.1). However, due to the significant discrepancy between the experimentally measured integral length

scale and that obtainable from the precursor simulation (approximately 1 mm), a different turbulent decay is expected. Specifically, a more rapid decay is anticipated in the numerical simulation compared to the experimental data. Consequently, the target value of Tu equal to 2.2% is set on the LE fo the blade, based on the measured value at plane 02 (2.34%).

Given the Tu_{target} , it is possible to estimate the $Tu_{extraction}$ using the DHIT monitored from the precursor simulation. Knowing t_{target} (which is the temporal instant corresponding to Tu_{target}), it is possible to calculate $t_{extraction}$, estimating the time it takes the turbulent fluctuations to reach the blade from the inlet. The temporal delay between $t_{extraction}$ and t_{target} was calculated knowing the distance of the blade from the inlet ($0.75 \times c_{ax}$) and the streamwise component of the mean velocity at the inlet. The resulting value is $\Delta t = 3.0759 \cdot 10^{-4}$ s, therefore $Tu_{extraction} = 5.214\%$. More details about the estimation of $Tu_{extraction}$ can be found in [7].

6.2.2 Duplication, transformation, concatenation and blending of the precursor solution field

The idea is to inject turbulence into the main domain continuously, using the fluctuations extracted from a much smaller precursor domain. Due to the limited size of the triply periodic cube, a solution could be to use several copies of the turbulent field. Using the same flow field in this way would have a very high correlation in the streamwise direction, which is considered as much more detrimental than in the pitchwise and spanwise directions. To overcome this problem, a procedure inspired by Xiong et al. [52] and Larsson [53] has been adopted. This procedure consists in using a concatenation along the streamwise direction of different pseudo-realizations of the precursor domain, obtained through translations and rotations on the original cube. To avoid discontinuities at the interfaces between the pseudo-realizations, the concatenation is implemented by a blending technique. In this way a smooth turbulent flow field is obtained along the streamwise direction. Lastly, to solve some undesired compressibility artifacts typically introduced by the blending, a projection of the velocity field on a divergence-free space is performed.

The blended turbulence box generated by [7] and used in this study, is obtained by merging 24 pseudo-realizations of the initially extracted flow field, with a blending length of nearly 20% of the total size of the box. The resulting domain retains periodicity in all the direction.

Chapter 7

Free domain simulations

This chapter focuses on the effect of various simulation parameters on the properties of freely decaying turbulence. The parametric study in question was conducted through a series of simulations performed in a free domain. Firstly, the details regarding the numerical simulation setup will be presented. Secondly, the results of the various cases will be compared and discussed, in order to evaluate the impact of the simulation parameters.

7.1 Computational setup

The parametric study was conducted through several simulations, each with different characteristics. Initially, a baseline simulation was established, i.e. the *baseline case*. Subsequently, the effects of various parameters were investigated:

- Reynolds number and Mach number;
- injection angle (α_{in});
- type of boundary conditions imposed at the inlet (total or static);
- type of mesh (isotropic or anisotropic).

Table 7.1 summarizes the characteristics of the baseline case, where the Mach number and Reynolds number refer to the inlet section of the domain, and the characteristic length for the Reynolds number is the length of the precursor domain used for turbulence generation $Re = (LU_{in})/\nu_{in}$.

Re	M	α_{in}	BC type	Mesh type
$4.584 \cdot 10^3$	0.4222	0°	Total	Isotropic

Table 7.1: Characteristics of the baseline case

To study the effects of Reynolds and Mach numbers, two different values were considered for each quantity (see Table 7.2).

These values were combined to create four different flow configurations: Re_1M_1 , Re_1M_2 , Re_2M_1 , and Re_2M_2 . In this first part of the parametric study, these four cases were analyzed with the Re_1M_1 case serving as the baseline, while other parameters were kept constant. For the second part, Reynolds and Mach numbers

Re_1	Re_2	M_1	M_2
$4.584 \cdot 10^3$	$7.825 \cdot 10^3$	0.4222	0.6

Table 7.2: Re and M values for the parametric study

were fixed to the baseline values, while other parameters were varied individually and in combination. A summary of all cases analyzed is presented in Table 7.3.

Re and M	α_{in}	BC type	Mesh Type
Re_1M_1	0°	Total	Isotropic
Re_1M_2			
Re_2M_1			
Re_2M_2			
Re_1M_1	26.565°	Static	Anisotropic
	63.435°		
	0°	Total	
	26.565°		
	63.435°	Static	
	0°		
	26.565°		
	63.435°		

Table 7.3: Summary of the parametric study

The following parts of this section will discuss with more details several aspects of the free domain simulations. Firstly, the computational domain and the relative meshing are introduced. Secondly, the parameters of the numerical solver settings and the physical hypothesis are listed and explained. Third, the boundary conditions and their effect on the flow are discussed. Subsequently, the numerical transient of the simulations is highlighted, considering the initial conditions of the solution and the convergence criteria. Lastly, the virtual probes and monitors used to extract the data and the parameters of interest are defined.

7.1.1 Computational domain and meshing

To investigate the spatial evolution of turbulent flow, a free computational domain was adopted, specifically a virtual wind tunnel in the shape of a parallelepiped. This geometry is a simple choice to analyze the evolution of turbulent flow without the effect of any wall. Due to the high number of cases analyzed, the tunnel is simple and relatively small, in order to reduce the total computational cost.

The dimensions of the domain were determined based on the dimensions of the cubic precursor domain presented in [7], with an edge length $L = 4.11875$ mm. The parallelepiped extends for a length L in the y and z directions, while the streamwise length (corresponding to the x -direction) is $12 \times L$. This configuration can be visualized as a sequence of 12 cubes with side length L , aligned along the streamwise

direction (Figure 7.1).

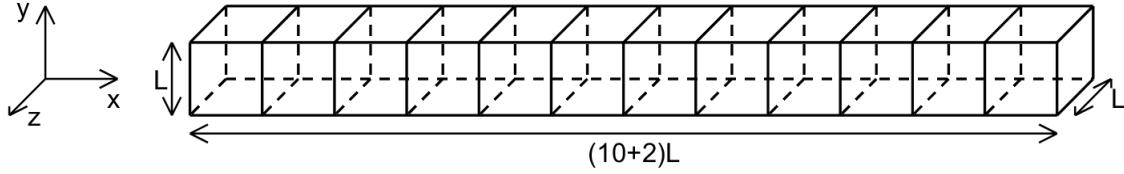


Figure 7.1: Free domain, 3-dimensional view

The first 10 cubes constitute the primary region of interest, where analyses were conducted to assess the evolution of flow parameters as a function of the streamwise location. The last two cubes were dedicated to the implementation of a sponge layer. This is a wave-damping region of the domain and its function is to gradually attenuate numerical perturbations propagating towards the domain boundaries, thus avoiding wave reflection and ensuring open boundary conditions. In other words, the sponge layer absorbs the turbulence energy, simulating an infinite environment.

The mesh was generated using the open-source software GMSH (see Section 5.3). In order to analyze the effect of spatial discretization on turbulent flow evolution, two different meshes were used in this study: an isotropic mesh and an anisotropic one. For the first mesh, the free domain was discretized similarly to the precursor domain in [7] (Figure 6.1): each edge of length L was divided into 16 elements, while the long side was subdivided into $12 \cdot 16 = 192$ elements. This resulted in a structured, isotropic, three-dimensional mesh composed of 49152 identical cubic elements, with an edge length of $L/16 = 0.25742$ mm each (Figure 7.2). The main domain is discretized using the same spatial resolution as the precursor domain to optimize computational resources. Employing a coarser mesh in the main domain would compromise its ability to resolve the smallest turbulent structures. Conversely, using a finer mesh would result in over-resolution, as the main domain would be resolving structures generated in a coarser mesh. More details about the precursor domain and the turbulence injection are discussed in Chapter 6.

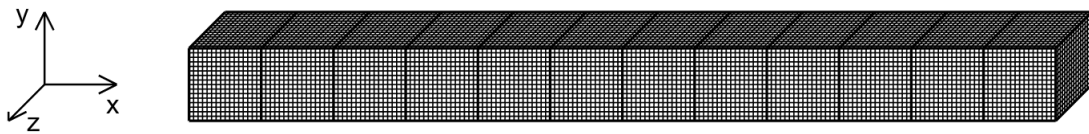


Figure 7.2: Free domain isotropic mesh, 3-dimensional view

Subsequently, the mesh was split into 64 partitions, resulting in 768 elements per partition. The choice of the number of partitions and the number of CPUs dedicated to each partition (1 CPU per partition) is based on a trade-off between simulation efficiency and the utilization of the HPC resources available (see Section 5.1.1).

For the anisotropic mesh, the elements size along the z -direction is halved (Figure 7.3). The resulting mesh exhibits a resolution comparable to the inlet region of the turbine domain, where the streamwise and pitchwise resolutions are consistent with the precursor domain, while the spanwise resolution is enhanced (see Subsection 8.1.1). Despite the doubled number of elements compared to the isotropic mesh,

the simulation characteristics in terms of partitions and CPUs per partition were kept unchanged, but the memory per CPU was appropriately increased.

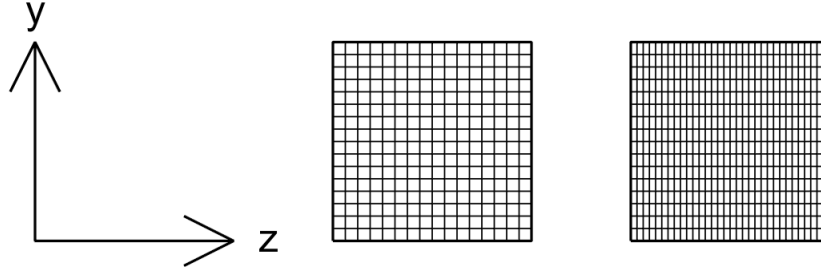


Figure 7.3: Isotropic mesh (**left**) and anisotropic mesh (**right**), 2-dimensional inlet view

7.1.2 Solver settings

As discussed in Chapter 5, the flow equations are solved using the ArgoDG software. The compressible NSE are considered, including continuity, momentum, and energy equations. Furthermore, the governing equations are dimensionless using reference values for pressure ($p_{ref} = 6000$ Pa) and temperature ($T_{ref} = 260$ K). The numerical solver uses the conserved variables (ρ , ρu , ρv , ρw , ρE) as degrees of freedom. More details about fluid equations, assumptions, and constants are discussed in Section 2.1. A DGM with a polynomial order $p = 3$ is employed for spatial discretization. This choice is consistent with the discretization used in the precursor domain, as detailed in [7]. The Roe upwind flux for the convective terms is used, while, to stabilize the diffusive fluxes, the DGM is coupled with the SIPDG method, as discussed in Section 5.2.

Regarding the temporal discretization, a second-order backward difference (BDF2) scheme is employed. A nonlinear tolerance of 10^{-4} is set for the time integration. The nonlinear solver utilizes a Newton method, extended with a Generalized Minimal Residual Method (GMRES) iterative solver. To accelerate convergence, a Jacobi preconditioner is applied to the Jacobian matrix. Given the relatively slow variation of the Jacobian matrix over time, it is recomputed only every 5 time steps to improve computational efficiency. This approximation is justified by the fact that the Jacobian matrix size is directly proportional to the number of degrees of freedom (DOF) of the problem, and therefore, freezing it for several time steps can significantly enhance the simulation performance. The time step size is determined adaptively to satisfy the CFL condition. Typically, time steps in the range of 10^{-7} s to 10^{-6} s are used.

7.1.3 Boundary and initial conditions

To generate the flow for different test cases, different boundary conditions were used. In all simulations, periodic conditions were applied on boundary faces in both the y and z directions, respectively. At the inlet, either *Mach total* and *Free stream* boundary conditions type were imposed, depending on the specific case. The first condition type specifies total variables, while the second one specifies static variables. Static pressure boundary condition was imposed at the outlet in all simulations, with

the pressure value adjusted for each test case to ensure a statistically homogeneous solution throughout the domain.

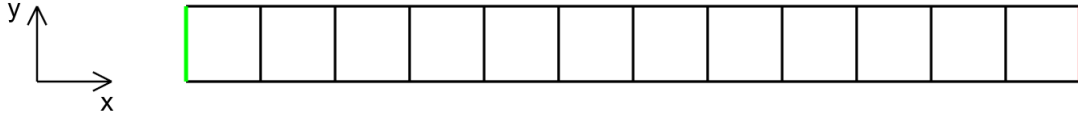


Figure 7.4: Free domain with inlet shown in green (left) and outlet shown in red (right), 2-dimensional view

For the parametric study on the effects of Reynolds and Mach numbers, the same inlet boundary conditions as in the baseline case were employed, i.e., Mach total conditions. Total variables were used at the inlet of the baseline case because usually it is the standard way to impose boundary conditions in turbine CFD simulations. Table 7.4 details the inlet and outlet conditions for the various cases with different Re and M . The case Re_1M_1 corresponds to the baseline case.

Quantity	Unit	Re_1M_1	Re_1M_2	Re_2M_1	Re_2M_2
P_{in}^0	[Pa]	$1.0779 \cdot 10^4$	$0.8190 \cdot 10^4$	$1.0779 \cdot 10^4$	$0.8165 \cdot 10^4$
T_{in}^0	[K]	300	300	200	200
P_{out}	[Pa]	$9.5353 \cdot 10^3$	$6.4209 \cdot 10^3$	$9.5353 \cdot 10^3$	$6.4014 \cdot 10^3$
α_{in}	[°]	0			

Table 7.4: Boundary conditions for simulations with different Re and M

To analyze the effect of the injection angle, the Reynolds and Mach numbers were kept constant at the baseline case values (Re_1M_1), while the parameter α_{in} was varied (see Table 7.5).

Quantity	Unit	Case ₁	Case ₂	Case ₃
α_{in}	[°]	0	26.565	63.435

Table 7.5: Boundary conditions for simulations with different α

In the same way, Free stream boundary condition cases were simulated with $Re = Re_1$ and $M = M_1$. As an example, Table 7.6 presents the values used to reproduce the $\alpha_{in} = 0$ case. To change the injection angle, the inlet velocity \bar{U}_{in} is modified in order to maintain the same magnitude and to obtain injection angles as those in Table 7.5.

In all the cases, turbulence is introduced into the domain through the inlet. However, for Mach total conditions, it is sufficient to specify the velocity field from the precursor simulation, while for Free stream conditions, the static temperature and static pressure fields must also be specified from precursor simulation.

To accelerate convergence, the flow field was initialized with a homogeneous solution throughout the domain, consistent with the inlet boundary condition. The specific properties of the initial solution varied depending on the type of inlet boundary condition (Figure 7.7).

Quantity	Unit	Example case
P_{in}	[Pa]	$9.5353 \cdot 10^3$
T_{in}	[K]	289.6703
\bar{U}_{in}	[m/s]	[144.0567 0.0 0.0]
P_{out}	[Pa]	$9.5353 \cdot 10^3$

Table 7.6: Example case with Free stream boundary conditions

Mach total cases		Free stream cases	
Quantity	Unit	Quantity	Unit
P^0	[Pa]	P	[Pa]
T^0	[K]	T	[K]
M	[-]	\bar{U}_{in}	[m/s]
α	[°]		

Table 7.7: Types of initial solution

7.1.4 Convergence

Most of the data presented in this master's thesis are time and space averaged characteristics of turbulent flows, therefore data collection can start only after the numerical transient of the simulation is finished and the domain is converged to a statistically steady state.

To assess the end of the transient, the convective density flux at the inlet and outlet is monitored. For a steady-state problem, it is sufficient to use the principle of mass conservation by monitoring the mass flow rate through the domain boundaries. However, since the flow in the cases considered is turbulent and thus intrinsically unsteady, mass conservation is not verified instantaneously. Nevertheless, it is possible to evaluate the statistical steadiness by assessing when the mass flow rate average over time is zero.

Figure 7.5 and Figure 7.6 show the convective density flux at the inlet and outlet and their difference, respectively for the numerical transient and for the converged simulation. These data are extracted from the baseline case as an example; however, the same reasoning applies to all cases. The x -axis reports the time in term of convective time units (tc), which is an estimate of the time it takes for the flow to go through the entire domain. More specifically, figure 7.5 shows 1536 CPU hours of computation, corresponding to 16400 time steps, while figure 7.6 shows 6144 CPU hours of computations, from time step 16400 to 89900. For the baseline case, the time step size is 10^{-7} s. The first figure shows the numerical transient of the simulation, which can be considered exhausted after 4 tc . In the second figure, it is possible to observe a null mass flow on average over time and therefore a statistically steady-state flow configuration. Moreover, the plots in figure 7.6 show a strongly periodic behavior. This behavior is linked to the blended turbulent box finite streamwise length generated by [7].

Once the convergence condition was reached, the time required to obtain stable time-average results was evaluated for each case. In some cases, the simulations were not run for sufficient time to allow smooth trends; however, the results can be considered representative.

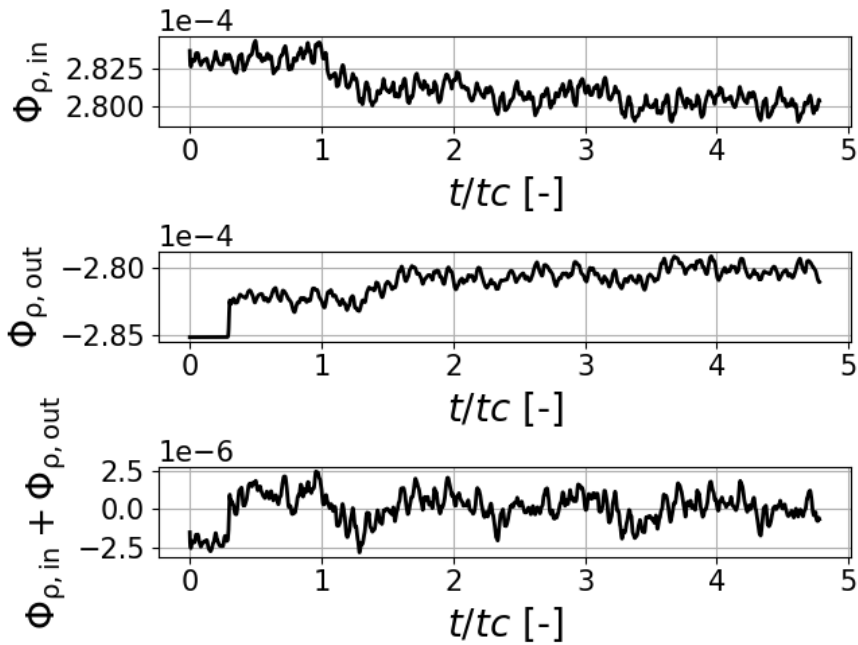


Figure 7.5: Convective density flux (Φ_{ρ} [$\text{kg m}^{-2} \text{s}^{-1}$]) during the numerical transient of the simulation

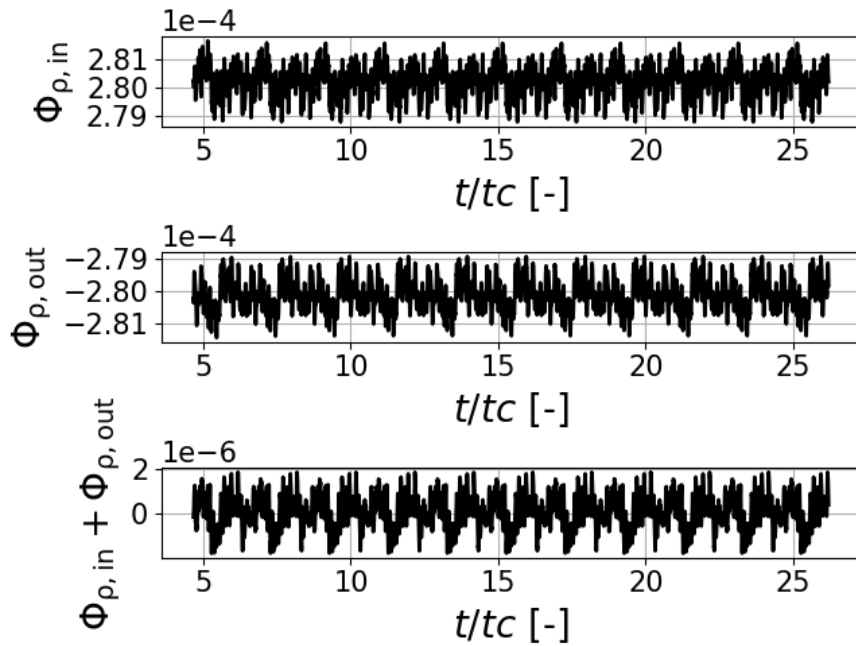


Figure 7.6: Convective density flux (Φ_{ρ} [$\text{kg m}^{-2} \text{s}^{-1}$]) of the converged simulation

7.1.5 Data extraction

To mitigate the usage of storage resources and the computational cost of post-processing the full flow field, data extraction was performed using a set of virtual probes. The probes are distributed in 48 planes, perpendicular to the streamwise direction, and evenly spaced within a region that extends from the inlet to $2 \times L$ upstream of the outlet (Figure 7.7). This extraction region was chosen to avoid the sponge layer (see Section 7.1.1).



Figure 7.7: Free domain probe set shown in red, 2-dimensional side-view

Two probes configuration were employed (Figure 7.8). The first one, with a high density of probes, was used to collect data such as time and space averaged quantities. The collection was carried out by co-processing, which is performed simultaneously with the simulation. This approach allows efficient calculation of statistical properties while minimizing storage requirements.

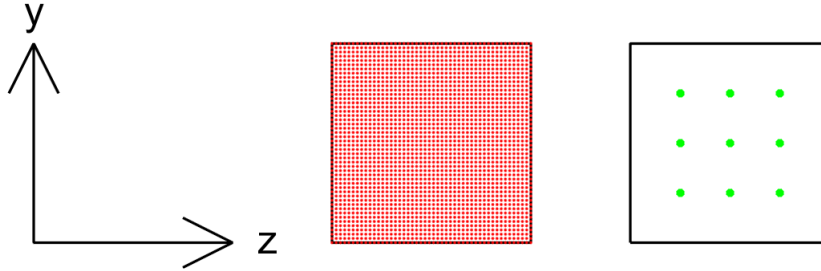


Figure 7.8: High density probe set shown in red (on the left) and low density probe set shown in green (on the right), 2-dimensional inlet view

The second configuration in Figure 7.8, with a much lower probe density, was used to capture instantaneous velocity data for the calculation of the streamwise evolution of the velocity integral length scale L_{XX} . Indeed, a different approach was employed to calculate L_{XX} compared to L_{YY} and L_{ZZ} . In the former case, the streamwise velocity component was extracted from the low density probe set at various time steps. Subsequently, in post-processing, the time series at different points was used to determine L_{XX} . For the other two integral length scales, spatial correlation (see Equation 2.25) was utilized through the high density probe set to directly compute the scales at several instants, while the values were time averaged via co-processing. It is worth specifying that the integral length scales calculated in Chapter 8 regarding the turbine simulation follow this second approach.

7.2 Results and discussion

The first case presented is the baseline case, which serves as a reference for subsequent analyses. After that, the effects of varying the following parameters are investigated:

1. Reynolds and Mach numbers,
2. inlet boundary conditions type,
3. injection angle, and
4. mesh.

Initially, the simulations were conducted starting from the baseline case and varying one parameter at a time. Subsequently, the combined effects of parameters 2, 3 and 4 are analyzed.

7.2.1 Baseline case

The characteristics of the baseline case are summarized in Table 7.1. This case was selected as a reference for subsequent simulations because it presents the same inlet conditions as those used by [7] for the low Mach number case, with the only difference that $\alpha_{in} = 0$. Additionally, the isotropic mesh was employed.

Figure 7.9 shows the diagonal terms of the Reynolds stress tensor. $\overline{u'u'}$, $\overline{v'v'}$, and $\overline{w'w'}$ have been time-averaged and averaged in the y and z directions. The x -axis represents the streamwise location, non-dimensionalized by the characteristic length of the precursor domain cube L . The same averaging procedures and non-dimensionalization of the x -axis apply to all results presented in this section.

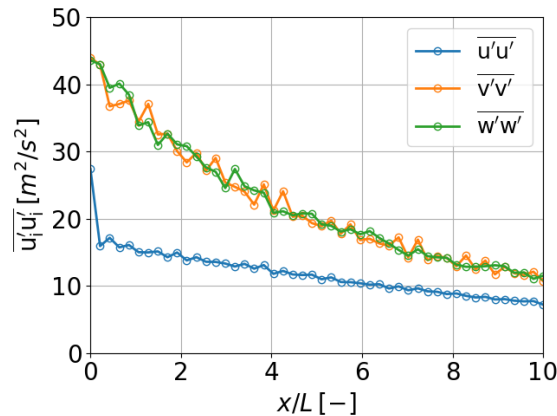


Figure 7.9: Streamwise evolution of diagonal terms of the Reynolds stress tensor for the base case

Turbulence anisotropy is evident in Figure 7.9, as $\overline{u'u'}$ is smaller than both $\overline{v'v'}$ and $\overline{w'w'}$. This difference is already present at the inlet and increases rapidly over a very short distance, due to the steep decrease of $\overline{u'u'}$. Moving towards the outlet, $\overline{v'v'}$ and $\overline{w'w'}$ decrease while remaining of the same order of magnitude. On the

other hand, $\overline{u'u'}$ decreases more slowly for most of the domain; in fact, the turbulence anisotropy decreases moving toward the outlet.

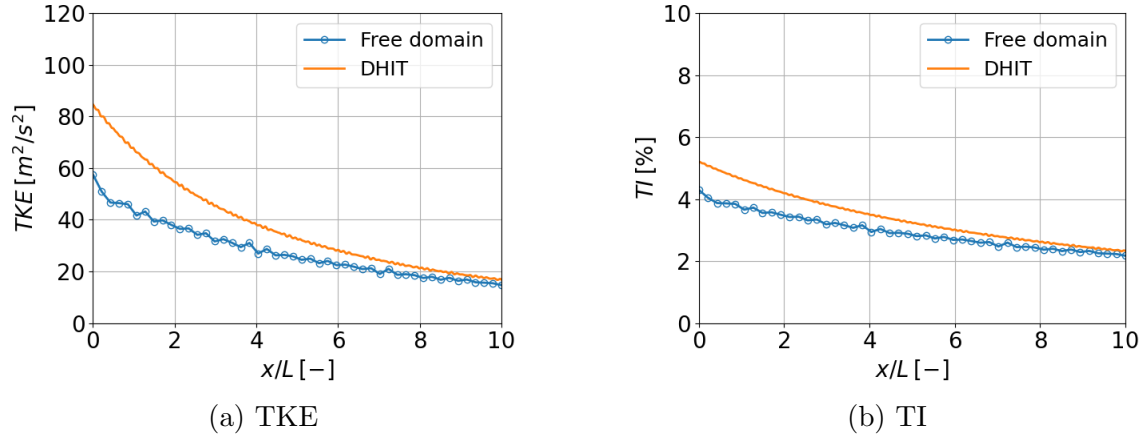


Figure 7.10: Streamwise evolution of the Turbulent Kinetic Energy (**left**) and Turbulent Intensity (**right**) for the base case

Figure 7.10a and Figure 7.10b show the streamwise evolution of the turbulent kinetic energy (TKE) and turbulence intensity (TI), respectively. In both figures, the blue curve represents the data extracted directly from the free domain, while the orange curve corresponds to the data obtained from the precursor domain. Specifically, the time evolution of TKE was extracted from the precursor box and then transformed into a spatial evolution using the convective velocity at the inlet of the free domain. This transformation was performed to enable a direct comparison between the two curves on the same plot. The TKE at the inlet of the orange curve corresponds to the time instant at which data was extracted from the precursor simulation for turbulence injection. However, a discrepancy in TKE is observed at the inlet between the two curves, indicating that part of the turbulent energy is lost during the injection process. Nevertheless, both the orange and blue curves have the same slope, therefore the turbulence decay is the same in both simulations.

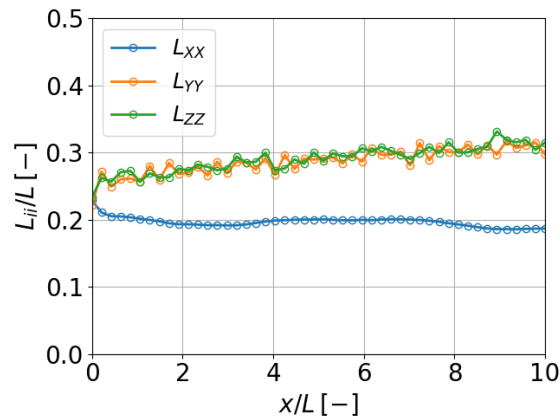


Figure 7.11: Streamwise evolution of velocity integral length scale for the base case

Figure 7.11 presents the streamwise evolution of the integral length scales in the x , y , and z directions, denoted as L_{XX} , L_{YY} , and L_{ZZ} , respectively. Similar to the

behavior observed for $\overline{u'u'}$, $\overline{v'v'}$, and $\overline{w'w'}$, the terms corresponding to the y and z directions are of the same order of magnitude throughout the domain, while the term corresponding to the x direction is smaller. However, contrary to the diagonal terms of the Reynolds stress tensor, L_{XX} , L_{YY} , and L_{ZZ} are equal at the inlet and then diverge rapidly.

7.2.2 Reynolds and mach numbers effect

In order to analyze the effect of the Reynolds number and the Mach number, four cases are compared. Table 7.2 shows the values of Re and M used, while the other parameters are the same of Table 7.1. The case with Re_1 and M_1 corresponds to the base case.

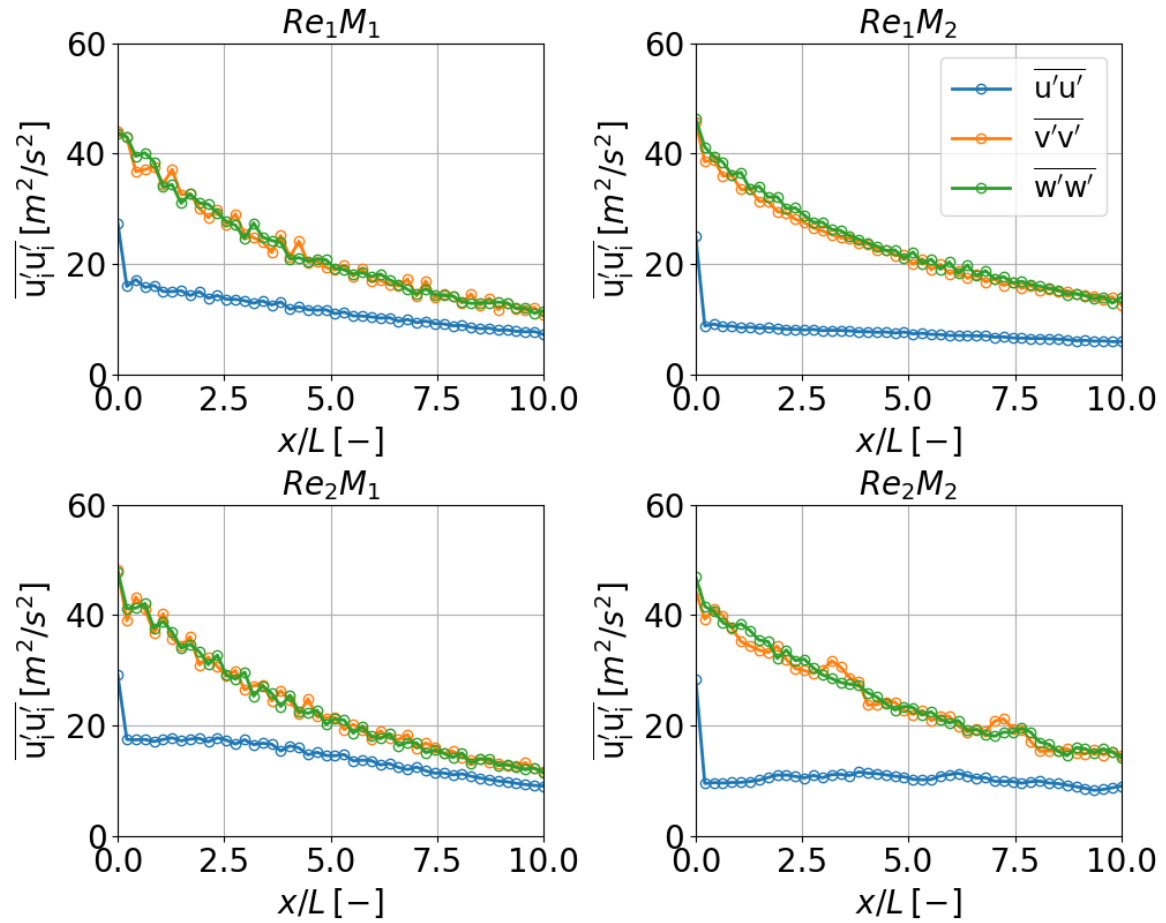


Figure 7.12: Streamwise evolution of diagonal terms of Reynolds stress tensor for different Re and M cases

Figure 7.12 shows the streamwise evolution of the diagonal terms of the Reynolds stress tensor for the four cases. All the plots have almost the same behavior. Nevertheless, M_2 cases seem to be slightly more anisotropic.

Figure 7.13a shows $\overline{u'u'}$ for the four cases. Although $\overline{u'u'}$ at the inlet is almost the same for each case, it has a step decrease which magnitude depends on the Mach number. In fact, cases with higher M have lower $\overline{u'u'}$ in the first part of the domain. Conversely, the slope of the plots seems to depend on the Reynolds

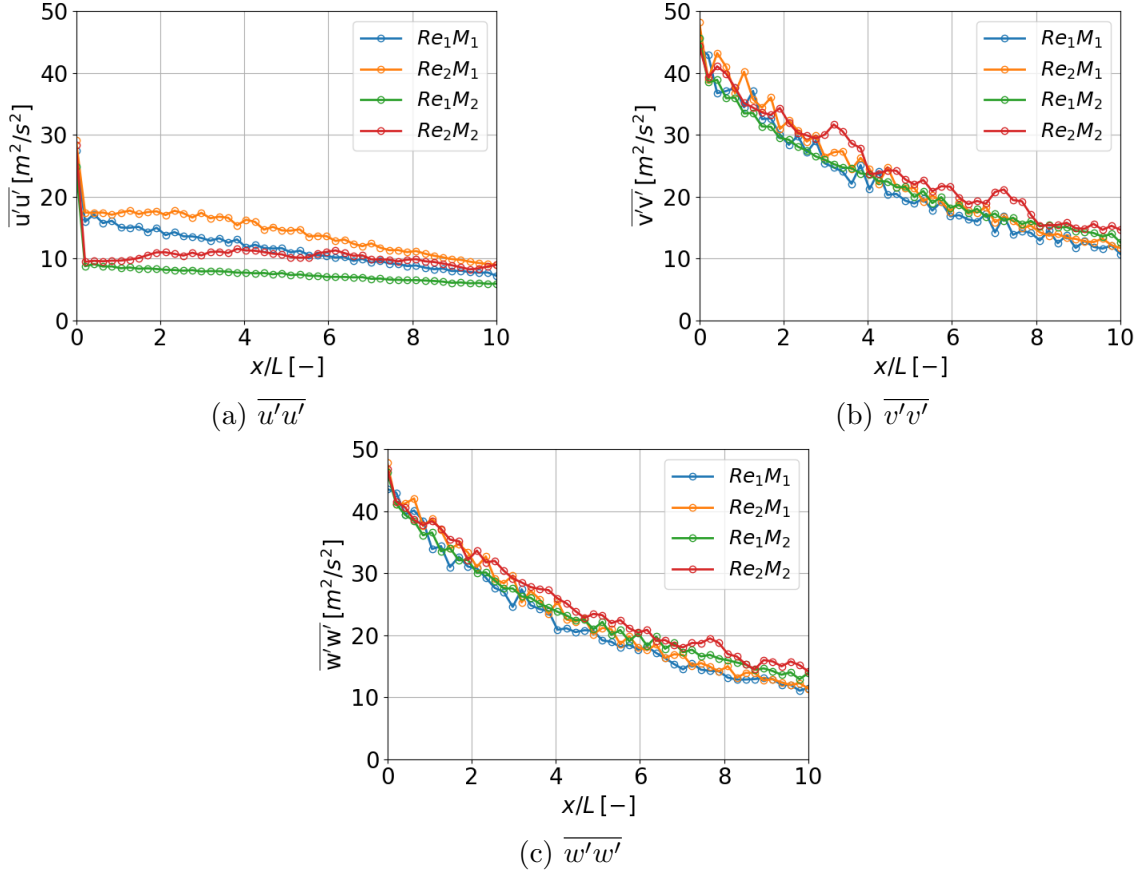


Figure 7.13: Streamwise evolution of $\overline{u'u'}$ (**top-left**), $\overline{v'v'}$ (**top-right**), and $\overline{w'w'}$ (**bottom**) for different Re and M cases

number: cases with higher Re have lower decrease of $\overline{u'u'}$ through the domain, and therefore, higher $\overline{u'u'}$ in the last part of the domain. The $\overline{v'v'}$ and $\overline{w'w'}$ evolution is shown in Figure 7.13b and Figure 7.13c respectively. The plots relative to different cases are almost overlapping, hence, Re and M have very slight effect on them.

The TKE of the four cases are shown in Figure 7.14. Since the precursor simulation to create the turbulence is the same for each case, the time evolution of TKE for the precursor box is also the same. Nevertheless, the convective velocity is different in each case, therefore the orange curve relative to the DHIT in function of the streamwise location is also different. In general, all cases present almost the same inlet energy gap of the baseline case, however the streamwise energy evolution is different from case to case: the mismatch between free domain and DHIT behavior increases with high M and decreases with high Re . In fact, for Re_2M_1 case the two curves are overlapped for most of the domain. Nevertheless, the baseline case demonstrates the closest agreement between the free domain curve's gradient and the precursor domain curve's gradient, probably because it is the only one with the same total boundary conditions at the inlet of the precursor simulation.

Figure 7.15 shows the L_{ii} of the four cases. In each case, the behavior is almost the same of the baseline case: the integral length scales are the same at the inlet, then L_{XX} rapidly diverge from L_{YY} and L_{ZZ} , while these last ones are of the same order of magnitude in the full domain. Furthermore, the L_{ii} anisotropy increases

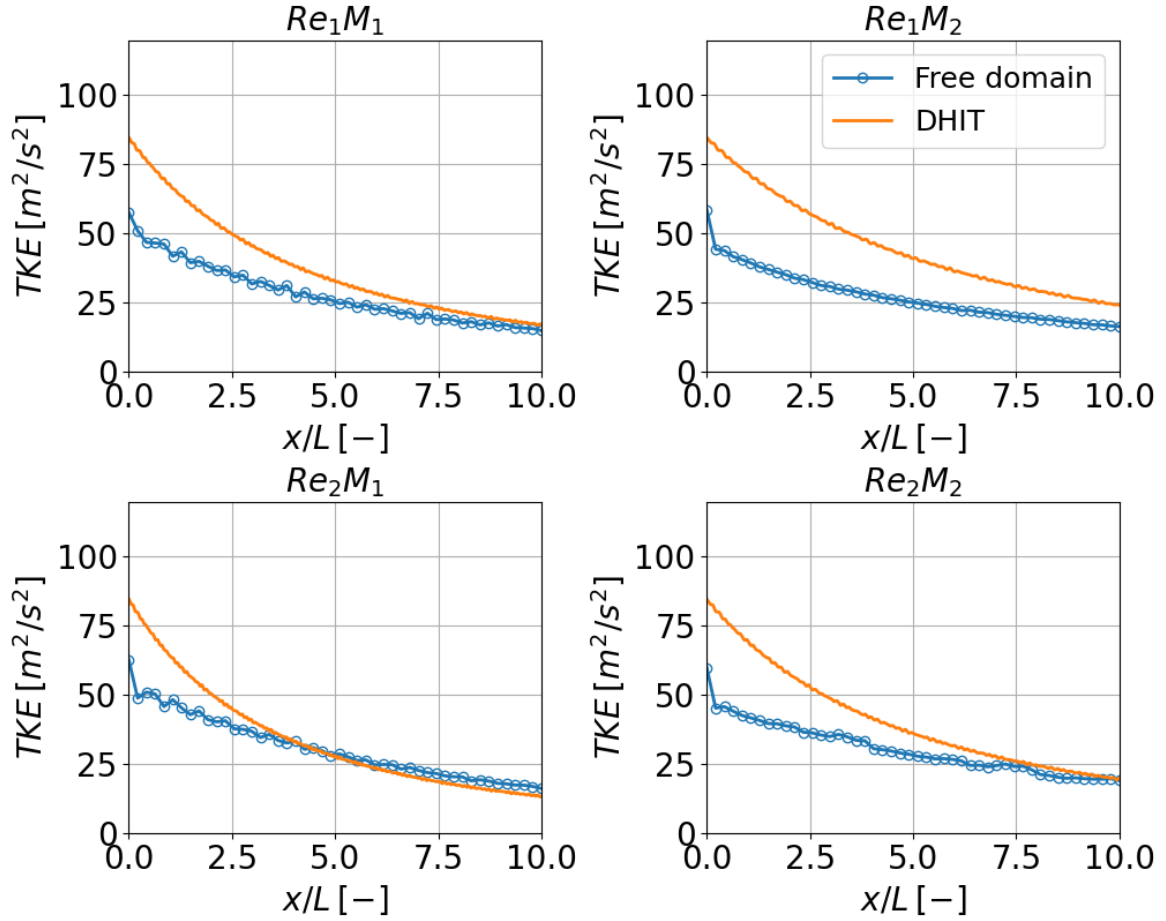


Figure 7.14: Streamwise evolution of the Turbulent Kinetic Energy for different Re and M cases

with high M and decrease with high Re .

Figure 7.16a shows L_{XX} evolution for the four cases. The behavior of the plot is dominated mostly by the M , in fact cases with higher M have lower L_{XX} . Comparing cases with the same M is also possible to observe the effect of the Re : increasing Re leads to a decrease of L_{XX} .

Figure 7.16b and Figure 7.16c show L_{YY} and L_{ZZ} respectively. In contrast with L_{XX} , for these cases the behavior of the plots is dominated by the Re : increase the Re leads to a decrease of the integral length scales. There is also a slight effect of the M : increase the M leads to an increase of the curves.

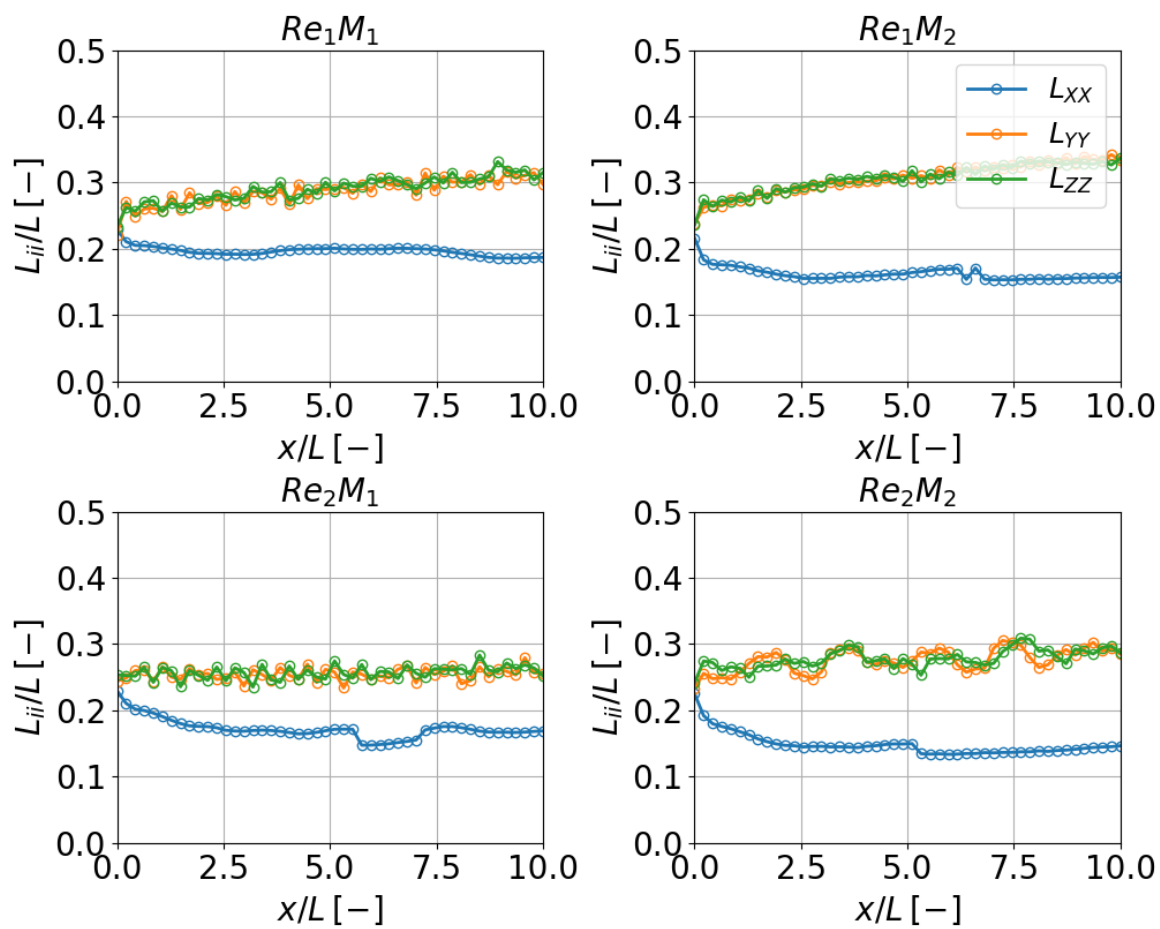


Figure 7.15: Streamwise evolution of velocity integral length scale for different Re and M cases

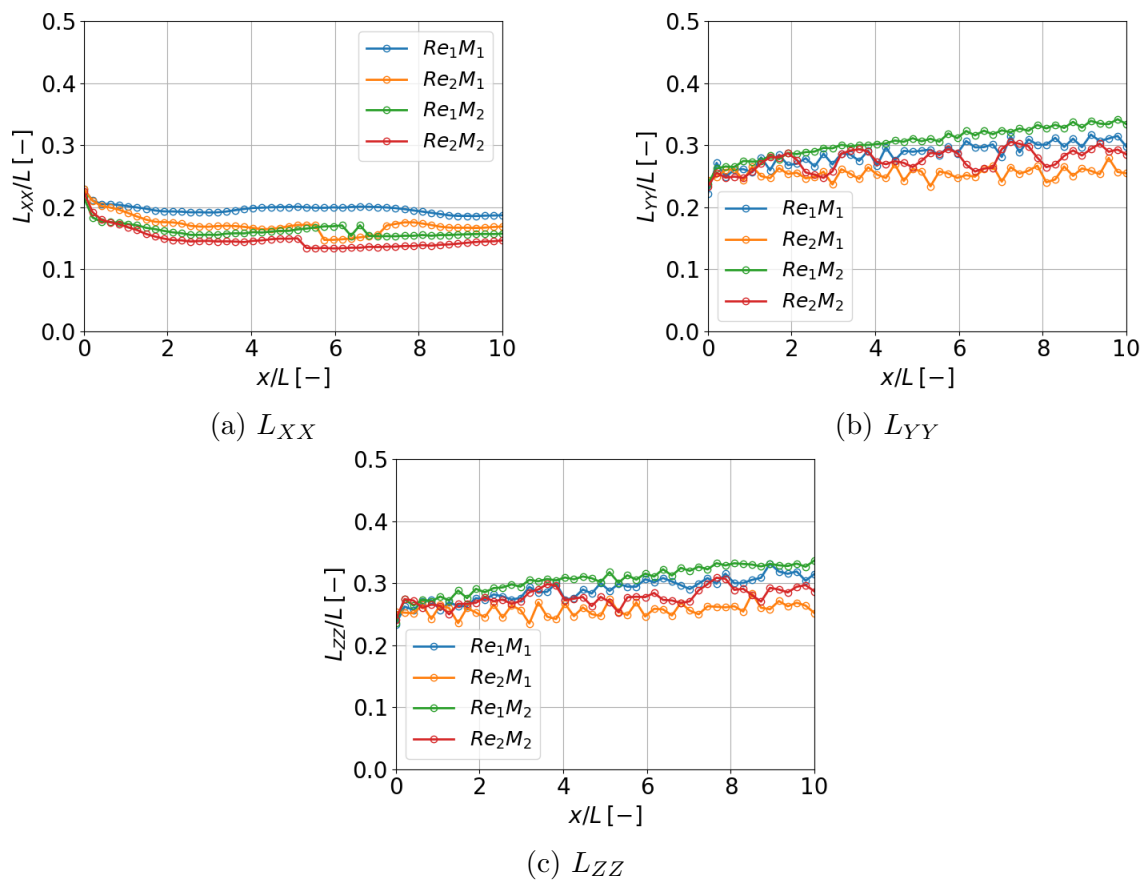


Figure 7.16: Streamwise evolution of L_{XX} (**top-left**), L_{YY} (**top-right**), and L_{ZZ} (**bottom**) for different Re and M cases

7.2.3 Boundary condition type effect

This section will discuss the effect of changing the inlet boundary conditions type of the baseline case, from Mach total to Free stream. The other parameters of the simulation are kept the same, as shown in Table 7.1.

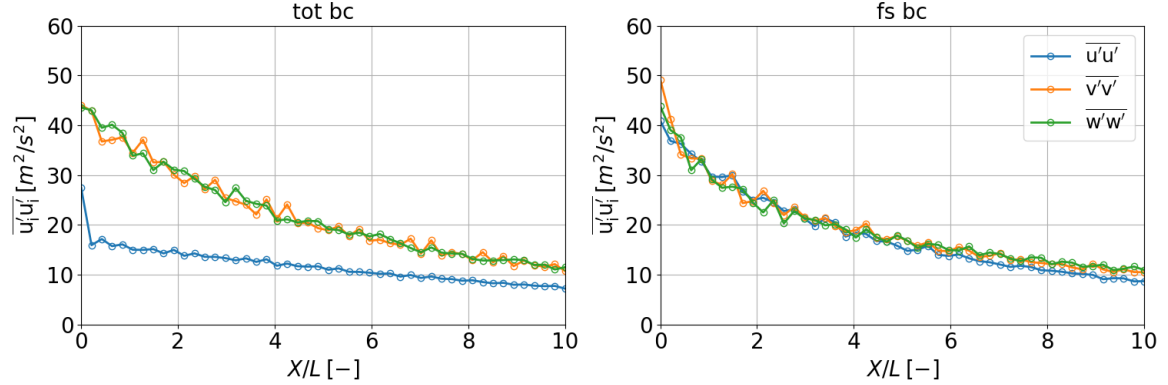


Figure 7.17: Streamwise evolution of diagonal terms of Reynolds stress tensor for different inlet boundary conditions type

Figure 7.17 shows the streamwise evolution of the diagonal terms of the Reynolds stress tensor for the baseline case (with Mach total boundary conditions) and for the Free stream case. In the second simulations, $\overline{u'u'}$, $\overline{v'v'}$ and $\overline{w'w'}$ are of the same order of magnitude throughout the domain, therefore the turbulence is isotropic in all streamwise locations.

Figure 7.18a shows the $\overline{u'u'}$ for the two cases. Compared to baseline case, Free stream conditions lead to higher $\overline{u'u'}$ in all streamwise locations, without a step decrease near the inlet and with a greater decay throughout the domain. Otherwise, $\overline{v'v'}$ and $\overline{w'w'}$, shown respectively in Figure 7.18b and Figure 7.18c, are slightly lower for the Free Stream case, but they have similar behavior compared to the baseline case.

In Figure 7.19 is possible to see that the TKE streamwise evolution of the two cases is almost the same. In fact, the large increase of turbulent kinetic energy associated with the x direction for the Free stream case is compensated by the decrease of energy associated with both y and z directions. However, the two TKE curves are slightly different near the inlet, where there is more energy for the Free stream case. As a consequence, changing the boundary conditions type, the energy gap between the free domain and the DHIT becomes smaller, but still present. Since the superimposition of turbulent fluctuations on the mean flow at the inlet is not perfectly physical, this probably leads to a rapid dissipation of small scales, and consequently to a drop of energy.

Figure 7.20 shows the velocity integral length scales in the three directions for the two cases. Changing the inlet boundary condition type from Mach total to Free stream leads to a large increase of L_{XX} , which becomes much closer to L_{YY} and L_{ZZ} . Therefore, the three curves have a very similar behavior, but only in the first half of the domain. Indeed, L_{XX} diverges from the other integral length scales in

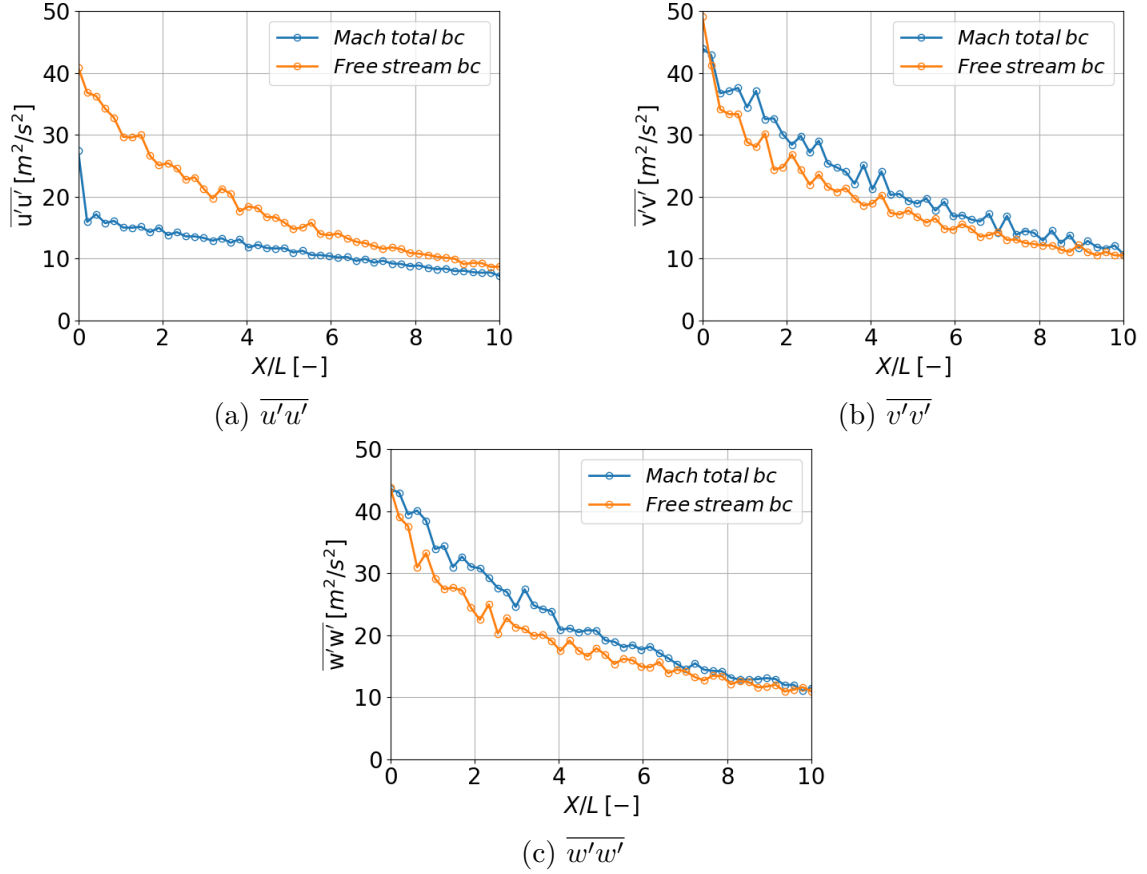


Figure 7.18: Streamwise evolution of $\overline{u'u'}$ (**top-left**), $\overline{v'v'}$ (**top-right**), and $\overline{w'w'}$ (**bottom**) for different inlet boundary conditions type

the second half, though much less compared to the Mach total case.

Figure 7.21a, Figure 7.21b and Figure 7.21c show respectively L_{XX} , L_{YY} and L_{ZZ} for the two cases. These plots highlight that the only integral length scale to change with the boundary conditions type is L_{XX} , while the others are almost unchanged. Although the L_{XX} is the same at the inlet for both simulation, the behavior shortly after is totally the opposite. For the Mach total case the curve slightly decrease and rapidly settles at 0.2, while for the Free stream case curve tends to oscillate around 0.3.

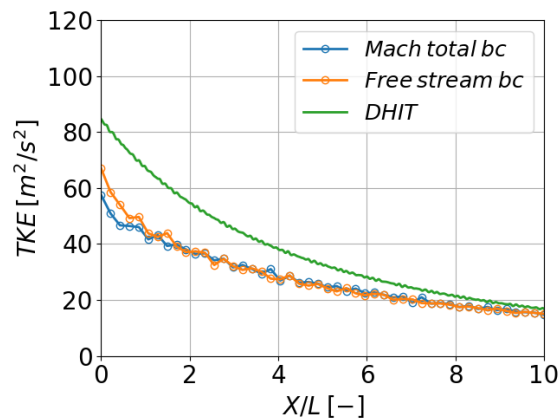


Figure 7.19: Streamwise evolution of the Turbulent Kinetic Energy for different inlet boundary conditions type

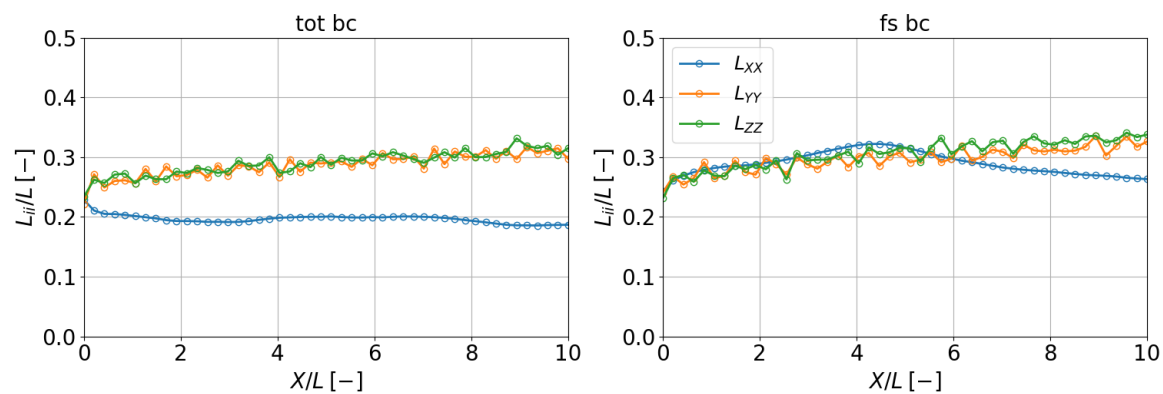


Figure 7.20: Streamwise evolution of velocity integral length scale for different inlet boundary conditions type

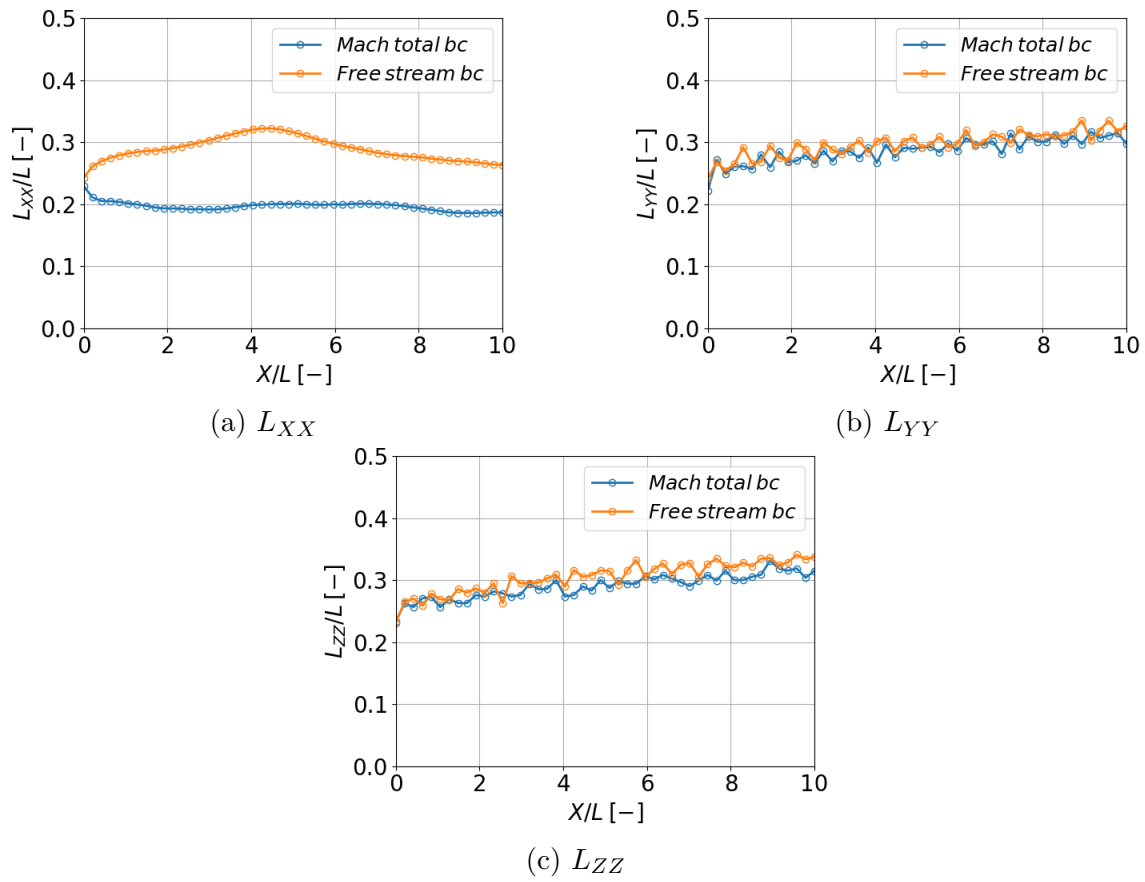


Figure 7.21: Streamwise evolution of L_{XX} (**top-left**), L_{YY} (**top-right**), and L_{ZZ} (**bottom**) for different inlet boundary conditions type

7.2.4 Injection angle effect

This section presents the results of simulations with different injection angles, using both Mach total and Free stream boundary conditions. The injection angle is changed in the xy -plane in each case (see Table 7.8). The angles were chosen in such a way as to cover the values normally found in turbines.

Injection angle α_{in} [°]	Injection vector [x,y,z]
0	[1, 0, 0]
26.565	[2, 1, 0]
63.435	[1, 2, 0]

Table 7.8: Injection angles and related injection vectors

To properly compare the effect of α_{in} , the curves present in this section are plotted as functions of \tilde{x}/L , where \tilde{x} is the axis of a relative reference frame obtained rotating the absolute one around the z axis of an angle equal to the injection angle in each case.

Mach total condition cases

Figure 7.22 shows the streamwise evolution of the diagonal terms of the Reynolds stress tensor for different α_{in} , obtained using the Mach total boundary conditions. Compared to the zero injection angle case (which corresponds to the baseline case), the effect of the low injection angle ($\alpha_{in} = 26.565^\circ$) is really slight. Indeed, the general behavior of the three curve is quiet similar, except for the fact that $\overline{v'v'}$ and $\overline{w'w'}$ are not overlapping anymore. Otherwise, the high injection angle ($\alpha_{in} = 63.435^\circ$) has a large effect, especially for $\overline{v'v'}$, that is much higher than $\overline{u'u'}$ and $\overline{w'w'}$. Furthermore, for this last case $\overline{u'u'}$ and $\overline{w'w'}$ are of the same order of magnitude.

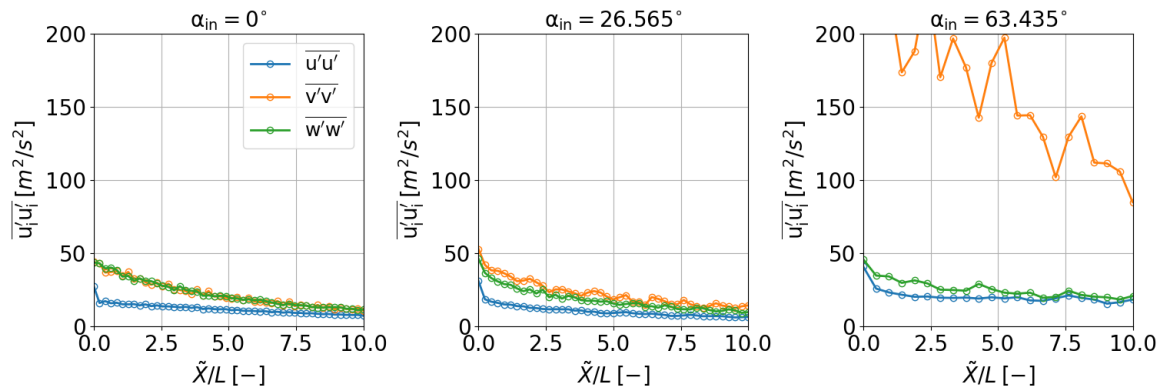


Figure 7.22: Streamwise evolution of diagonal terms of Reynolds stress tensor for different α_{in} , using Mach total boundary conditions

Figure 7.23a, Figure 7.23b and Figure 7.23c show respectively $\overline{u'u'}$, $\overline{v'v'}$ and $\overline{w'w'}$ for the different α_{in} cases. Regarding $\overline{u'u'}$, the curves of $\alpha_{in} = 0^\circ$ and $\alpha_{in} = 26.565^\circ$ cases are really close, while the curve of $\alpha_{in} = 63.435^\circ$ is slightly higher. Also for $\overline{v'v'}$, there is no difference between zero and low injection angle, but the effect of

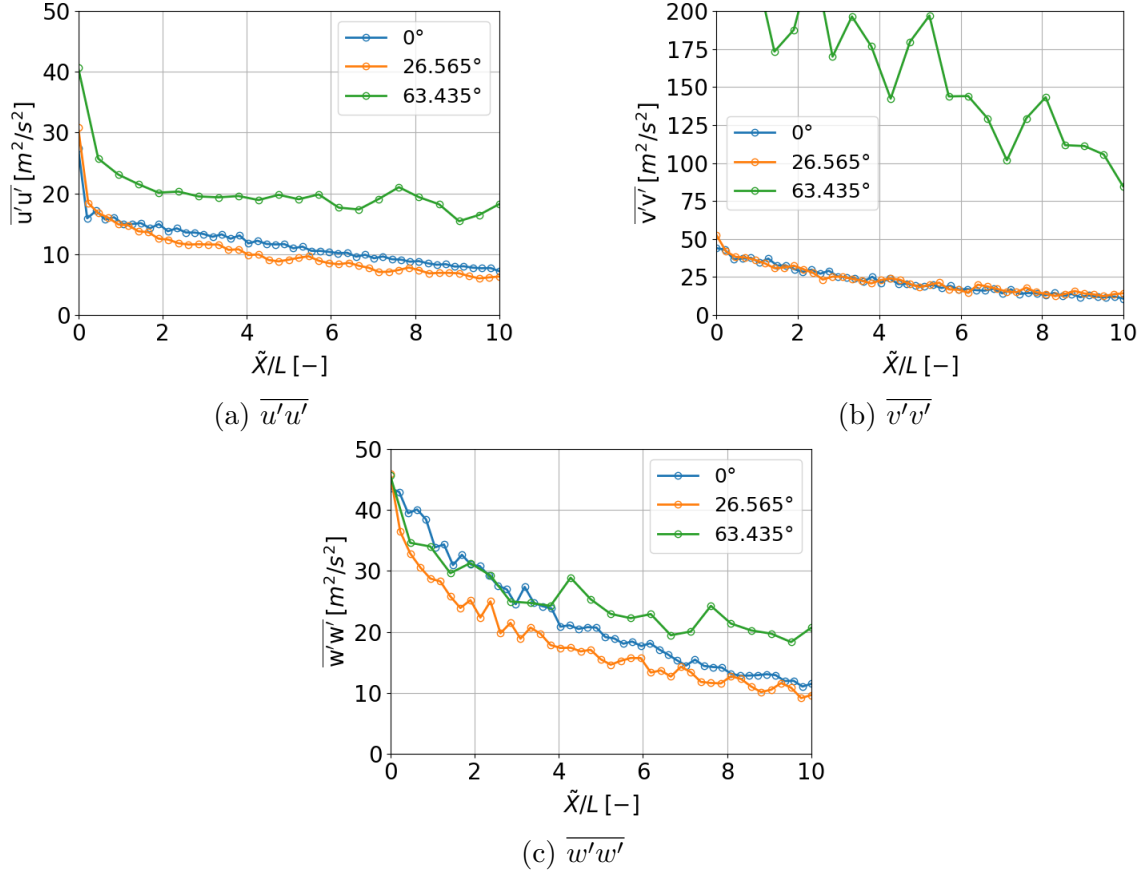


Figure 7.23: Streamwise evolution of $\overline{u'u'}$ (**top-left**), $\overline{v'v'}$ (**top-right**), and $\overline{w'w'}$ (**bottom**) for different α_{in} , using Mach total boundary conditions

the high angle is much larger. Lastly, the low injection angle leads to a decrease of $\overline{w'w'}$ throughout the domain, while the high injection angle curve is of the same order of magnitude of $\alpha_{in} = 0^\circ$ in the first half of the domain and then it becomes the highest among the three for the second half. In general, in all diagonal terms of the Reynolds stress tensor, the curves related to $\alpha_{in} = 63.435^\circ$ are less smooth, particularly for the $\overline{v'v'}$ plot.

Figure 7.24 shows the evolution of the TKE for the three cases compared to the DHIT. The curves behavior is in accordance with the evolution of the Reynolds stress tensor: the curves of zero and low injection angle are really close, while the TKE for $\alpha_{in} = 63.435^\circ$ is much larger and also less smooth. Probably, the high injection angle generates non-physical energy, especially in velocity fluctuations in the y direction. Furthermore, the TKE in the high angle case is higher than the TKE in the precursor box.

Figure 7.25 shows the velocity integral length scales in the three directions for the three cases. One of the first aspects to look at is that L_{YY} and L_{ZZ} have a different evolution when the injection angle is not zero. Another aspect is that L_{XX} is notably lower compared to the other integral length scales for the zero and low injection angles, while is almost of the same order of magnitude of L_{YY} for the high injection angle case.

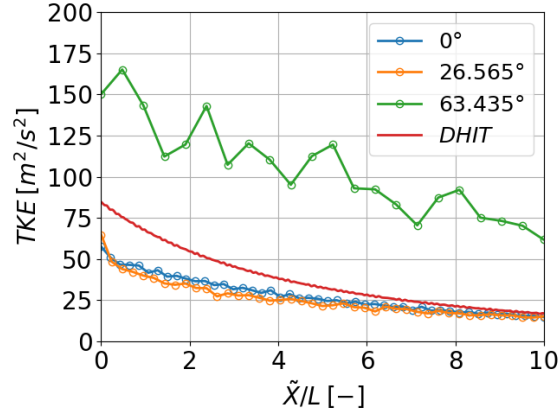


Figure 7.24: Streamwise evolution of the Turbulent Kinetic Energy for different α_{in} , using Mach total boundary conditions

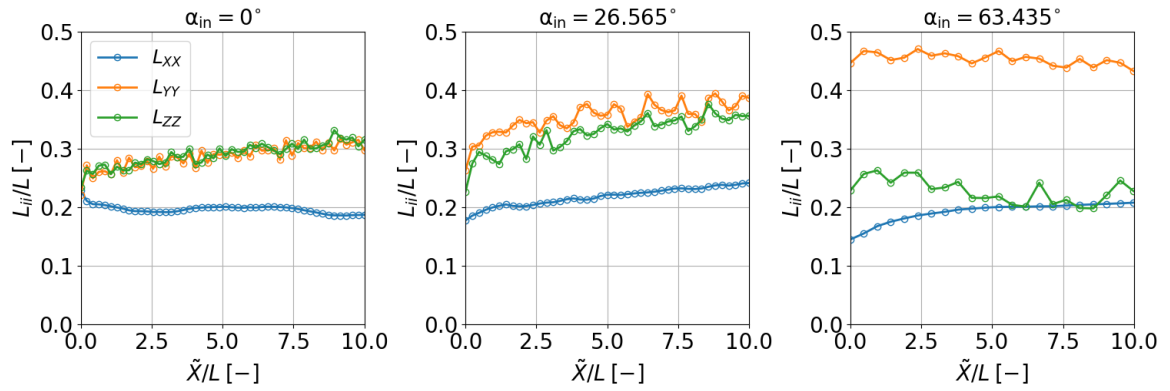


Figure 7.25: Streamwise evolution of velocity integral length scale for different α_{in} , using Mach total boundary conditions

Figure 7.26a, Figure 7.26b and Figure 7.26c shows respectively L_{XX} , L_{YY} and L_{ZZ} for the three cases. Regarding L_{XX} , the curve related to $\alpha_{in} = 0^\circ$ is the only one approximately constant through the domain, while the curves of $\alpha_{in} = 26.565^\circ$ and $\alpha_{in} = 63.435^\circ$ increase along the streamwise direction. Moreover, L_{XX} for the zero and low injection angles is almost the same near the inlet and then it diverges going to the outlet. Otherwise, in the high injection angle case, the curve is lower at the inlet, but it rapidly reach the $\alpha_{in} = 0^\circ$ evolution and stabilizes at the same values. Regarding L_{YY} curves, the mean value increase α_{in} , indeed $(L_{YY})_{\alpha_{in}=63.435^\circ} > (L_{YY})_{\alpha_{in}=26.565^\circ} > (L_{YY})_{\alpha_{in}=0^\circ}$. For the L_{ZZ} plot, the inlet values are approximately the same in the three cases, but the curve related to the low injection angle increases compared to $\alpha_{in} = 0^\circ$ through the domain, while the curve related to the high injection angle case tends to decrease.

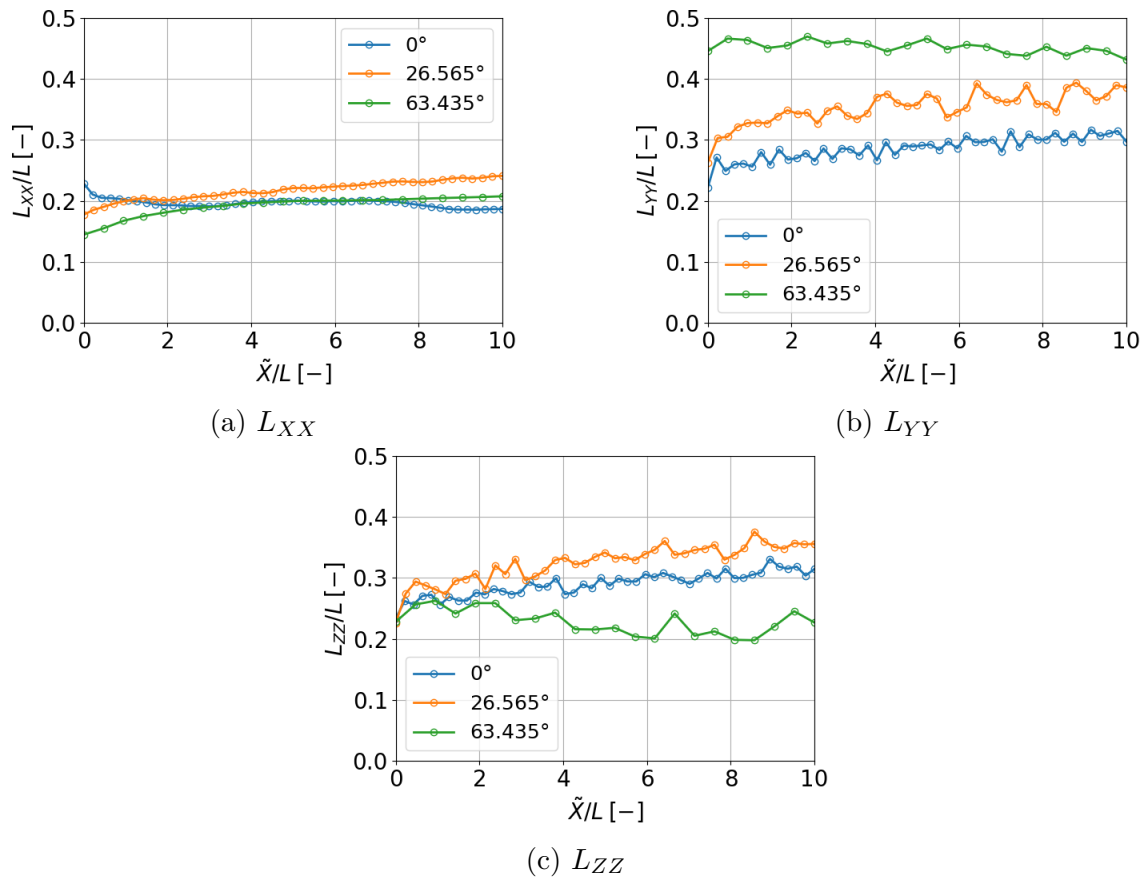


Figure 7.26: Streamwise evolution of L_{XX} (**top-left**), L_{YY} (**top-right**), and L_{ZZ} (**bottom**) for different α_{in} , using Mach total boundary conditions

Free stream condition cases

Figure 7.27 shows the streamwise evolution of the diagonal terms of the Reynolds stress tensor for different α_{in} , obtained using the Free stream boundary conditions. With these boundary conditions, the injection angle has no effect on $\overline{u'u'}$, $\overline{v'v'}$ and $\overline{w'w'}$, therefore the three turbulent flows are isotropic throughout the domain. As a consequence, the TKE evolution is the same in all cases.

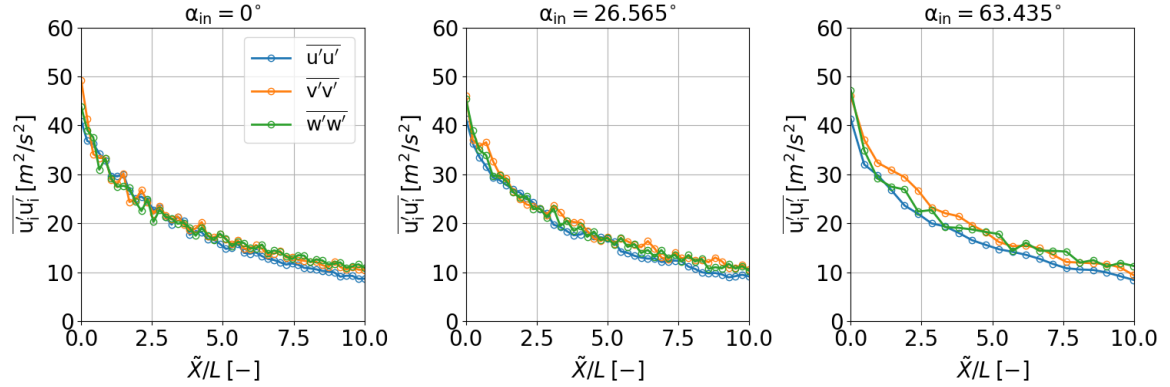


Figure 7.27: Streamwise evolution of diagonal terms of Reynolds stress tensor for different α_{in} , using Free stream boundary conditions

Figure 7.28 shows the evolution of the integral length scales. In this analysis, α_{in} does not affect L_{YY} and L_{ZZ} , but leads to a lower L_{XX} . As a consequence, the difference between L_{XX} and the other integral length scales increase with the injection angle.

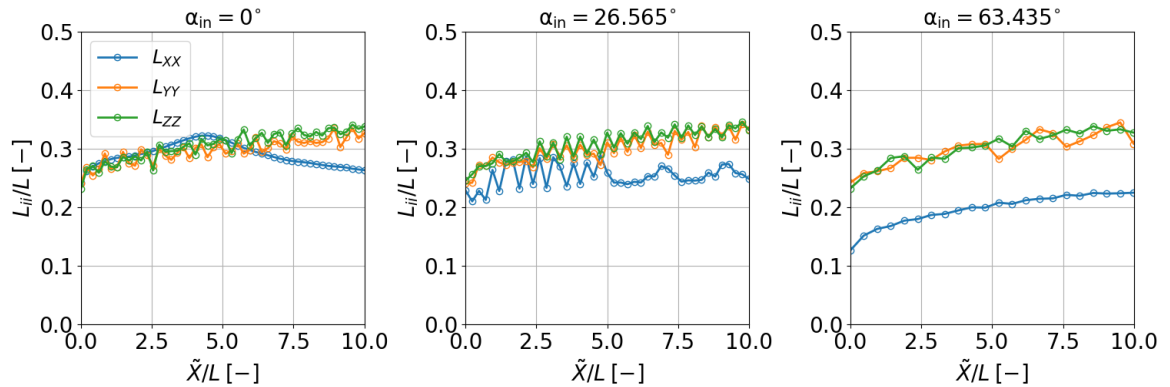


Figure 7.28: Streamwise evolution of velocity integral length scale for different α_{in} , using Free stream boundary conditions

Figure 7.29 focuses on the L_{XX} evolution for the three cases. Increasing the injection angle from 0° to 26.565° does not change the integral length scale at the inlet, but it decreases in the rest of the domain. On the other hand, for the high injection angle case, L_{XX} is much lower at the inlet, but it increases going downstream.

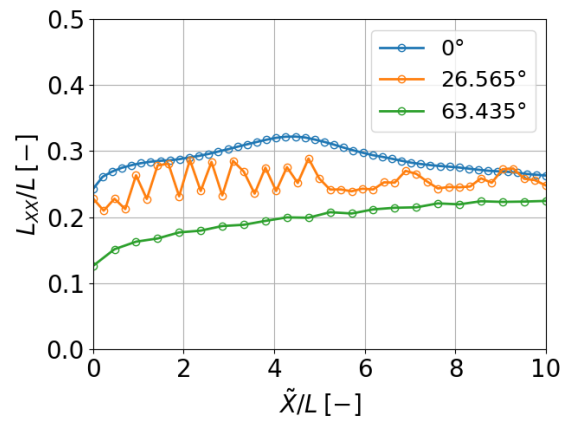


Figure 7.29: Streamwise evolution of L_{XX} for different α_{in} , using Free stream boundary conditions

7.2.5 Mesh isotropy effect

This section contains the results of simulations with different meshes. As discussed in Section 7.1.1, one mesh is isotropic while the other is anisotropic (Figure 7.3). The isotropic mesh is the same used for the baseline case. Similarly to Section 7.2.4, the simulations with different meshes have been run using both Mach total and Free stream boundary conditions. The results in this section are run with zero injection angle.

Mach total conditions cases

Figure 7.30 shows the $\overline{u'u'}$ streamwise evolution for the isotropic mesh and the anisotropic one. The two curves are perfectly overlapping throughout the domain. Also, the curve related to the evolution of $\overline{v'v'}$ and $\overline{w'w'}$ have the same behavior with the two meshes. As a consequence, the TKE evolution is the same for the two meshes as well. To avoid redundancy, the figures pertaining $\overline{v'v'}$, $\overline{w'w'}$ and the TKE are not included.

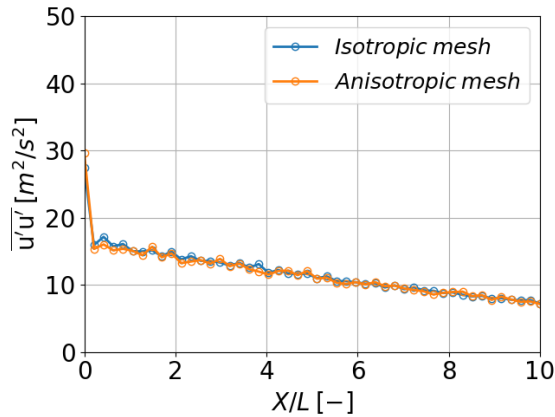


Figure 7.30: Streamwise evolution of $\overline{u'u'}$ for different meshes, using Mach total boundary conditions

Figure 7.31 shows the L_{XX} streamwise evolution for the two meshes and also in this case there is no difference between the curves. In the same way, the mesh does not affect L_{YY} and L_{ZZ} , therefore the related figures are omitted for redundancy reasons.

In conclusion, regarding the Mach total cases with $\alpha_{in} = 0^\circ$, the mesh seems to have no effect on the diagonal terms of the Reynolds stress tensor or on the integral length scales.

Free stream conditions cases

Figure 7.32a, Figure 7.32b and Figure 7.32c show respectively the evolution of $\overline{u'u'}$, $\overline{v'v'}$ and $\overline{w'w'}$ for the isotropic mesh and the anisotropic one, obtained using Free stream boundary conditions and $\alpha_{in} = 0^\circ$. In these cases, the change of mesh leads to an increase of the diagonal terms of the Reynolds stress tensor. At the inlet, the increase is slight, but through the domain it is more evident.

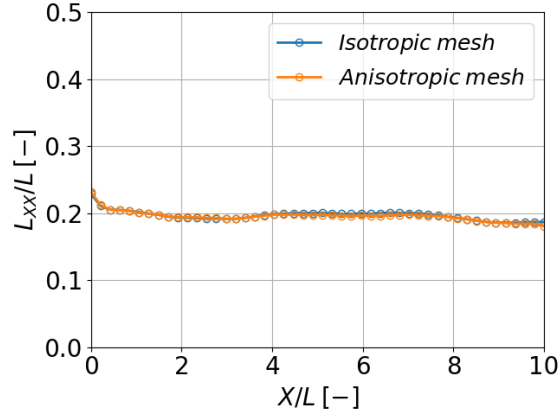


Figure 7.31: Streamwise evolution of L_{XX} for different meshes, using Mach total boundary conditions

Figure 7.33 shows the diagonal terms on the same plot for each mesh. Although the new mesh is anisotropic, the turbulence with Free stream boundary conditions is still isotropic. Indeed the increase of $\overline{u'u'}$, $\overline{v'v'}$ and $\overline{w'w'}$ is of the same order of magnitude, even if the mesh has been refined only in the z direction (see Section 7.1.1).

Figure 7.34 shows the TKE evolution for the two meshes of the free domain, compared to the DHIT. Since the new mesh has almost no effect on the Reynolds stress at the inlet, the energy gap between the main simulation and the precursor simulation is still present. Nevertheless, the curve of the anisotropic mesh is closer to the curve of the precursor simulation compared to the isotropic mesh. Indeed, the orange and the green curves are overlapping in the second half of the free domain. However, the slope for the box is closer to the isotropic mesh compared to the anisotropic one, probably because the first mesh has the same spatial discretization of the precursor box. Apparently, refining the mesh leads to a slower turbulence decay, and thus to a less decreasing curve.

Figure 7.35a, Figure 7.35b and Figure 7.35c show respectively the L_{XX} , L_{YY} and L_{ZZ} evolution for the two meshes. In general, all the integral length scales decrease with the second mesh. They also tend to maintain the inlet value throughout the domain, even if L_{XX} decreases slightly near the outlet.

Figure 7.36 shows the integral length scales on the same plot for each mesh. Although the mesh has been refined only in the z direction, the three scales in the anisotropic mesh are of the same order of magnitude for most of the domain, since L_{XX} begins to diverge from L_{YY} and L_{ZZ} to lower values after about six boxes.

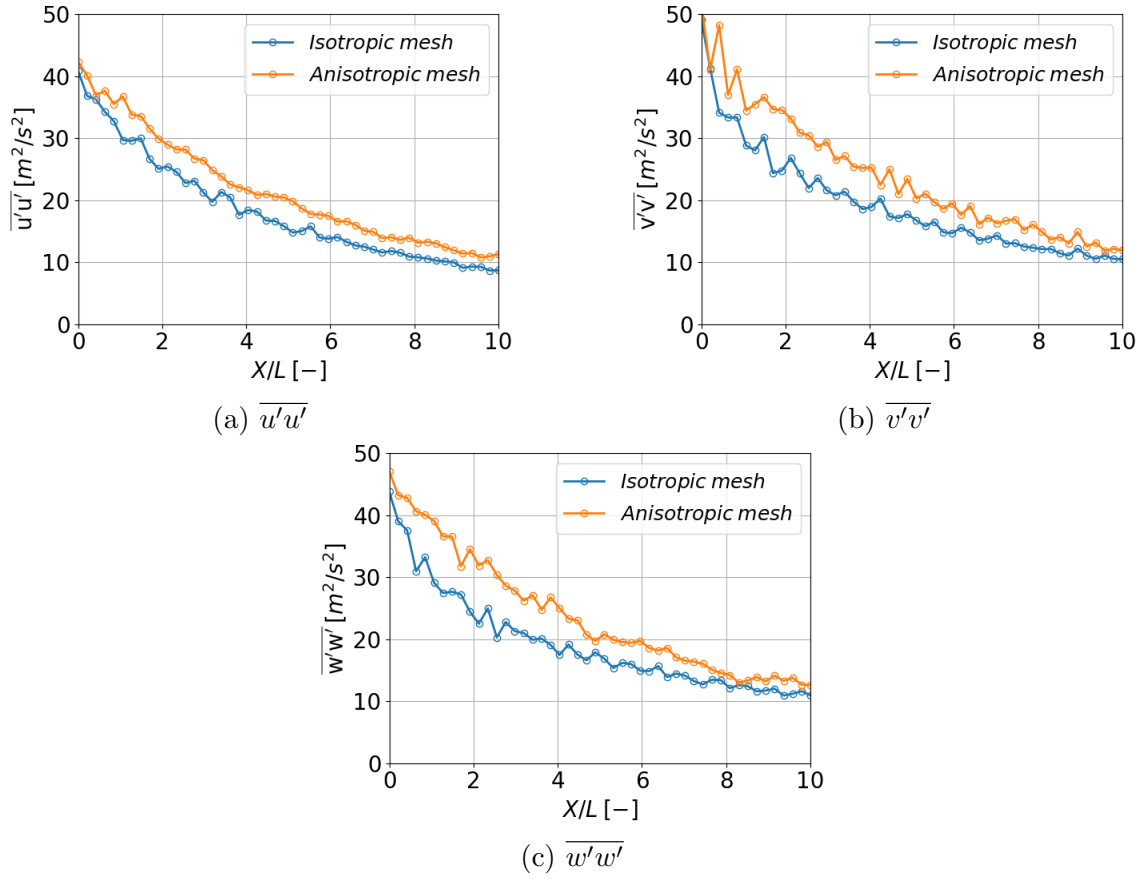


Figure 7.32: Streamwise evolution of $\overline{u'u'}$ (**top-left**), $\overline{v'v'}$ (**top-right**), and $\overline{w'w'}$ (**bottom**) for different meshes, using Free stream boundary conditions

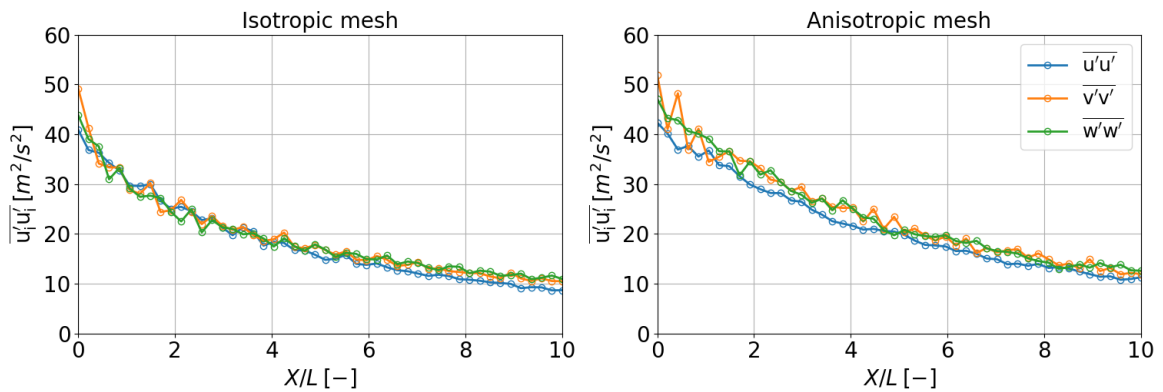


Figure 7.33: Streamwise evolution of diagonal terms of Reynolds stress tensor for different meshes, using Free stream boundary conditions

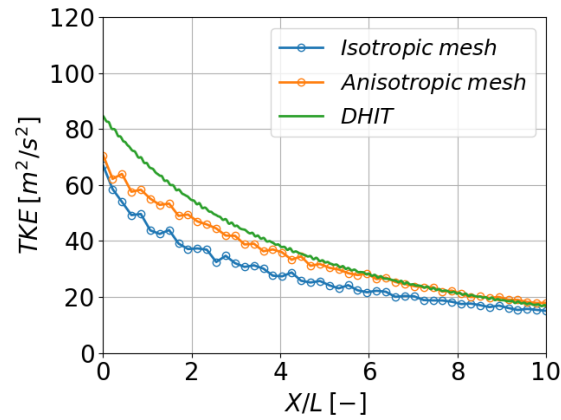


Figure 7.34: Streamwise evolution of the Turbulent Kinetic Energy for different meshes, using Free stream boundary conditions

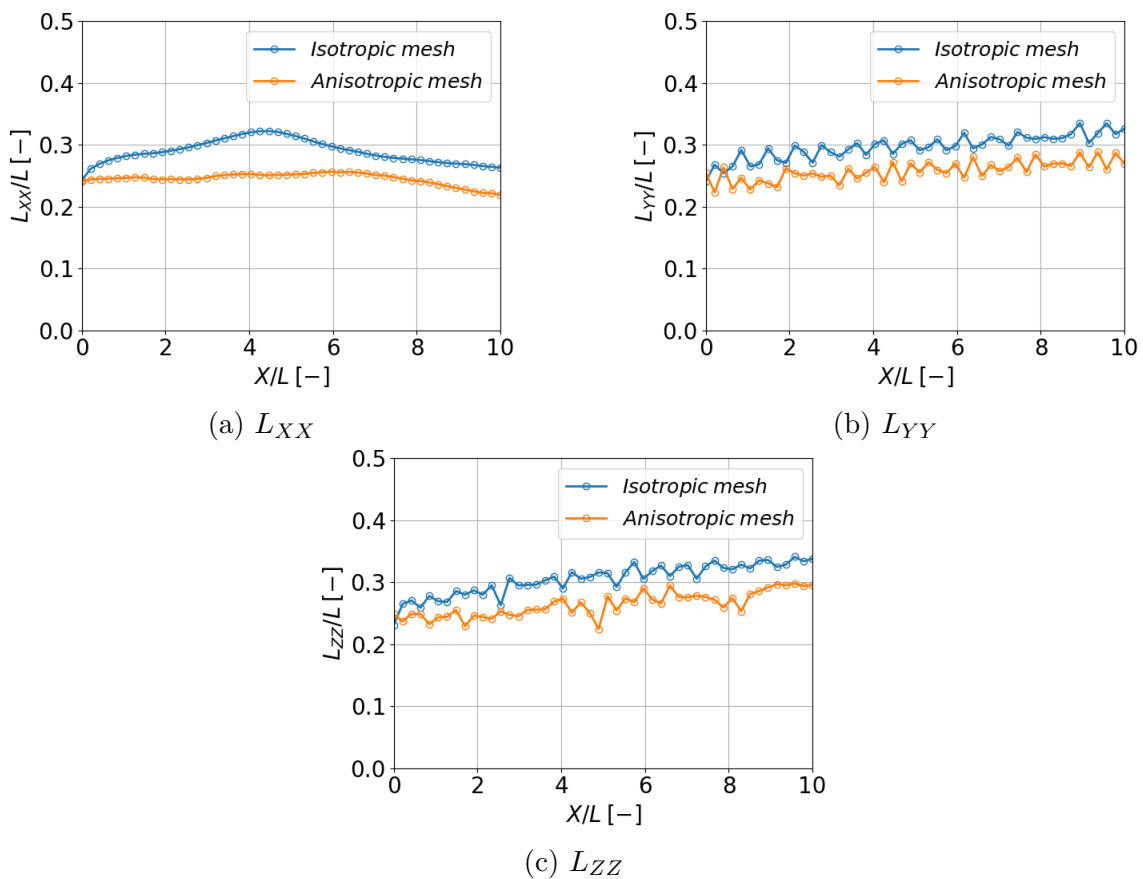


Figure 7.35: Streamwise evolution of L_{XX} (**top-left**), L_{YY} (**top-right**), and L_{ZZ} (**bottom**) for different different meshes, using Free stream boundary conditions

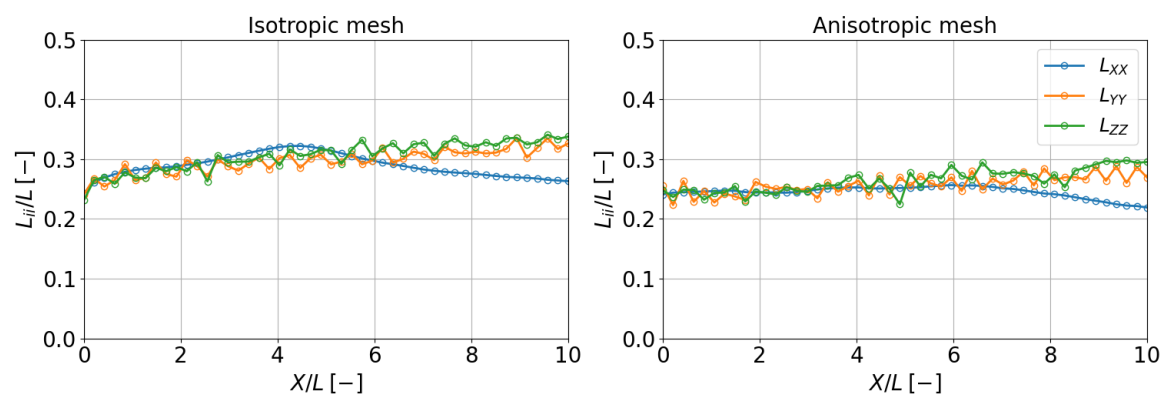


Figure 7.36: Streamwise evolution of velocity integral length scale for different meshes, using Free stream boundary conditions

7.2.6 Mesh isotropy effect with non-zero injection angle

This section will discuss the results of simulations with different meshes, but, differently from Section 7.2.5, in these cases $\alpha_{in} \neq 0^\circ$. The computations have been run using both Mach total and Free stream boundary conditions. Similarly to Section 7.2.4, the \tilde{x} axis of the plots in this section is related to a relative reference frame.

Mach total conditions cases

Figure 7.37a and Figure 7.37b show the $\overline{u'u'}$ streamwise evolution for the two different meshes, respectively, for $\alpha_{in} = 26.565^\circ$ and $\alpha_{in} = 63.435^\circ$. Differently for Subsection 7.2.5, in these cases the mesh seems to have an effect on the solution. Indeed, the plots related to the simulations with the anisotropic mesh are above the plots related to the isotropic mesh.

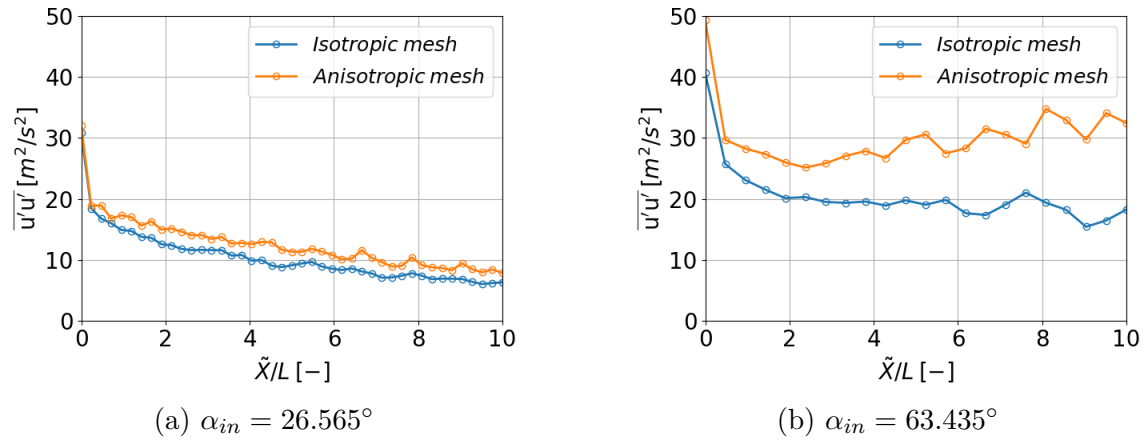


Figure 7.37: Streamwise evolution of $\overline{u'u'}$ for different meshes, using Mach total boundary conditions and with $\alpha_{in} \neq 0^\circ$

For simplicity reasons, the graphs related to $\overline{v'v'}$ and $\overline{w'w'}$ are not shown, but in general the effect of the anisotropic mesh is the same as exhibited by $\overline{u'u'}$, that is an increase of the curves compared to the isotropic mesh cases. Furthermore, the increase of the orange curves seems to be larger for the high injection angle cases.

Figure 7.38a and Figure 7.38b show the TKE evolution for the two meshes, respectively, for $\alpha_{in} = 26.565^\circ$ and $\alpha_{in} = 63.435^\circ$. Since the refined mesh leads to an increase of the diagonal terms of the Reynolds stress tensor, the TKE is higher for the anisotropic mesh in both cases, even if the behavior of the curves for the two meshes remains approximately the same.

Regarding the integral length scales, the effect of the refined mesh is the opposite. Compared to the isotropic mesh, the plots of L_{ii} related to the anisotropic mesh are below. Figure 7.39a and Figure 7.39b show the streamwise evolution of L_{XX} for the two meshes, respectively, for $\alpha_{in} = 26.565^\circ$ and $\alpha_{in} = 63.435^\circ$. The curves related to L_{YY} and L_{ZZ} are not shown for redundancy reasons, because the effect of the mesh is the same as for L_{XX} . Differently from the Reynolds stress tensor, the shift downwards of the orange curves for the integral length scales does not depend by

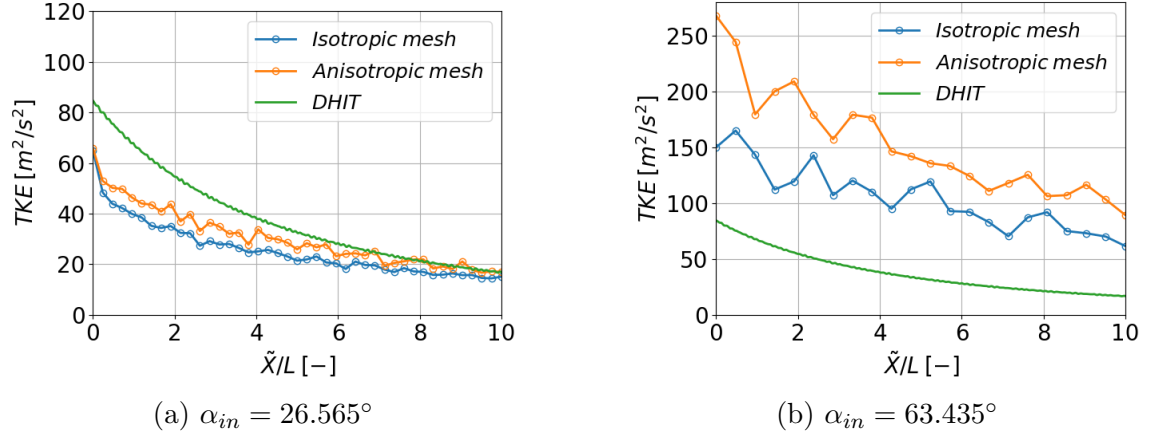


Figure 7.38: Streamwise evolution of the Turbulent Kinetic Energy for different meshes, using Mach total boundary conditions and with $\alpha_{in} \neq 0^\circ$

the amplitude of the injection angle. However, the decrease of the different scales due to the new mesh is not the same. In fact, the effect of the mesh on L_{YY} is less than the others, while for L_{XX} and L_{ZZ} the shift is of the same order of magnitude.

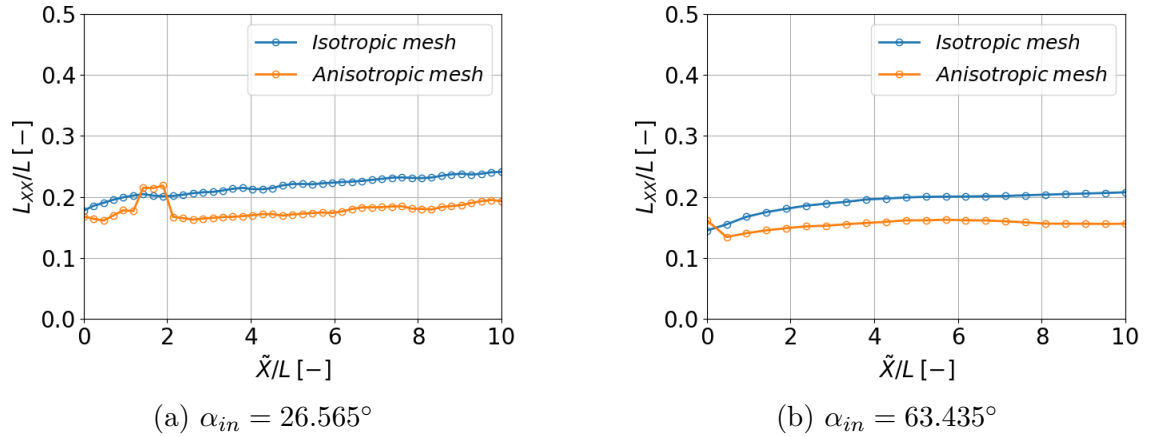


Figure 7.39: Streamwise evolution of L_{XX} for different different meshes, using Mach total boundary conditions and with $\alpha_{in} \neq 0^\circ$

Free stream conditions cases

The effect of the anisotropic mesh on simulations with Free stream boundary conditions and $\alpha \neq 0^\circ$ is the same as it had on simulations with $\alpha = 0^\circ$. Therefore, in this Subsection there are not graphs, as they are quite similar to those in the Subsection 7.2.5.

As already discussed, the new mesh leads to an increase of all the diagonal terms of the Reynolds stress tensor and, as a consequence, to an increase of the TKE. The magnitude of the increase is independent from the amplitude of the injection angle and is the same for all the diagonal terms, hence the turbulence is still isotropic. With respect to the integral length scales, they decrease by the same order of magnitude for both injection angles.

Chapter 8

Turbine simulations

Following the structure of Chapter 7 for the free domain, this chapter focuses on turbine simulations. Specifically, a high-speed low-pressure turbine cascade with high free stream turbulence. The linear cascade consists of SPLEEN blades, the geometrical features of which are presented in Section 3.1. The aim of this part of the study is to assess the effect of different boundary conditions on a practical test case with turbulence injection. In this master's thesis, static inlet boundary conditions have been employed to simulate the turbine cascade. The results will be compared with the numerical data obtained by [7], which used total conditions, and the experimental data collected by [1]. All these results refer to the same operating conditions: $M_{is,out} = 0.7$ and $Re_{is,out} = 70 \cdot 10^3$ (see Section 3.2). Although the use of static variables for imposing inlet boundary conditions in numerical simulations of turbines is not standard practice, they have been employed in this study to investigate the impact of this approach on the simulation results.

8.1 Computational setup

This section provides details of the turbine numerical simulation. Firstly, the computational domain geometry and mesh will be briefly discussed. Subsequently, the imposed boundary conditions, initial conditions, and the criterion used to determine the end of the numerical transient will be described. Finally, the locations within the domain from which the results presented in this study were extracted will be specified. Since the solver settings for the turbine simulation are identical to those employed for the free domain simulations, they will not be discussed further. However, it is worth noting that a time step of 10^{-7} s was used.

All solver settings presented in this section are directly applicable to those used in [7], with the exception of the inlet boundary conditions.

8.1.1 Computational domain and meshing

Figure 8.1 shows the turbine computational domain. The geometric features of the SPLEEN blade and the cascade have been presented in Subsection 3.1. The domain used for this study is the same used by [7]. Differently from previous simulations of the same blade [2, 6, 3], in this study and in [7] the inlet section is nearer to the LE of the blade ($0.75 \times c_{ax}$). Since in these cases the simulation occurs with

turbulence injection, the distance that turbulent structures must cover before reaching the blade has been shortened. However, if the inlet is too close to the blade, it may interfere with the boundary conditions. Nevertheless, this effect has been investigated by [7] and can be assumed to be negligible. Regarding the outlet section, its distance is kept unchanged respect to the previous simulations ($5 \times g$ downstream to the TE), in order to have enough space to analyze the wake and to prevent any non-physical interaction between the outlet and the blade due to reflection upstream of perturbations. In addition, a sponge layer is implemented. The pitchwise thickness is g , which is also equal to $8 \times L$. The spanwise thickness is equal to L , which is approximately 9% of c_{ax} . This thickness is also different from [2, 6, 3], in order to allow the turbulence injection through the precursor domain. Overall, 8 copies of the precursor domain are required to cover the entire inlet surface. As a result, the turbine simulation presents high correlation along the pitchwise direction. However, it should not compromise the reproduction of a physical turbulent flow behavior (see Chapter 6).

Since the flow is assumed to be quasi-two-dimensional, a small spanwise dimension relative to the domain can be employed to significantly reduce the computational cost, while still capturing the three-dimensional turbulent flow features. To verify the adequacy of the spanwise thickness for the resolution of turbulent structures, the integral length scales computed along the spanwise direction will be discussed in Subsection 8.2.6.

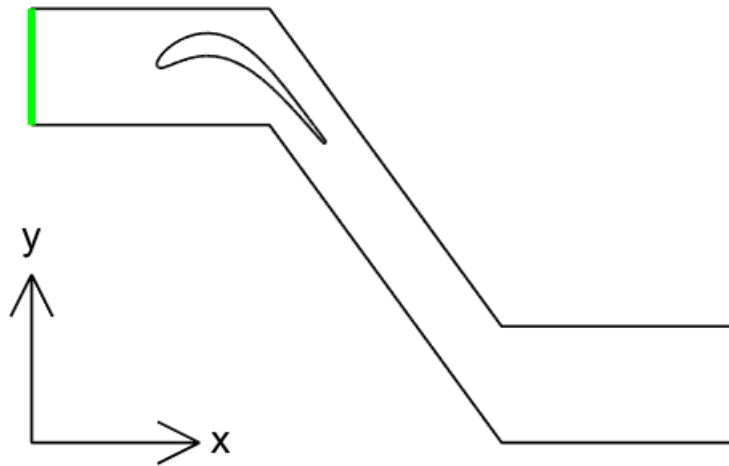


Figure 8.1: Turbine domain with inlet shown in green (left) and outlet shown in red (right), 2-dimensional view

Figure 8.2 shows the mesh of the turbine domain generated by [7] and used in this study. As for the free domain simulations, the mesh has been generated using the GMSH software; however, in this case the mesh is unstructured. Several refinements regions are present in the domain: the complete inlet region, the blade channel and the wake region. The element size in the inlet region is set to 0.5% of c , matching the spatial resolution of the precursor domain, to optimally reproduce injected turbulence. In addition, a 0.79 mm thick O-type structured mesh has been used around the blade, with a second-order accuracy of the mesh edges. Specific refinements regions have been introduced near the LE and the TE. The highest

level of refinement can be found in elements in direct contact with the blade surface, which have a size of 0.076% of c , while the coarsest level in the mesh is near the outlet, with an element size equal to 7.6% of c . Regarding the spanwise resolution, the domain has been divided into 34 equivalent layers, corresponding to 0.23% of c for each element. The high spanwise resolution is also necessary to reproduce the three-dimensional turbulent structures in the domain.

The overall number of elements is 2 020 042. Further details about the elements size and the mesh quality can be found in [7].

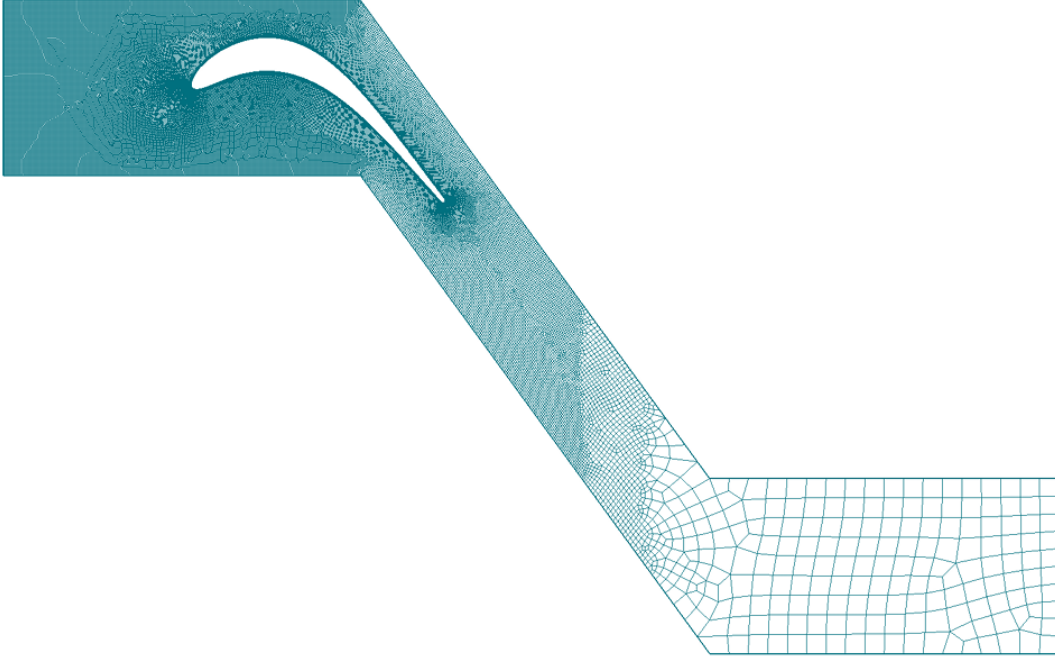


Figure 8.2: Mesh of the turbine domain, 2-dimensional view (taken from [7])

To ensure that the mesh adequately resolves the flow features near the blade wall, it is necessary to verify that the centroid of the elements closest to the wall lies within the pure viscous sublayer, i.e., $n^+ < 5$ (see Subsection 2.3.3). Figure 8.3 shows the wall coordinates of the elements in contact with the blade in the normal and tangential directions, respectively, where the solid line represents the time-averaged value and the dashed lines represent the extremes of the instantaneous values. The negative part of the abscissa in both graphs refers to the PS, while the positive part refers to the SS. Given that the polynomial reconstruction of the DGM is also of order 3 in the SPLEEN simulations, it is sufficient to verify that $n^+ < 15$. Figure 8.3a shows that this condition is satisfied around the entire blade at all times. The values of the wall coordinate in the tangential direction s^+ are higher due to the larger size of the elements near the wall in this direction (see Figure 8.3b). Nevertheless, the values fall within a range that can be considered acceptable for the wall resolution.

Following a similar approach to that outlined in Subsection 7.1.1 for the free domain, the turbine domain mesh was divided into 512 partitions, with 4 CPUs

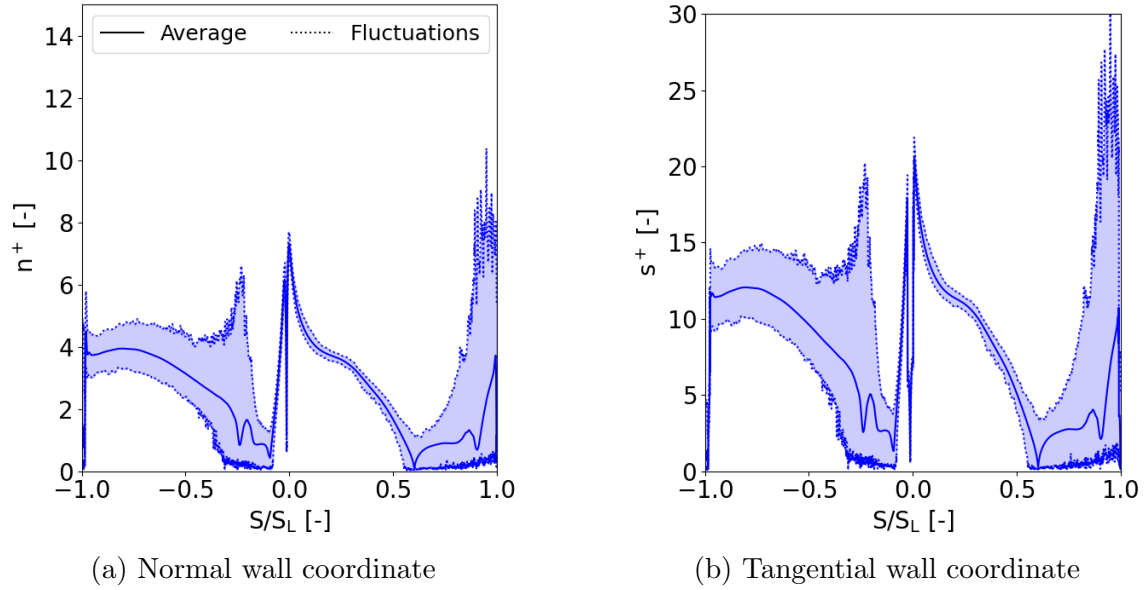


Figure 8.3: Time-averaged and extremes instantaneous values of the wall coordinates associated to the near-wall elements

assigned to each partition, requiring a total of 16 nodes on the Lucia cluster to run the simulation.

8.1.2 Boundary conditions, initial conditions and convergence

To simulate the flow in the turbine domain, several boundary conditions have been imposed. Starting from inlet, free stream boundary conditions type is imposed. Differently, the results of [7] have been obtained imposing Mach total boundary conditions type at the inlet. A summary of the inlet parameters used in the two cases is shown in Table 8.1. In both cases, the same static pressure is imposed at the outlet: $p_{out} = 7771.164$ Pa.

Mach total conditions			Free stream conditions		
Quantity	Unit	Value	Quantity	Unit	Value
P_{in}^0	[Pa]	10779.39	P_{in}	[Pa]	9535.7
T_{in}^0	[K]	300	T_{in}	[K]	289.674
α_{in}	[°]	36.3	\bar{U}_{in}	[m/s]	[116.1 85.28 0]

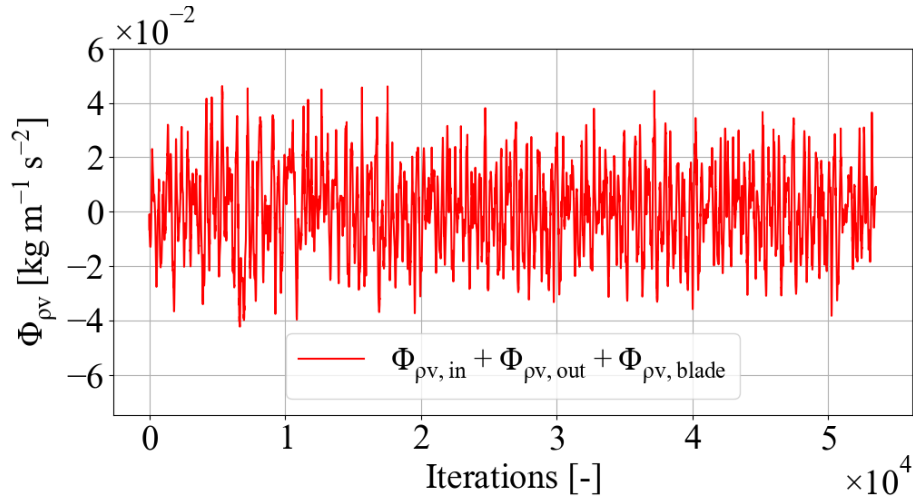
Table 8.1: Inlet boundary conditions parameters for the turbine simulation

A no-slip condition is imposed on the blade surface, meaning that the fluid velocity at the wall is zero. Additionally, the blade is assumed to be adiabatic, resulting in zero heat flux across the blade surface.

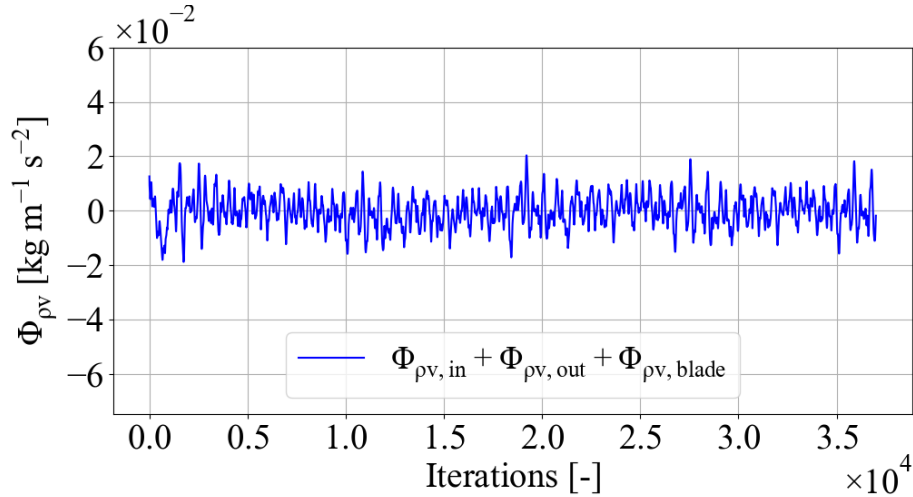
Periodicity is imposed in both the pitchwise and spanwise directions. The first condition allows to simulate a linear cascade composed by an infinite number of blade, while the second condition allows to simulate an infinite span blade. Due to the latter condition, blade tip and end wall effects are not considered in the frame

of this study.

The flow field has been initialized using a statistically converged solution computed by [7]. Since the mesh and the operating conditions of the turbine simulation presented in this study are the same of [7], convergence to a statistically stable state was achieved relatively short time despite the high number of DOF. Following the approach adopted for the free domain, the end of the transient of the turbine simulation was determined by monitoring the convective density flux at the inlet and outlet. Given the unsteady nature of turbulence, mass conservation within the domain is not instantaneously satisfied but can be verified by time-averaging. The transient phase was considered complete after 37,000 time steps, corresponding to slightly more than $2 t_c$.



(a) Mach total inlet boundary conditions



(b) Free stream inlet boundary conditions

Figure 8.4: Time evolution of the pitchwise component of the momentum fluxes; data are monitored during the numerical transient and extracted on the inlet, the outlet and the blade, for both total (**top**) and static (**bottom**) inlet boundary conditions [total case taken from 7]

The end of the transient can also be assessed by monitoring the momentum fluxes on the boundaries. Figure 8.4 shows the time evolution of the momentum fluxes along the pitchwise direction, considering the contribution of the inlet, the outlet and the blade. Differently from the convective fluxes of density, the momentum fluxes on the blade are not zero, thus they must be taken into account. The upper plot is related to the simulation with total boundary conditions at the inlet, while the lower one is related to the simulation with static conditions. In both cases, the conservation of momentum is not verified instantaneously due to the unsteady nature of turbulence; however, it is verified on average over the time. The fluxes related to the total conditions case are shown in order to evaluate their stronger oscillations. Although the injected turbulence is the same, in the total conditions case it leads to higher fluctuation.

8.1.3 Data extraction

Similarly to the free domain, the data extraction in the turbine simulation has been carried out in specific locations and using co-processing, in order to mitigate the storage resources required and the computational cost of post-processing.

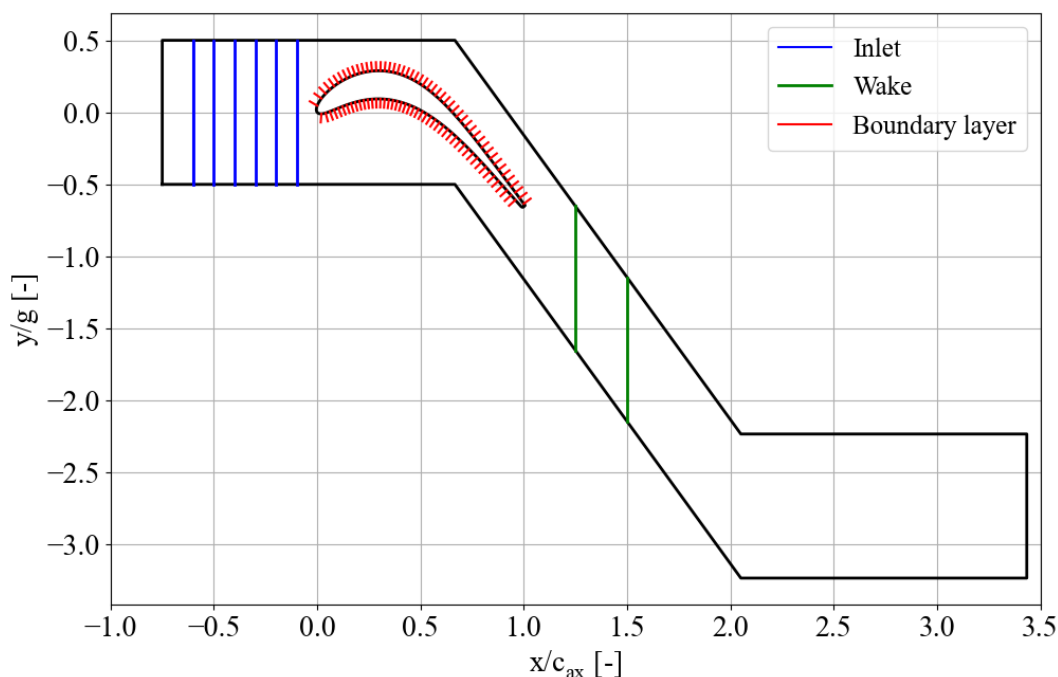


Figure 8.5: Probes layout in the turbine domain

Figure 8.5 shows the distribution of the probes used to collect data in the turbine domain. Firstly, a set of probes distributed on 6 equidistant planes is employed in the inlet region, between $0.6 \times c_{ax}$ and $0.1 \times c_{ax}$ upstream to the LE of the blade. These data are used to evaluate the isotropy and the TKE of the turbulence reaching the blade. Then, a probe set is also located near the blade to evaluate the boundary layer evolution on PS and on the SS. This information is analyzed in combination with data extracted directly from the blade surface, to assess the presence of separation bubbles and transition in the BL. Lastly, a set of probes distributed on two planes

located respectively $0.25 \times c_{ax}$ and $0.5 \times c_{ax}$ downstream to the TE of the blade is used to monitor the wake region. These planes correspond to the plane 05 and plane 06 used in the VKI S1/C wind tunnel (Figure 4.2). All probe sets presented in Figure 8.5 are extruded along the spanwise direction across the entire blade span. In addition, some instantaneous fields are extracted from a single spanwise plane to generally evaluate the flow features.

8.2 Results and discussion

This section will present and discuss the results of the numerical simulation for the turbine. The outcomes of the study is categorized as follows:

1. turbulent energy density spectrum and streamwise evolution of Reynolds stress tensor, TKE, and integral length scales in the inlet turbulent flow;
2. instantaneous field in a single spanwise plane of the local Mach number, vorticity, numerical Schlieren, and entropy generation;
3. time and spanwise average of the blade loading;
4. time and spanwise average of the skin friction coefficient on the wall blade, and its temporal evolution;
5. velocity profiles and TKE in the BL, with related integral parameters;
6. pitchwise distribution of total pressure deflection, total temperature deflection, Reynolds stress tensor and integral length scales in the wake, with deviation angle and turbulent energy density spectrum.

8.2.1 Inlet

Figure 8.6 shows the streamwise evolution of Reynolds stresses in the inlet region for the two types of inlet boundary conditions. The data related to this figure and all the others present in this subsection are extracted through the inlet probe set (Figure 8.5). The main differences between the two cases are the diagonal terms of the Reynolds stress tensor. More specifically, the turbulence injected with static conditions is much more isotropic. This result is perfectly consistent with what has been observed in the free domain: in the total conditions case the $\overline{u'u'}$ is lower, while $\overline{v'v'}$ is higher due to $\alpha_{in} \neq 0^\circ$. The off-diagonal cross-product terms are near zero for both cases, with a small difference in $\overline{u'v'}$ that is negative for the total conditions case, which also indicates turbulence anisotropy.

Figure 8.7 shows the TKE evolution in the inlet region with total and static boundary conditions. The two curves are compared to the TKE evolution predicted with the DHIT in the precursor domain. Similarly to the free domain, the TKE at the inlet of the main domain is lower than the predicted value. Hence, some turbulence kinetic energy is lost with the injection process, independently from the type of boundary conditions. Furthermore, the curves related to the total conditions case is higher due to the $\alpha_{in} \neq 0^\circ$. Overall, the turbulent flow reaching the LE of the blade in the static conditions case match better the expected values.

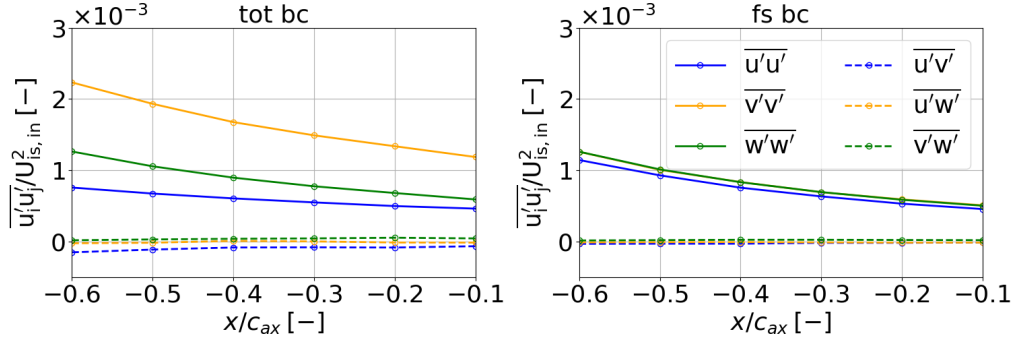


Figure 8.6: Streamwise evolution of the Reynolds stresses in the inlet region, averaged over time and along pitchwise and spanwise directions, with total (**left**) and static (**right**) inlet boundary conditions (total case reproduced from [7])

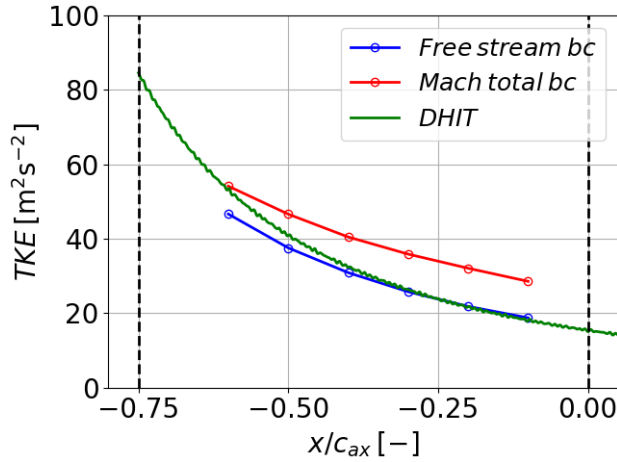


Figure 8.7: Streamwise evolution of the TKE in the inlet region, averaged over time and along pitchwise and spanwise directions, with total and static inlet boundary conditions; the curves are compared to the TKE evolution predicted using the DHIT (total case reproduced from [7])

Figure 8.8 shows the streamwise evolution of the integral length scales for the three components of velocity fluctuation, computed along the spanwise direction. The curves related to L_{XZ} and L_{ZZ} are quite similar for the two numerical cases, while a large difference can be observed for L_{YZ} . In the Free stream case that scale is close to L_{XZ} , while the scale is higher and close to L_{ZZ} for the Mach total case. In the case of homogeneous and isotropic turbulence, the integral length scale calculated along a direction for the fluctuation of the velocity component in the same direction is typically about twice the integral length scales calculated along the same direction but related to the fluctuations of the velocity components in the other directions:

$$L_{XZ} \sim L_{YZ} \sim 2L_{ZZ}. \quad (8.1)$$

The scales reproduced by the Free stream case are much closer to this condition, so this once again confirms that it is much closer to reproducing homogeneous and isotropic turbulence. Overall, a slight increase of all scales along the streamwise direction can be observed for both cases.

Figure 8.9 shows the energy density spectrum extracted at $0.5 \times c_{ax}$ upstream of the blade LE, for the static and total conditions cases. A line with slope $-5/3$

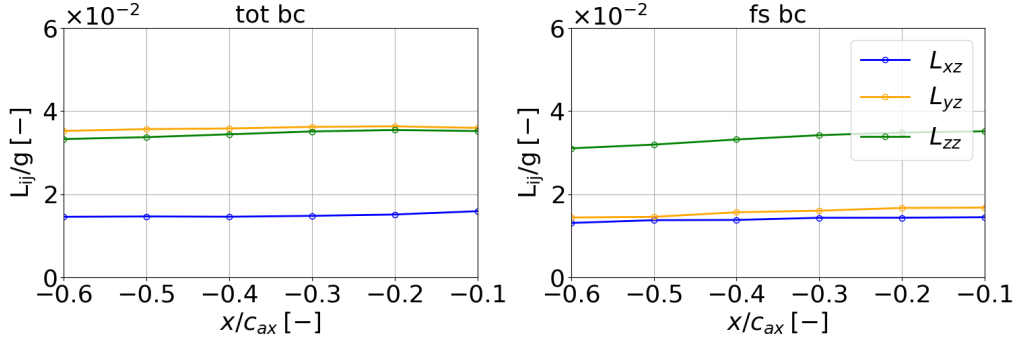


Figure 8.8: Streamwise evolution of the integral length scales in the inlet region related to the three components of velocity fluctuation, averaged over time and integrated along the spanwise direction, with total (**left**) and static (**right**) inlet boundary conditions (total case reproduced from [7])

is plotted in the inertial subrange as a reference of the spectrum function (Equation 2.39). The curves related to the energy distribution of the two cases are quite close, and also similar to the typical energy spectrum for homogeneous and isotropic turbulence (Figure 2.1). However, the energy spectral content is slightly higher for the free stream case.

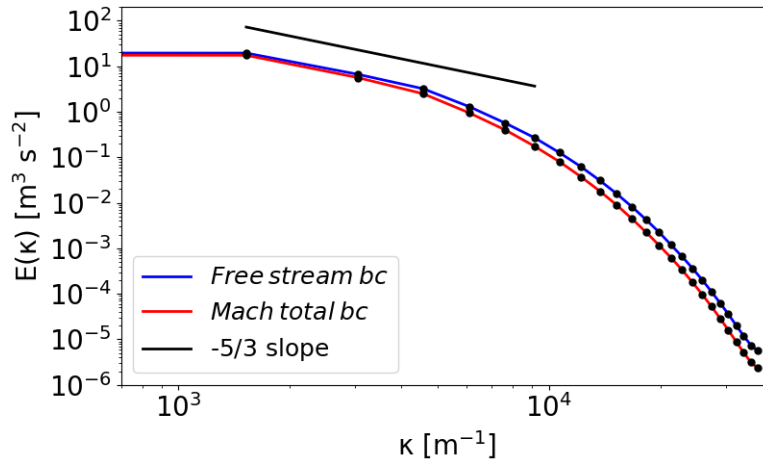


Figure 8.9: Energy density spectrum averaged over time and along pitchwise and spanwise directions, extracted at $0.5 \times c_{ax}$ upstream to the LE of the blade, for total and static inlet boundary conditions (total case reproduced from [7])

8.2.2 Fields

Figure 8.10 shows the instantaneous field of the local Mach number M in a spanwise plane. The M field, along with the other fields present in this subsection, consists of multiple SPLEEN blades arranged side-by-side in the pitchwise direction to enhance the visualization of the flow through the linear cascade. The general behavior of the flow is the same for both inlet conditions cases. The flow decelerates on the PS near the LE, where a short separation bubble can be observed due to the adverse pressure gradient. Further downstream, the flow accelerates and reattaches to the wall shortly after. Regarding the SS, the flow accelerates in the front part

and separates in the rear part of the blade where the flow decelerates. Nevertheless, the flow reattaches before reaching the TE. As a result, the wake width near the blade is equal to the blade thickness at the TE (t). Furthermore, the low-velocity region within the wake, which exhibits a highly unsteady nature, can be observed.

Since 8 precursor domains are required to cover the entire inlet section of each blade domain, strong periodicity in the flow structure along the pitchwise direction is observed. However, the high correlation along the pitchwise direction should not compromise the reproduction of a physical turbulent flow behavior (see Chapter 6).

One aspect that differs between the two simulations concerns the local Mach number gradient observed within the blade channel. Specifically, in the case of static inlet conditions, the Mach field in this region is significantly smoother compared to the case with total inlet conditions. This is probably caused by the higher level of disturbances present in the latter case.

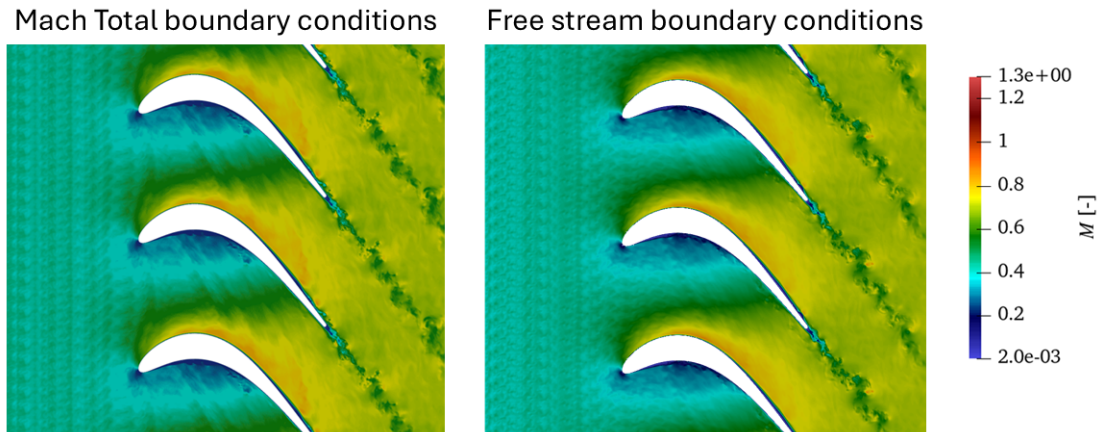


Figure 8.10: Instantaneous field of the Mach number extracted from the spanwise plane at $z = 0$, with total (**left**) and static (**right**) inlet boundary conditions (total case taken from [7])

Figure 8.11 shows the instantaneous field of the vorticity magnitude ω in a spanwise plane. Similar to what was observed for the Mach number field, there is a strong periodicity of the turbulent structures along the pitchwise direction. Also in this case, the general vorticity distribution for the two different types of inlet conditions exhibits the same characteristics. Vorticity production is concentrated in the flow regions near the wall and in the wake. In particular, this visualization highlights the separation bubbles. Indeed, high levels of vorticity are noticeable at the free shear layer at the interface between the separated flow and the bubble, i.e., on the PS near the LE and on the SS near the TE. Nevertheless, the highest levels of vorticity are located in the wake, especially in the portion closest to the blade's trailing edge.

Another aspect highlighted by this field is the flow acceleration in the blade channel. Indeed, the turbulent structures are deformed and elongated along the flow direction in this region. Regarding this phenomenon, it is worth specifying that the difference found between the two cases for the vorticity distribution in the blade channel can be attributed to the different time instant at which the corresponding

fields were extracted. Although the same turbulence structures are injected in both simulations, their position in the cascade is different due to the different time they have had to travel downstream.

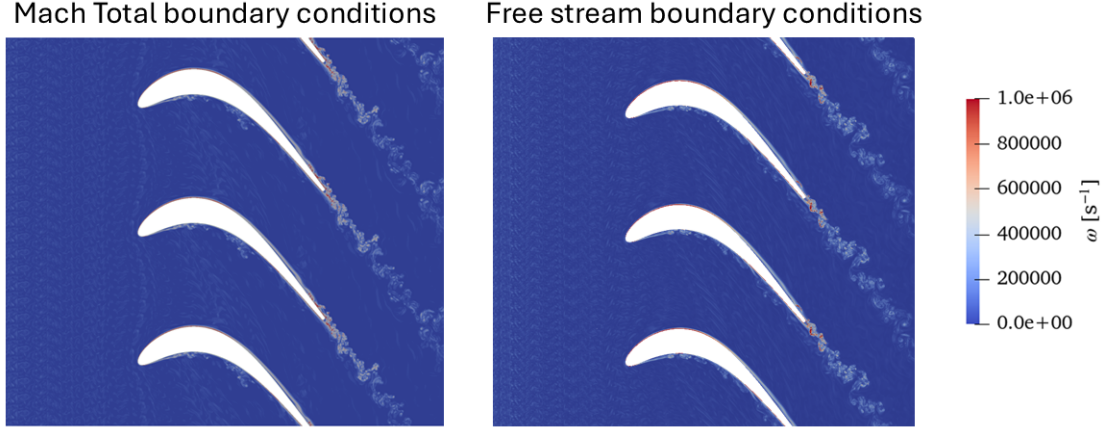


Figure 8.11: Instantaneous field of the vorticity magnitude extracted from the span-wise plane at $z = 0$, with total (**left**) and static (**right**) inlet boundary conditions (total case taken from [7])

Figure 8.12 shows the instantaneous field of the local normalized density gradient ($\nabla\rho/\rho$), also known as numerical Schlieren. Similar to previous fields, a strong pitchwise periodicity is present in this case, due to the density variations caused by the turbulent structures. The numerical Schlieren is displayed using a logarithmic scale. The highest density variations are observed near the blade wall and in the wake, while smaller variations attributable to acoustic waves are present in the rest of the domain. Since the flow is subsonic, these waves can travel upstream. Indeed, perturbations travel from the wake to the blade. Furthermore, "V" shape structures can be found near the rear part of the SS, where the waves reflect on the blade wall.

The main difference between the numerical Schlieren extracted from the cases lies in the intensity of the acoustic waves. In fact, the density variations in the case of total conditions are more marked. The cause of this phenomenon can be attributed to the compensation procedure implemented within the turbulence injection. The total pressure and total temperature imposed at the inlet for the Mach total simulation are evaluated on the sum of convective inlet velocity and turbulent velocity fluctuations. As a consequence, a compensation is necessary to obtain the desired total value after imposing the velocity fluctuation from the precursor domain. This procedure could be the cause of such acoustic disturbance in the numerical simulation.

Figure 8.13 shows the instantaneous field of the entropy generation (Δs). As discussed in Section 3.4, Δs can be used to estimate the amount of losses in the cascade. The entropy distribution in the two cases is very similar. Most of the losses are generated on the rear part of the SS and in the base flow, by the viscous effects in the mixing of the edges of the separation bubble and the wake. Indeed, a slight Δs level is also observed on the front part of the PS, where a short separation

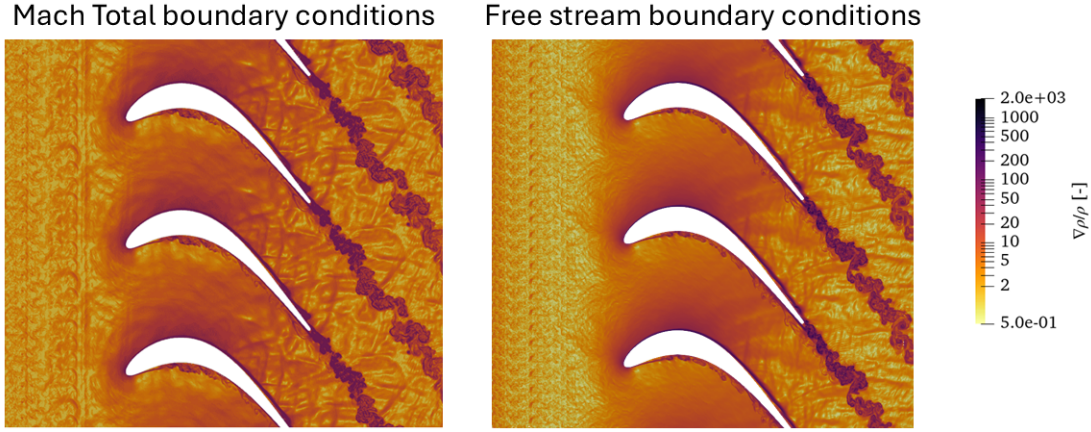


Figure 8.12: Instantaneous field of the normalized density gradient (numerical Schlieren) extracted from the spanwise plane at $z = 0$, with total (**left**) and static (**right**) inlet boundary conditions (total case taken from [7])

bubble occurs. The entropy generated by the free stream turbulence is negligible compared to the other effects, and therefore is not visible.

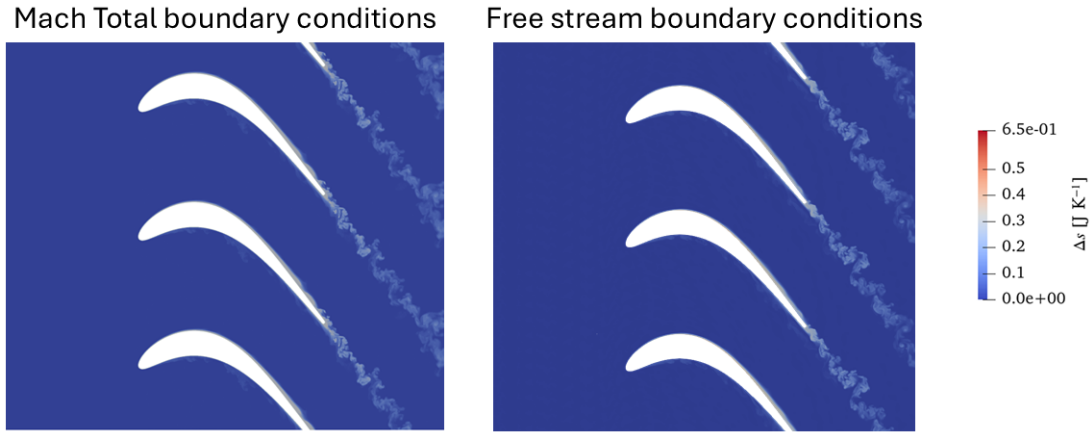


Figure 8.13: Instantaneous field of the entropy generation extracted from the spanwise plane at $z = 0$, with total (**left**) and static (**right**) inlet boundary conditions (total case taken from [7])

8.2.3 Blade loading

Figure 8.14 shows the distribution of the isentropic Mach number on the blade (M_{is}) for the two inlet boundary conditions cases and for the experimental case. The upper curves are related to the SS, while the lower ones are related to the PS. The x -axis refers to the streamwise location which is made dimensionless through c_{ax} . The M_{is} distribution is directly correlated to the static pressure acting on the wall (see Equation 3.1), thus it can be used to evaluate the normal component of the forces exchanged between the flow and the blade surface.

The behavior of the curves related to the different inlet conditions is similar for most of the blade surface, except in the front part of the PS and in the rear

part of the SS. More specifically, the discrepancy is observed near the regions where the separated flow reattaches to the wall. Apparently, the case with static inlet conditions tends to reattach further downstream, both for the separation bubble on the PS and for the one on the SS. The cause can be attributed to the different TKE injected for the two cases. Indeed, the higher turbulent intensity associated with the total inlet conditions case causes the transition of the boundary layer further upstream, thus leading to an earlier flow reattachment.

In the remaining portions of the blade, the two curves are overlapped, except for a discrepancy in the rear part of the SS, where the M_{is} of the total conditions case is slightly higher.

Overall, both numerical simulations reproduce the experimental measurements quite well. However, the simulation with static inlet conditions deviates slightly from the experimental flow reattachment on the PS. On the other hand, it has a better agreement near the reattachment on the SS.

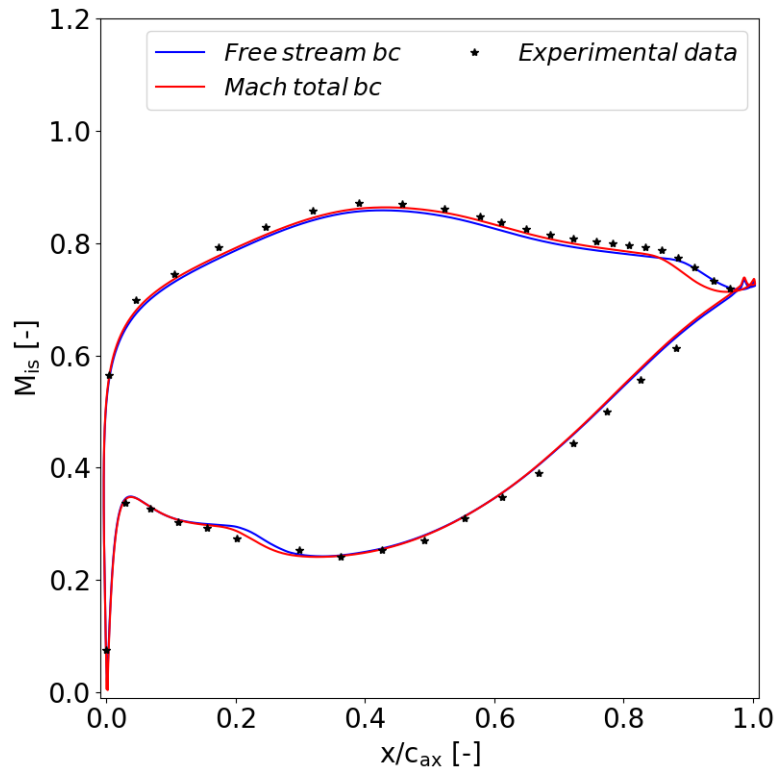


Figure 8.14: Time and spanwise average of the isentropic Mach number on the blade, with total and static inlet boundary conditions cases (total case taken from [7]) compared to experimental data [1]

8.2.4 Skin friction

Figure 8.15 shows the distribution of the skin friction coefficient c_f (see Equation 2.49) around the blade, related to the wall shear stress τ_w for the two numerical cases. In addition, the quasi-wall shear stress τ_q measured experimentally is plotted on a separated axis. The latter is reported to make a comparison on the general

trend and not on the absolute value. Similarly to Figure 8.3, the solid lines represent the time-averaged values and the dashed lines represent the extremes of the instantaneous values. In addition, the negative part of the abscissa refers to the PS, while the positive part refers to the SS.

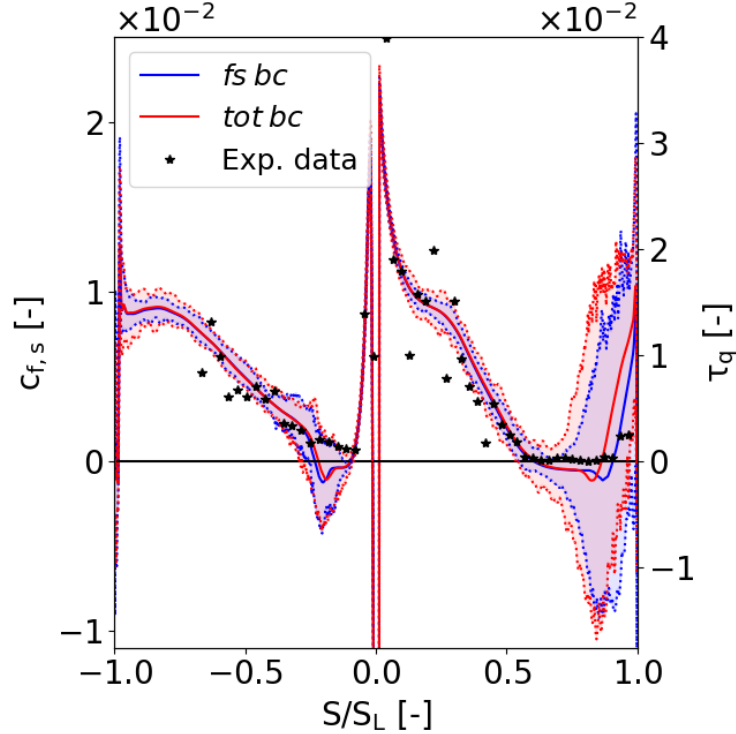
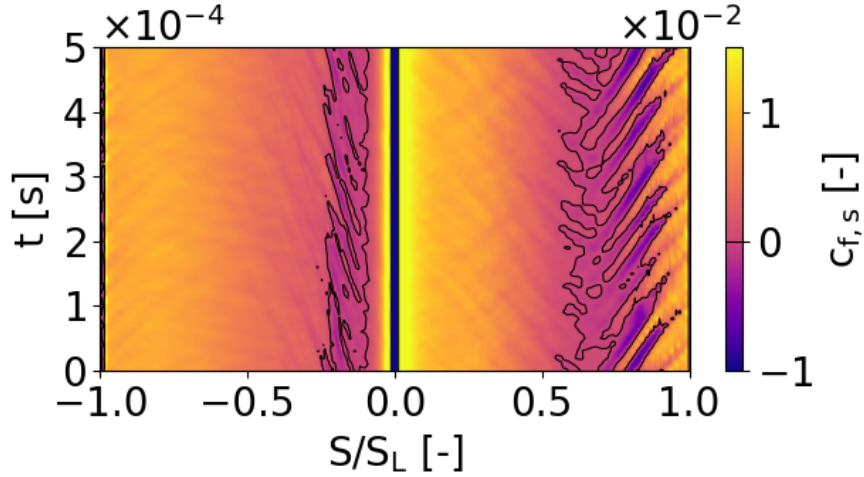


Figure 8.15: Time and spanwise average of the skin friction coefficient on the blade, with total and static inlet boundary conditions cases [total case taken from 7] compared to experimental data [1]

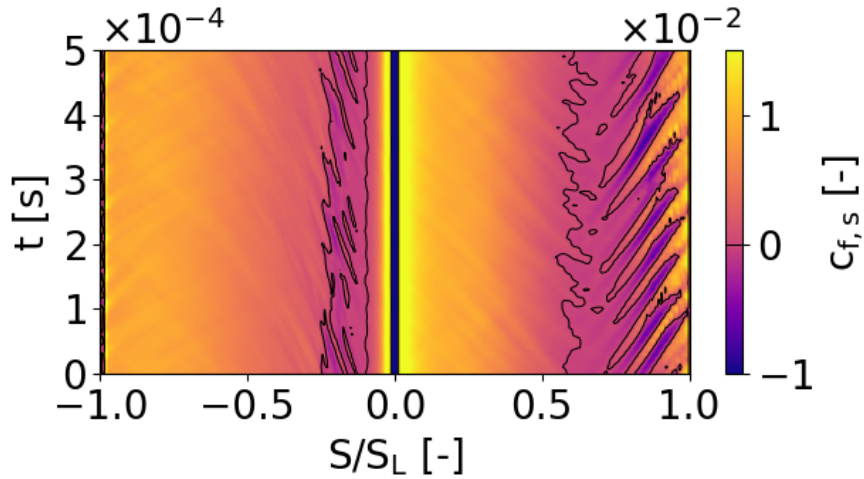
The general behavior of the two curves is the same. On the SS, c_f is large near the LE, then it decreases to 0 at the separation point (see Equation 2.53). A long separation bubble occurs in the rear part (where $c_f < 0$), then the flow reattaches near the TE and the c_f rapidly increases. The large fluctuations observed in the rear part are linked to the transition of the BL from laminar to turbulent regime. As predicted in the previous sections, the onset of turbulence in the static conditions case is further downstream because of the lower TKE injected. As a consequence, reattachment is also delayed downstream, leading to a better match with the experimental results.

Regarding the PS, large c_f is observed near the LE, then it rapidly decreases to 0 at the separation point. The increase in fluctuations indicates the onset of turbulence in the separated flow, which allows the reattachment of the BL and leads to a short bubble formation. Due to the lower TKE in the static conditions case, the reattachment occurs slightly downstream. In the remaining portion of the PS, the c_f gradually increases. Here, the decreasing fluctuations indicate the relaminarization of the BL, caused by a favorable pressure gradient.

Figure 8.16 shows the temporal evolution of the spanwise averaged c_f on the blade for the two numerical cases, over a time span of $5 \cdot 10^{-4}$ s. Black curves indicate where $c_f = 0$, thus allowing to assess the evolution of the separation bubbles over



(a) Mach total inlet boundary conditions



(b) Free stream inlet boundary conditions

Figure 8.16: Time evolution of the spanwise averaged skin friction coefficient on the blade, with total (**top**) and static (**bottom**) inlet boundary conditions (total case taken from [7])

time.

The long separation bubble near the TE on the SS exhibits a strong oscillatory behavior caused by periodic bubble bursting. However, the separated flow manages to reattach before the TE in each time step, and an open separation never occurs. Again, it is possible to observe the longer bubble for the static conditions case on average over time.

Regarding the PS, the short bubble occurs near the LE. Unlike the long bubble, the amplitude of fluctuations in this case is much smaller. Comparing the two numerical cases, it is again possible to observe the slight difference in bubble size on average over time.

Lastly, some blurred lines consistent with the shape of bubbles are present on the rear part of the PS and on the front part of the SS. In the former case, the lines indicate the vortices generated in the short bubble that travel downstream. In the latter, they indicate information traveling upstream from the long bubble.

Furthermore, the case with total conditions exhibits more blurred lines with more directions, probably due to the greater acoustic disturbances present in this case (Figure 8.12).

8.2.5 Boundary layer

Figure 8.17 shows some tangential velocity profiles for the two numerical cases. The velocity data are extracted using the boundary layer probe set (Figure 8.5). The tangential velocity is made dimensionless using the isentropic output velocity ($u/U_{is,out}$). The negative part of the abscissa refers to the PS, while the positive part refers to the SS.

The plots give the same information of the previous sections. On the PS, the flow separation occurs near the LE, then it rapidly reattaches and accelerates moving towards the TE. Regarding the SS, the flow accelerates in the front part of the blade and separates in the rear part, but it manages to reattach before the TE. The curves for the two cases overlap over most of the domain, except for the separation bubbles. In the static inlet conditions case, the flow reattaches further downstream, with a slight discrepancy in velocity profiles on the PS and a more noticeable one on the SS.

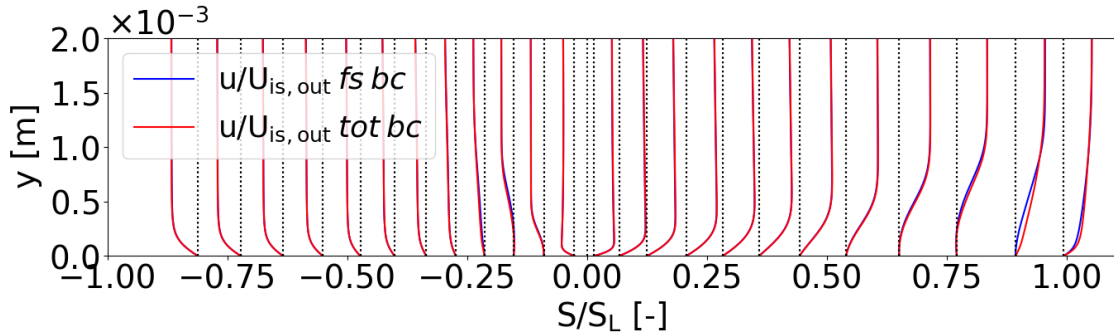
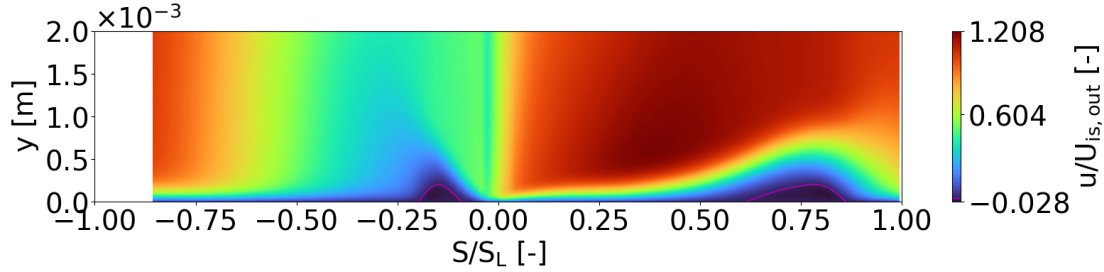


Figure 8.17: Time and spanwise average of tangential velocity profiles in the boundary layer, with total and static inlet boundary conditions (total case taken from [7])

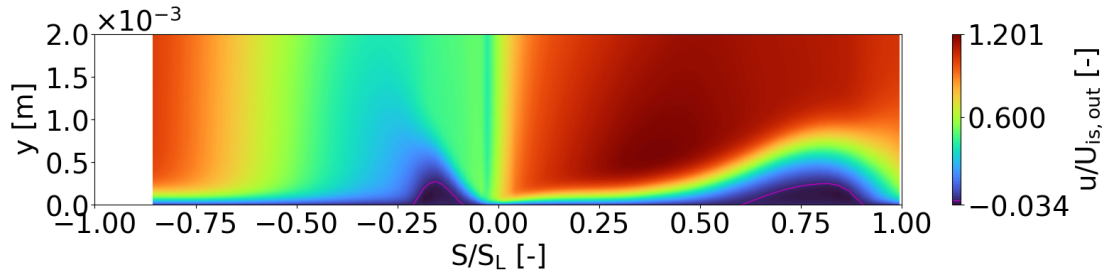
Figure 8.18 shows the dimensionless tangential velocity field in the boundary layer. The information contained in this field is similar to that reported in Figure 8.17, but in this case the separation bubbles are highlighted. The magenta lines represent the union of the points where the tangential velocity is zero. Since the field refers only to the tangential component of velocity, the highlighted contour does not exactly represent the average profile of the separation bubbles. Nevertheless, it can be considered representative of the phenomenon and therefore an approximation of the real shape. On the other hand, the normal component of velocity is zero on the wall, thus the average separation and reattachment points correspond to the actual ones.

Looking at the figure, it is evident the difference for the bubbles length and shape on the two sides of the blade. The flow on the PS separates and reattaches quite rapidly. Differently, the bubble on the SS has an elongated front part and a shorter rear part. The former is due to the strong adverse pressure gradient encountered by the boundary layer, while the latter is due to the turbulent reattachment.

In addition, a slight difference can be observed between the two numerical simulations. Not only the bubbles of the simulation with static inlet conditions are slightly longer, but they are also higher in a certain sense. Since the flow reattaches further downstream, the free shear layer moves further away from the wall and the flow displacement induced by the presence of the separation bubbles is greater.



(a) Mach total inlet boundary conditions



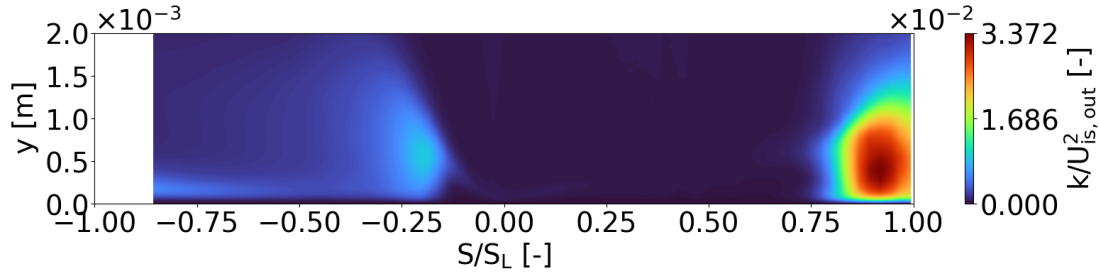
(b) Free stream inlet boundary conditions

Figure 8.18: Time and spanwise average of the tangential velocity in the boundary layer, with total (**top**) and static (**bottom**) inlet boundary conditions (total case taken from [7])

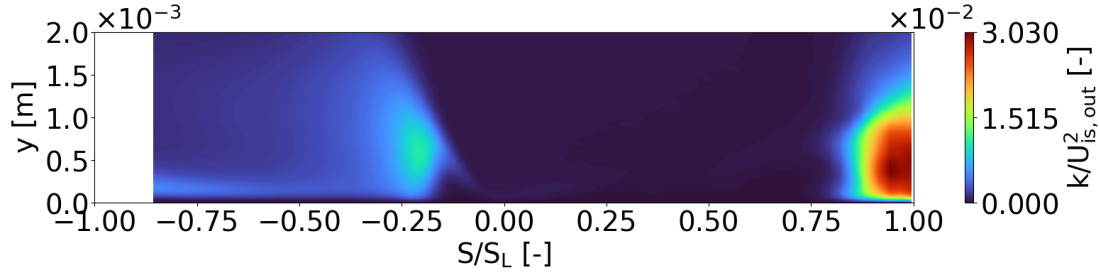
Figure 8.19 shows the TKE distribution in the boundary layer. The field highlights the turbulent fluctuations generated by separated flow transition (see Subsection 2.3.1). Indeed, high TKE is concentrated in the separated flow regions. On the PS, the free shear layer produces high velocity fluctuations, which rapidly propagate into the boundary layer, causing its transition and thus the reattachment of the flow to the wall. In the rear part of the PS, the favorable pressure gradient leads to relaminarization and gradual decrease in TKE. Conversely, the SS is characterized by low velocity fluctuations up to the region near the TE, where the separated flow transition leads to high levels of TKE. In the case with static inlet conditions, the concentration of TKE is visibly further downstream, denoting the delayed transition of the boundary layer.

Figure 8.20 shows the integral quantities on both PS and SS for the two numerical cases. The quantities presented are the displacement thickness δ^* , the momentum thickness θ and the shape factor H (see Section 2.3). The horizontal dashed line in $H = 2$ represents the boundary between laminar and turbulent regimes.

Overall, the curves behavior is the same for both simulations. On the PS δ^* increase rapidly near the LE due to the separation. θ also increases: at first the slope is low, then the slope increases due to the increasing momentum exchange caused by



(a) Mach total inlet boundary conditions



(b) Free stream inlet boundary conditions

Figure 8.19: Time and spanwise average of the TKE distribution in the boundary layer, with total (**top**) and static (**bottom**) inlet boundary conditions (total case taken from [7])

the transition of the boundary layer. At the same location, H drops sharply below 2, indicating the transition from laminar to turbulent regime. Just downstream the transition, the flow reattaches and δ^* decreases. θ decreases with reattachment as well, and also decreases due to the gradual transition from turbulent to laminar regime. H tends to increase after the reattachment, confirming the relaminarization caused by the favorable pressure gradient on the rear part of the PS.

On the SS, the separation occurs on the rear part of the blade, where δ^* rapidly increases. H firstly increases due to the laminar separation, and then it starts to decrease, indicating the transition of the BL. Subsequently, the higher momentum exchange allows the reattachment before the TE and thus δ^* decreases. θ gradually increases in the front part, while a high slope is observable near the TE due to the transition.

Figure 8.21 shows the same information of Figure 8.20, with a focus on the differences between the two numerical cases. In the static inlet conditions case, δ^* exhibits higher values in the separation region, with the maximum values further downstream. Indeed, the flow displacement induced by the separation is stronger compared to the total inlet conditions case; moreover, the reattachment of the flow occurs further downstream. Regarding θ , the curve related to the static conditions case is slightly higher in the short bubble on the PS, while it is slightly lower in the long one on the SS. Lastly, the H curves present the same features discussed for δ^* , i.e., higher values and further downstream maximum values for the static conditions case in the separation regions. Indeed, the transition is delayed due to the lower TKE injected.

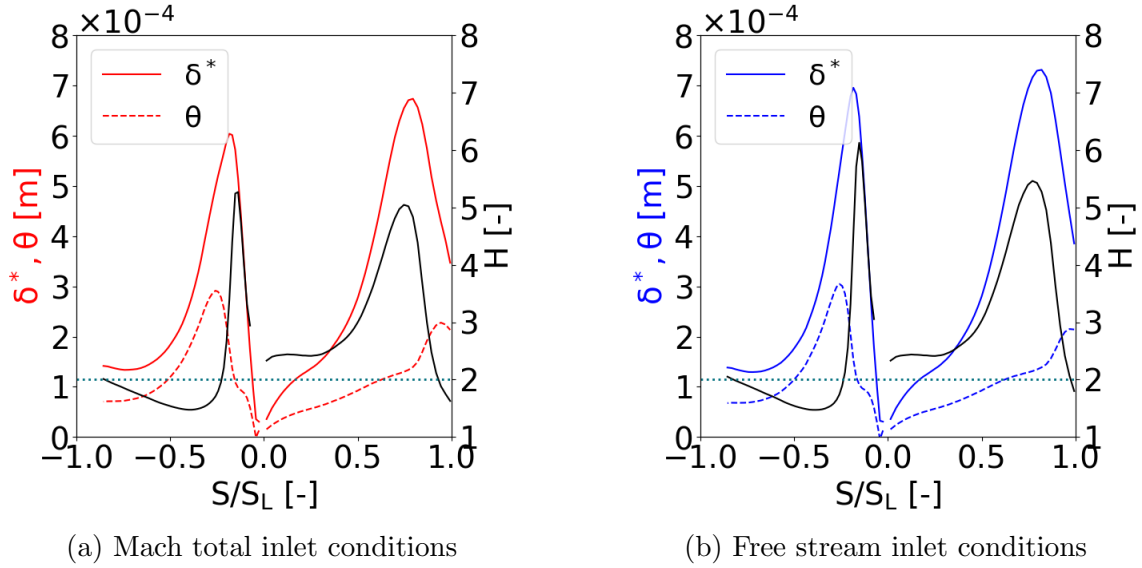


Figure 8.20: Time and spanwise average of the boundary layer integral parameters, with total (**left**) and static (**right**) inlet boundary conditions (total case taken from [7])

8.2.6 Wake

Figure 8.22 shows the normalized distribution of total pressure loss in the wake. This parameter can be used to evaluate the losses in the wake (see Section 3.4). The data of plane 05 and plane 06 are extracted using probe sets located downstream the TE at $0.25 \times c_{ax}$ and $0.5 \times c_{ax}$ respectively (Figure 8.5). All the plots discussed in this subsection refer to the same locations (plane 05 and 06). Experimental measurements are available only for plane 06.

The curves of plane 05 are more elongated compared to plane 06. This behavior is related to the total pressure decay, which affects both numerical simulations equally. The maximum total pressure loss decreases, while the width of the curve tends to increase due to the wake, which involves a larger portion of flow while moving downstream.

Furthermore, for the same location, the shape of the curve changes slightly between the two numerical cases. In fact, the simulation with static inlet conditions shows lower maximum values of total pressure loss and greater widths. The resulting distribution leads to a better agreement with the experimental results, especially for negative values of the pitchwise coordinate. The numerical simulation predicts the peak of the curve very well, even though the width is still smaller.

Figure 8.23 shows the total temperature distribution in the wake. Overall, the phenomena observed are similar to those discussed on Figure 8.22. Traveling from plane 05 to plane 06, T^0 peaks decrease and its curve becomes wider. Furthermore, the case with static conditions exhibits lower peaks and wider curves on both planes compared to the total conditions case.

Figure 8.24 shows the flow angle distribution in the wake. The thick black line correspond to the metal angle at the TE: $\alpha'_2 = 53.8^\circ$ (see Section 3.1).

The shape of the curves is closely linked to the chaotic behavior of the von

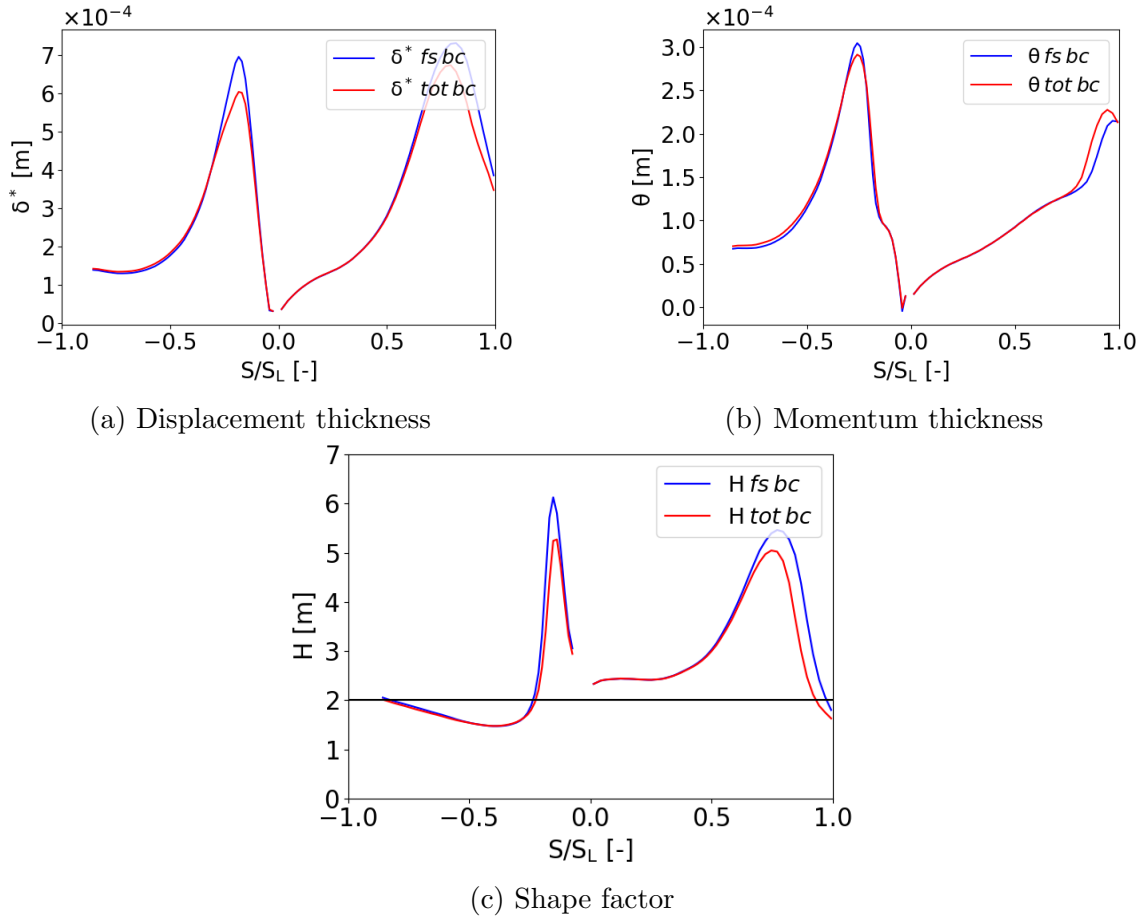


Figure 8.21: Time and spanwise average of displacement thickness (**top-left**), momentum thickness (**top-right**) and shape factor (**bottom**), with total and static inlet boundary conditions (total case taken from [7])

Karman vortex street (Figure 2.7). In plane 05, the average flow angle is higher for negative values of the pitchwise coordinate, and it is lower for positive values. Traveling to plane 06, the trend is the opposite. Nevertheless, the pitchwise average of the flow angle does not change between the two streamwise locations.

The shape of the curves relating to the two numerical simulations is almost identical. However, the case with static inlet conditions shows a shift in the flow angle of about $+0.25^\circ$. Consequently, the resulting deflection ($\delta_{fs} \approx 0.3^\circ$) is smaller compared to the case with total inlet conditions ($\delta_{tot} \approx 0.55^\circ$).

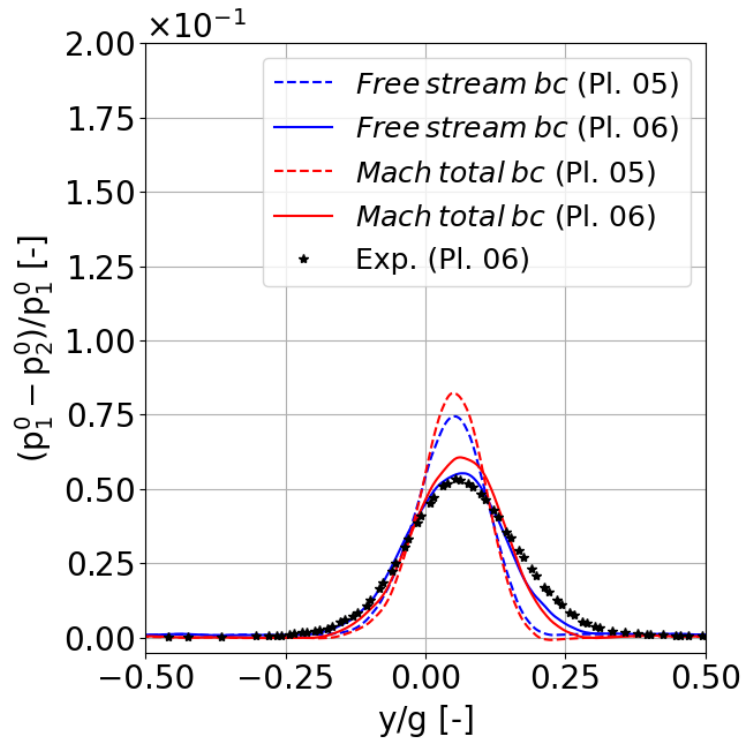


Figure 8.22: Time and spanwise average of the total pressure defect in the wake on planes 05 and 06, with total and static inlet boundary conditions cases (total case taken from [7]) compared to experimental data [1] (plane 06 only)

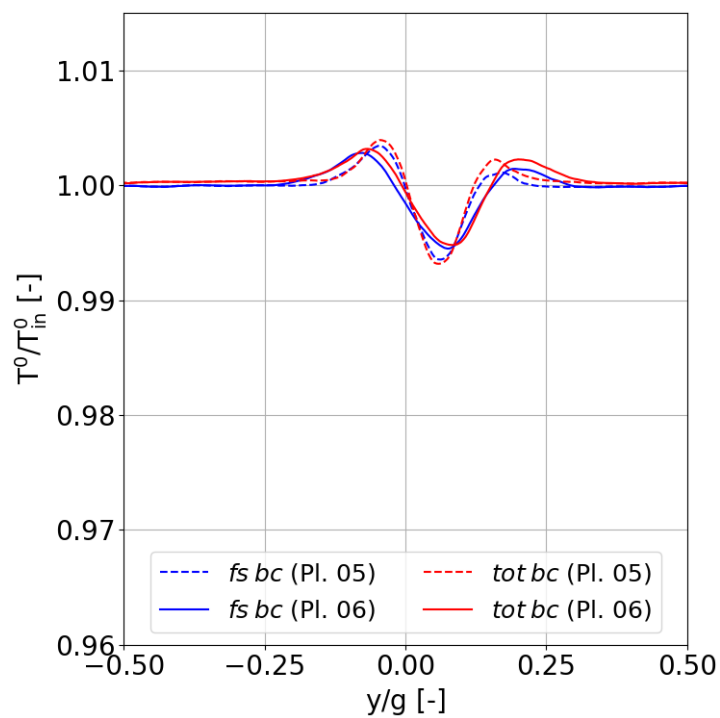


Figure 8.23: Time and spanwise average of the total temperature in the wake on planes 05 and 06, with total and static inlet boundary conditions (total case taken from [7])

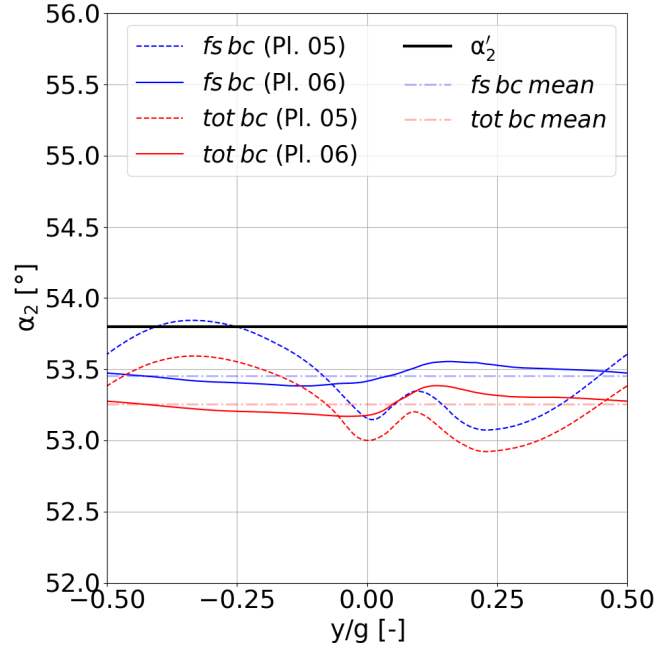


Figure 8.24: Time and spanwise average of the flow angle in the wake on planes 05 and 06, with total and static inlet boundary conditions (total case taken from [7])

Figure 8.25 shows the pitchwise distribution of the Reynolds stresses within the wake. The turbulent content in this region is primarily attributed to the presence of the von Karman vortex street. The intensity of the various Reynolds stress tensor components is strongly influenced by the predominantly two-dimensional nature of this coherent structure. Regarding the diagonal terms, $\overline{u'u'}$ and $\overline{v'v'}$ are of the same order of magnitude and higher than $\overline{w'w'}$. Furthermore, the higher non-diagonal term is $\overline{u'v'}$, while $\overline{u'w'}$ and $\overline{v'w'}$ are both around zero.

Those turbulent features are observable in both planes and for both numerical cases. However, the curves related to plane 06 are flatter due to turbulent decay in the wake. The general behavior for the two numerical cases is the same, with $\overline{v'v'}$ and $\overline{u'v'}$ slightly higher for the static conditions case.

Figure 8.26 shows the energy density spectrum in the wake, with a slope $-5/3$ as a reference of the spectrum function (Equation 2.39). Due to the turbulent decay, the turbulent content in the plane 05 is higher compared to plane 06. However, the energy is distributed in the same way across the different scales. There is no significant spectrum difference between the two numerical simulations in either plane.

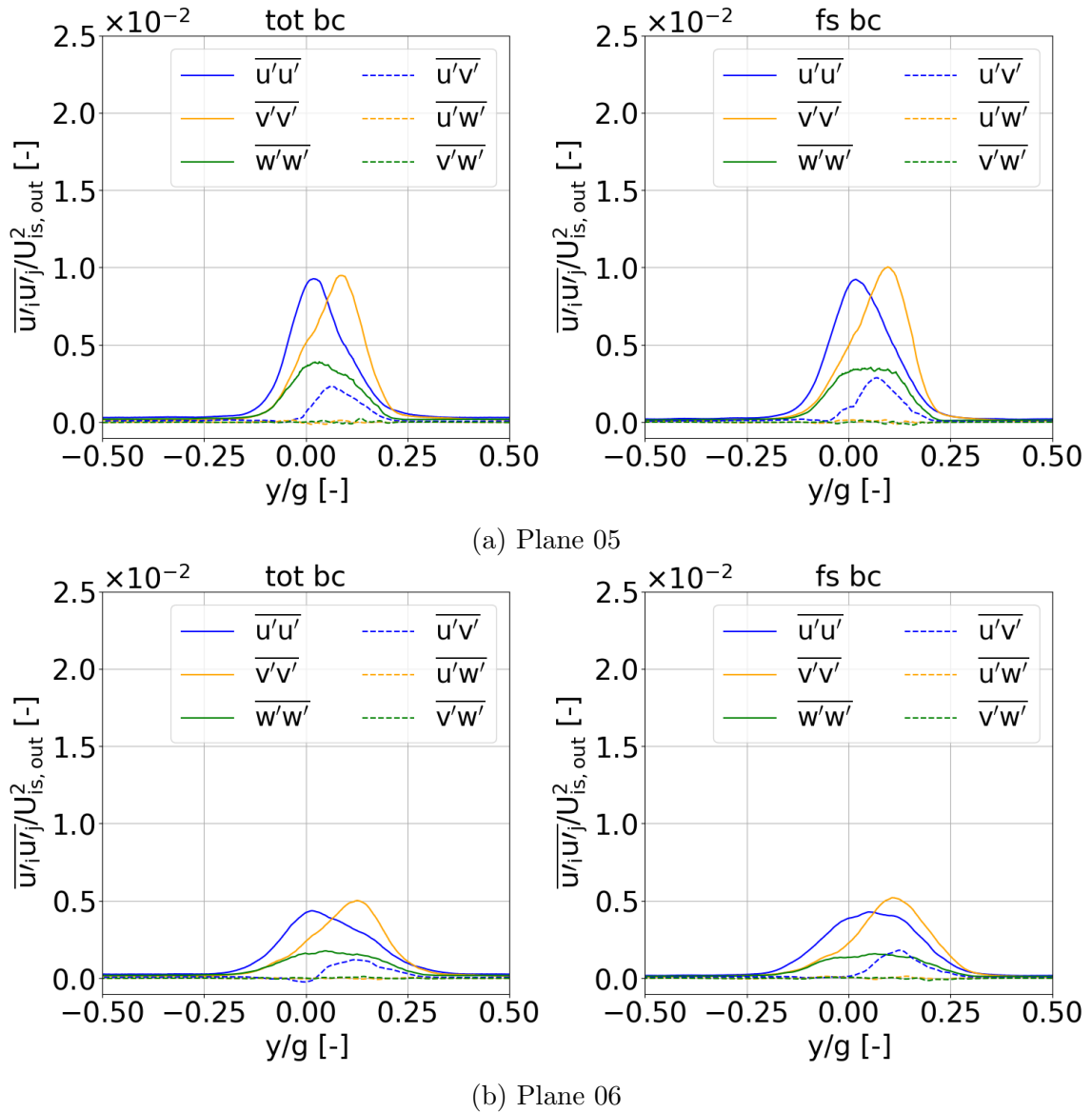


Figure 8.25: Time and spanwise average of the diagonal stresses in the wake on planes 05 and 06, with total and static inlet boundary conditions (total case taken from [7])

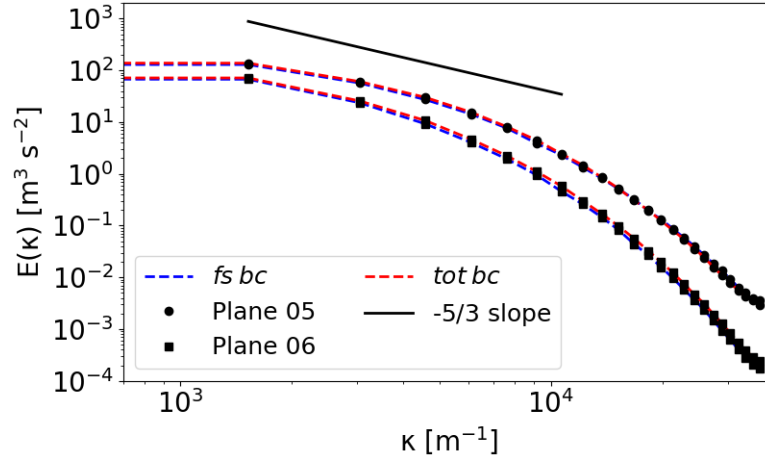
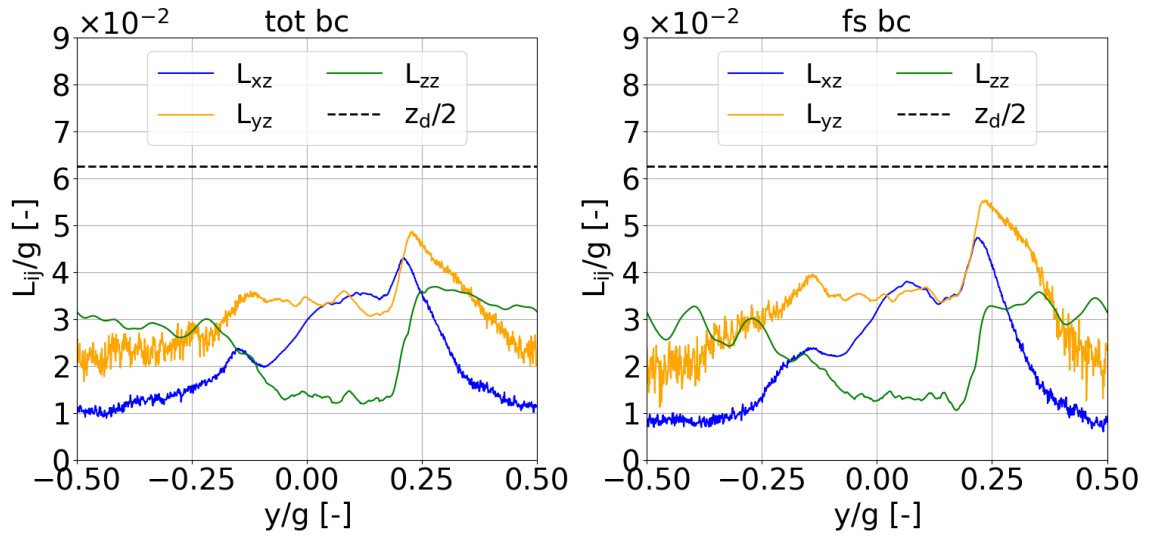


Figure 8.26: Time and spanwise average of the energy density spectrum in the wake on planes 05 and 06, with total and static inlet boundary conditions (total case taken from [7])

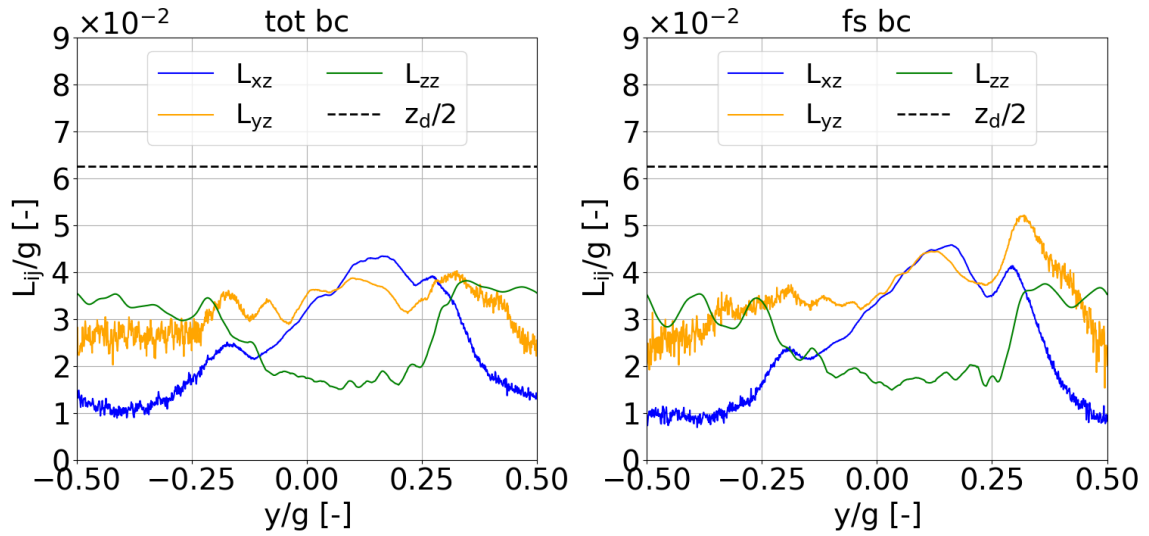
Figure 8.27 shows the spanwise distribution of the integral length scales for the three components of velocity fluctuation, computed along the spanwise direction. The black dotted line indicates half of the spanwise thickness. Since the latter is greater than the length scales, the computational domain should be thick enough to solve the turbulent scales in both numerical simulations.

The general trend of the integral length scales is the same in both planes. Their distribution along the pitchwise direction is strongly affected by the presence of the wake. Since the von Karman vortex street is dominantly two-dimensional, L_{XZ} and L_{YZ} are higher compared to L_{ZZ} in the middle of the plots, where the flow phenomenon occurs. Conversely, L_{XZ} and L_{YZ} are lower than L_{ZZ} at the edges of the plots, far from the wake. The turbulent structure in those regions refers to the injected structures, which have been deformed in different ways in the blade channel. Indeed, L_{XZ} and L_{YZ} exhibit strong fluctuations near the edges. Contrarily, the curves are smoother in the middle due to coherent structures of the vortex street.

The flow characteristics described above are valid for both numerical simulations. However, within the vortex street, L_{XZ} and L_{YZ} are higher for the static conditions case.



(a) Plane 05



(b) Plane 06

Figure 8.27: Time and spanwise average of the integral length scales in the wake on planes 05 and 06, with total and static inlet boundary conditions (total case taken from [7])

Chapter 9

Conclusion

In this master's thesis, the effect of different simulation parameters on DNS with turbulence injection was investigated. The study was performed on two primary domains: a free domain and a high-speed low-pressure turbine.

In the case of the free domain, a parametric study was conducted to evaluate the impact of the following simulation parameters: Reynolds and Mach numbers, inlet boundary conditions type, injection angle, and mesh type. The initial phase of the investigation, conducted by varying the Reynolds and Mach numbers while keeping the other parameters constant, revealed that the effect on turbulence statistics was minimal across different cases.

Subsequently, the remaining three simulation parameters were varied, while maintaining the Reynolds and Mach numbers at their baseline values. The results demonstrated that varying the inlet boundary conditions type leads to a significant variation in turbulence statistics. The turbulence in the case of total inlet conditions is highly anisotropic and also exhibits a substantial discrepancy between L_{YY} and L_{ZZ} compared to L_{XX} . Conversely, the case with static inlet conditions showed isotropic turbulence for the diagonal terms of the Reynolds stress tensor and a greater consistency of L_{XX} with the other integral length scales. Regarding the injection angle, the effect was particularly pronounced in the simulations with total inlet conditions, especially concerning the $\overline{v'v'}$ fluctuations. In contrast, α_{in} had minimal effect on the simulations with static inlet conditions, with the exception of variation for L_{XX} .

The effect of mesh type was evaluated by comparing isotropic and anisotropic meshes, distinguishing between cases with $\alpha_{in} = 0^\circ$ and $\alpha_{in} \neq 0^\circ$. In cases with $\alpha_{in} = 0^\circ$, the mesh type did not induce any significant variation in the turbulence statistics for simulations with total inlet conditions. However, distinct observations were made for simulations with static inlet conditions. In the latter case, the refined anisotropic mesh resulted in a slower decay of turbulence along the streamwise direction. Despite the mesh anisotropy, the turbulence remained isotropic, albeit with higher diagonal terms in the Reynolds stress tensor. Conversely, the integral length scales decreased compared to the isotropic mesh case and exhibited better agreement among themselves. For cases with $\alpha_{in} \neq 0^\circ$, the mesh variation led to changes in the turbulence statistics even for simulations with total inlet conditions. Specifically, the anisotropic mesh, compared to the isotropic one, caused an increase in the diagonal terms of the Reynolds stress tensor proportional to the injection angle, while

the integral length scales decreased. In contrast, the effect of mesh type on simulations with static inlet conditions remained consistent for both $\alpha_{in} \neq 0^\circ$ and $\alpha_{in} = 0^\circ$.

The observations from the free domain simulations were utilized to assess the impact of boundary conditions with turbulence injection in the case of the high-speed low-pressure turbine. To achieve isotropic free stream turbulence, static inlet conditions were employed. The results were then compared with experimental [1] and numerical [7] results pertaining to the same test case. To isolate the effect of inlet boundary conditions, the turbine simulation conducted in this study used the same mesh and computational setup as the simulation used for numerical comparison, with the exception of the inlet conditions. Specifically, static inlet conditions were used in this study, while total inlet conditions were used in [7]. Consistent with the findings from the parametric study, the use of static inlet conditions enabled the attainment of homogeneous and isotropic free stream turbulence. Furthermore, the turbulent kinetic energy was lower compared to the case with total inlet conditions, and exhibited better agreement with the experimental data.

Beyond the inlet region, the primary differences between the two numerical simulations are observable in the separation bubble regions, specifically on the PS near the LE and on the SS near the TE. In both cases, laminar separation occurs, followed by transition and reattachment of the separated flow. However, due to the lower TKE injected in the case with static inlet conditions, the transition and subsequent reattachment occur further downstream. Consequently, the TKE production in the boundary layer due to separation is also shifted downstream, and the flow displacement from the wall due to the separation bubbles is increased. Overall, the simulation with static inlet conditions exhibits better agreement with the experimental data in terms of blade loading and wake characteristics. A final difference between the two numerical simulations pertains to acoustic waves. Specifically, the case with static inlet conditions demonstrates lower acoustic disturbances compared to the case with total inlet conditions.

In conclusion, this study has demonstrated that various types of turbulence injection boundary conditions have a significant impact on DNS results. Future research could explore the influence of additional simulation parameters on turbulence injection, investigate further types of turbulence injection boundary conditions, and examine the effect of these conditions on a wider range of test cases.

Bibliography

- [1] S. Lavagnoli et al. *SPLEEN- High Speed Turbine Cascade– Test Case Database*. Zenodo, June 2023. DOI: 10.5281/zenodo.8075795.
- [2] A. Bolyn. “Detailed Flow Analysis of a Transonic Low Pressure Turbine at Low Turbulence Levels”. Master’s thesis. University of Liège, 2020.
- [3] M. Khateeb. “Impact of Operating Conditions on the Transitional Flow in a Low-pressure Fast Turbine Cascade”. Master’s thesis. University of Liège, 2021.
- [4] M. Borbouse. “Boundary layer stability and shock interactions in a high-speed low pressure turbine cascade”. Master’s thesis. University of Liège, 2023.
- [5] M. Borbouse et al. “Analysis of Separation and Transition on a Novel High-Speed Low Pressure Turbine Cascade”. In: *Proceedings of the Cambridge Unsteady Flow Symposium 2024*. 2024, pp. 341–362. DOI: 10.1007/978-3-031-69035-8_21.
- [6] M. Borbouse et al. *Boundary Layer Stability and Shock Interactions in a High Speed Low Pressure Turbine Cascade*. 2024. URL: <https://orbi.uliege.be/handle/2268/321879>.
- [7] N. Deneffe. “Numerical study of boundary layer stability and compressible flow phenomena in a high-speed low pressure turbine with elevated free-stream turbulence”. Master’s thesis. University of Liège, 2024.
- [8] W. Sutherland. “LII. The viscosity of gases and molecular force”. In: *The London, Edinburgh, and Dublin Philosophical Magazine and Journal of Science*. 5th ser. 36.223 (1893), pp. 507–531. DOI: 10.1080/14786449308620508.
- [9] S. B. Pope. *Turbulent Flows*. Cambridge University Press, 2000.
- [10] P. A. Davidson. *Turbulence: An Introduction for Scientists and Engineers*. Oxford University Press, 2004.
- [11] L. F. Richardson. *Weather prediction by numerical process*. Cambridge University Press, 1922.
- [12] A. N. Kolmogorov. “The Local Structure of Turbulence in Incompressible Viscous Fluid for Very Large Reynolds Numbers”. In: *Proceedings of the Royal Society of London* 434 (1991), pp. 9–13.
- [13] M. Quadrio. *Turbulence: Physics and Modeling*. Lecture notes. 2023-2024.
- [14] G. I. Taylor. “The spectrum of turbulence”. In: *Proceedings of the Royal Society of London* 164 (1938), pp. 476–490.
- [15] P. A. Durbin and B. A. P. Reif. *Statistical Theory and Modeling for Turbulent Flows*. 2nd. John Wiley & Sons Ltd, 2011.

-
- [16] L. Prandtl. “On the boundary layers in fluids”. In: *Verhandlungen des dritten internationalen Mathematiker-Kongresses in Heidelberg 1904*. Ed. by A. Krazer. English translation in: *Early Developments of Modern Aerodynamics*, edited by J. A. K. Ackroyd, B. P. Axcell, and A. I. Ruban, Butterworth-Heinemann, Oxford, UK, 2001, p. 77. Leipzig, Germany: Teubner, 1905, p. 484.
- [17] H. Schlichting and K. Gersten. *Boundary-Layer Theory*. 9th. Springer, 2017.
- [18] P. K. Kundu and I. M. Cohen. *Fluid Mechanics*. 2nd. Academic Press, 2001.
- [19] M. Zdravkovich. *Flow around circular cylinders. Volume 1: Fundamentals*. Oxford University Press, 1997.
- [20] J. D. Denton. “The 1993 IGTI Scholar Lecture: Loss Mechanisms in Turbomachines”. In: *Journal of Turbomachinery* 115.4 (1993), pp. 621–656.
- [21] R. E. Mayle. “The 1991 IGTI Scholar Lecture: The Role of Laminar-Turbulent Transition in Gas Turbine Engines”. In: *Journal of Turbomachinery* 113.4 (1991), pp. 509–536.
- [22] B. Thwaites. “Approximate Calculation of the Laminar Boundary Layer”. In: *The Aeronautical Quarterly* 1.3 (1949), pp. 245–280.
- [23] A. Hatman and T. Wang. “A Prediction Model for Separated-Flow Transition”. In: *Journal of Turbomachinery* 121.3 (1999), pp. 594–602.
- [24] W. Lou and J. Hourmouziadis. “Separation Bubbles Under Steady and Periodic-Unsteady Main Flow Conditions”. In: *Journal of Turbomachinery* 122.4 (2000), pp. 634–643.
- [25] *SPLEEN project*. URL: <https://www.h2020-spleen.eu/>.
- [26] *VKI - Research*. URL: <https://www.vki.ac.be/index.php/research-consulting-mainmenu-107>.
- [27] L. Simonassi et al. “An experimental test case for transonic low-pressure turbines- part 1 : Rig Design, instrumentation and experimental methodology”. In: *Volume 10B : Turbomachinery- Axial Flow Turbine Aerodynamics ; Deposition, Erosion, Fouling, and Icing ; Radial Turbomachinery Aerodynamics*. 2022.
- [28] L. Simonassi et al. “An experimental test case for transonic low-pressure turbines- part 2 : Cascade aerodynamics at on- and off-design Reynolds and Mach numbers”. In: *Volume 10B : Turbomachinery- Axial Flow Turbine Aerodynamics ; Deposition, Erosion, Fouling, and Icing ; Radial Turbomachinery Aerodynamics*. 2022.
- [29] P. E. Roach. “The generation of nearly isotropic turbulence by means of grids”. In: *International Journal of Heat and Fluid Flow* 8.2 (1987), pp. 82–92.
- [30] F. N. Frenkiel. “The Decay of Isotropic Turbulence”. In: *Journal of Applied Mechanics* 15.4 (1948), pp. 311–321.
- [31] C. Hirsch. *Numerical Computation of Internal and External Flows. Volume 1: Fundamentals of Computational Fluid Dynamics*. 2nd. Butterworth-Heinemann, 2007.
- [32] *Cenaero*. URL: <https://www.cenaero.be/>.
- [33] *CECI*. URL: <https://www.ceci-hpc.be/>.

- [34] *Documentation Lucia*. URL: <https://doc.lucia.cenaero.be/>.
- [35] V. Dolejší and M. Feistauer. *Discontinuous Galerkin Method: Analysis and Applications to Compressible Flow*. Vol. 48. Springer Series in Computational Mathematics. Springer, 2015.
- [36] K. Hillewaert. “Development of the discontinuous Galerkin method for high resolution, large scale CFD and acoustics in industrial geometries”. Ph.D. dissertation. Université catholique de Louvain, 2013.
- [37] Carton De Wiart and Corentin. “Towards a Discontinuous Galerkin Solver for Scale-resolving Simulations of Moderate Reynolds Number Flows, and Application to Industrial Cases”. Ph.D. dissertation. Université catholique de Louvain, 2014.
- [38] M. Hao, J. Hope-Collins, and L. di Mare. “Generation of turbulent inflow data from realistic approximations of the covariance tensor”. In: *Physics of Fluids* 34.11 (2022), p. 115140. DOI: 10.1063/5.0106664.
- [39] X. Wu. “Inflow Turbulence Generation Methods”. In: *Annual Review of Fluid Mechanics* 49 (2017), pp. 23–49.
- [40] X. Wu, K. D. Squires, and T. S. Lund. “Large eddy simulation of a spatially developing turbulent boundary layer”. In: *Supercomputing '95: Proceedings of the 1995 ACM/IEEE Conference on Supercomputing*. San Diego, CA, USA, 1995. DOI: 10.1145/224170.224408.
- [41] T. Lund, X. Wu, and K. Squires. “Generation of inflow data for spatially-developing boundary layer simulations”. In: *Journal of Computational Physics* 140 (1998), pp. 233–258. DOI: 10.1006/jcph.1998.5882.
- [42] S. Xu and M. Martin. “Assessment of inflow boundary conditions for compressible turbulent boundary layers”. In: *Physics of Fluids* 16 (2004), pp. 2623–2639. DOI: 10.1063/1.1758218.
- [43] N. S. Dhamankar, G. A. Blaisdell, and A. S. Lyrintzis. “Overview of Turbulent Inflow Boundary Conditions for Large-Eddy Simulations”. In: *AIAA Journal* 56 (2017). DOI: 10.2514/1.J055528.
- [44] A. Keating et al. “A priori and a posteriori tests of inflow conditions for large-eddy simulation”. In: *Journal of Fluids* 16 (2004). DOI: 10.1063/1.1811672.
- [45] A. Keating and U. Piomelli. “A dynamic stochastic forcing method as a wall-layer model for large-eddy simulation”. In: *Journal of Turbulence* 7 (2006). DOI: 10.1080/14685240612331392460.
- [46] M. Klein, A. Sadiki, and J. Janicka. “A digital filter based generation of inflow data for spatially developing direct numerical or large eddy simulations”. In: *Journal of computational Physics* 186.2 (2003), pp. 652–665.
- [47] K. Fukami et al. “Synthetic turbulent inflow generator using machine learning”. In: *Physical Review Fluids* 4.6 (2019), p. 064603. DOI: 10.1103/PhysRevFluids.4.064603.
- [48] J. Kim and C. Lee. “Deep unsupervised learning of turbulence for inflow generation at various reynolds numbers”. In: *Journal of Computational Physics* 406 (2020), p. 109216. DOI: 10.1016/j.jcp.2019.109216.

- [49] M. Rasquin et al. “Direct numerical simulations of airfoil cascades for the improvement of turbulence models through database generation”. In: *Proceedings of 15th European Conference on Turbomachinery Fluid dynamics & Thermodynamics, ETC15*. Budapest, Hungary, Apr. 2023.
- [50] R. S. Rogallo. *Numerical Experiments in Homogeneous Turbulence*. NASA Technical Memorandum. 1981.
- [51] T. Passot and A. Pouquet. “Numerical simulation of compressible homogeneous flows in the turbulent regime”. In: *Journal of Fluid Mechanics* 181 (1987), pp. 441–466.
- [52] Z. Xiong, S. Nagarajan, and S. K. Lele. “Simple method for generating inflow turbulence”. In: *AIAA Journal* 42 (2004). DOI: 10.1016/j.jcp.2008.10.027.
- [53] J. Larsson. “Blending technique for compressible inflow turbulence: Algorithm localization and accuracy assessment”. In: *Journal of Computational Physics* 228 (2009). DOI: 10.1016/j.jcp.2008.10.027.